Università degli Studi di Pisa

Facoltà di Scienze Matematiche, Fisiche e Naturali

Corso di Dottorato in Matematica

Tesi di Dottorato

On theoretical and experimental aspects of the rotation of celestial bodies

Candidato
Stefano Cicalò

Relatore
Prof. Andrea Milani Comparetti
Università di Pisa

Anno 2012

Contents

I Determination of the rotation of Mercury from satellite gravimetry 1

1 The rotation of the planet Mercury and the state of its core 4
1.1 Secular theory: Laplace plane and Cassini state 4
1.1.1 Reference systems 5
1.1.2 The Peale's experiment 5
1.2 Short-term perturbation theory: the librations in longitude 7
1.2.1 Librations effects without planetary perturbations 7
1.2.2 Librations effects with planetary perturbations 8
1.2.3 Choice of the initial conditions: an hybrid rotation model 12

2 Determination of the rotation state of Mercury from satellite gravimetry 13
2.1 Possible methods for the determination of the rotation of Mercury and the state of its core. 13
2.1.1 Radar observations of the surface from the Earth 14
2.1.2 Pure remote gravimetry 14
2.1.3 High resolution camera imaging and remote gravimetry 15
2.1.4 Least squares 17
2.2 Gravity field and rotation state: symmetries and undetermined coefficients 18
2.3 Analytical study: the model problem 18
2.3.1 Rotation of the gravity field 19
2.3.2 Simplifying assumptions 19
2.3.3 Hill's equations 20
2.3.4 Rotation from gravimetry analytical results 21
2.4 Rank deficiency in the orbit determination around another planet 24
2.5 Realistic Mercurycentric dynamics 25
2.5.1 Rotational dynamics: semi-empirical model 25
2.5.2 Sun, planetary and tidal perturbations 27
2.5.3 Non gravitational perturbations and accelerometer 28
2.5.4 Maneuvers 31
2.5.5 Relativistic corrections 33
2.6 Numerical simulation 33

2.6.1 Architecture of the *Orbit_14* software system 33
2.6.2 Error models 36
2.6.3 Pure and Correlated-Constrained Multi-arc method 38
2.7 Results and statistical analysis 46
2.7.1 Assumptions 46
2.7.2 Results 49
2.8 Conclusions 60

A The observation model **62**
A.1 The light time iterations 62
A.2 The time corrections 63
A.3 Integrated observables 63

B Global dynamics and relativistic models **65**
B.1 Solar System Barycentric orbits of Mercury and the Earth-Moon barycenter 65
B.2 Rotational dynamics of the Earth 71

II Rotational dynamics of asteroids under non-gravitational perturbations **76**

3 Averaged rotational dynamics of an asteroid in tumbling rotation under the YORP torque **77**
3.1 Introduction 77
3.2 Rotational dynamics 79
3.2.1 Reference systems 79
3.2.2 Angular variables 79
3.2.3 The rotation dynamical system 80
3.2.4 The YORP torque 81
3.2.5 Dissipation of Energy 84
3.3 Analytical formulas for the secular solution 84
3.3.1 Quantities averaged over the orbital motion 87
3.3.2 Factors averaged over the rotational motion 88
3.3.3 Averaged equations 89
3.3.4 The obliquity 89
3.3.5 Separation of variables and limitations 91
3.3.6 Averaged equations with dissipation of energy 91
3.3.7 Comparison between full and averaged solution 94
3.4 Dynamics without dissipation 96
3.4.1 Equilibrium points for the obliquity 96
3.4.2 Equilibrium points for the dynamic inertia $\bar{I}_D$ 97
3.4.3 Equilibrium points for the angular momentum magnitude 100
3.4.4 Generic examples of dynamics in the plane $(\bar{I}_D, \bar{\delta})$ 101
3.4.5 Generalizations 103

3.5 Transition and chaotic behavior 105
3.5.1 The transition probability 107
3.5.2 Chaotic phase and steady state evolution 108
3.5.3 Tests on the chaotic transition 109
3.5.4 Other possible transitions 112
3.6 Tests on asteroids 113
3.6.1 Computation of the $\mathcal{D}_k$ functions 113
3.6.2 Tests of the dynamics in detail: Asteroid Toutatis 120
3.7 Conclusions 122

C The averaged factors **123**

Part I

Determination of the rotation of Mercury from satellite gravimetry

Introduction.

According to science historians, Isaac Newton refused to publish his solution of the 2-body problem until when he had the proof that a spherically symmetric body generates, outside the body, the same gravity field as a point mass placed in the center of mass. Unfortunately, this also proves that the *inverse gravimetry problem* is ill-posed: even a perfect knowledge of the gravity field outside a body does not allow to solve for the internal mass distribution.

A question often arising in discussions on the science goals of planetary exploration missions is the following. Can a planetary mission *constrain the internal structure* without landing on the planet? Newton's classical result, and its modern versions, show that even a perfect knowledge of the gravity field outside the surface of the planet does not constrain the concentration of the mass towards the center, thus does not allow to constrain the size and density of the core. E.g., the 6 coefficients of the moment of inertia tensor are linearly related to the 5 harmonic coefficients of degree 2: if the latter are measured with remote gravimetry, one unconstrained parameter remains.

A solution of the problem could be to directly observe the rotation state of the planet. From a suitably defined obliquity of the rotation axis it is possible to estimate the absolute value of the principal moment of inertia, thus scaling correctly the moment of inertia tensor. It is also possible to measure the libration in longitude resulting from the coupling of the permanent equatorial ellipticity of Mercury with the Sun's tidal pull, and from this to detect the presence of a decoupling (liquid layer) between core and mantle, see [Peale 1988].

A first full analysis on this topic is [Wu et al. 1995], where the possibility of measuring Mercury rotation by a lander-orbiter system is investigated. Under the hypothesis of very accurate range/range-rate tracking data from the Earth and good ranging of the lander from the orbiter, the results presented are very good, with total uncertainties for the libration in longitude amplitude and the obliquity of 0.26 and 0.03 arcsec, respectively. For technical, and thus economical, reasons, for instance the environment at Mercury surface makes very difficult to design a lander capable of resisting for long enough to succeed in the experiment, this experiment has never been performed in reality, but it has been a strong source of inspiration for the ESA BepiColombo mission to Mercury.

In fact, other techniques for measuring the rotation state of a planet have been proposed later: e.g., by using a high resolution camera (as it will be attempted by the ESA BepiColombo mission to Mercury), or by using the radar images of the surface (as done by the Cassini mission with Titan [Stiles et al. 2008], or by [Margot et al. 2007] for the rotation of Mercury).

This *rotation experiment* proposed for BepiColombo imposes very tough constraints on the thermo-mechanical design of the orbiter, because of the need to measure spacecraft to surface directions in an absolute reference frame. Thus it would have been desirable to measure the rotation from the gravity field above the surface. In principle, the time-dependent gravity field generated by a rotating planet, measured in an inertial frame, depends upon the rotation state. Thus, by tracking for long enough and accu-

rately enough a satellite, it could be possible to measure the planet rotation without looking at the planet.

A theoretical difficulty in determining the rotation state by using only measurements of the gravity field is due to the presence of an approximate symmetry in the orbit determination problem. The approximate symmetry results from symmetry breaking of an exact symmetry, which is the one applicable to a spherically symmetric planet: if it rotates, the gravity field does not change, thus the orbit of a satellite does not change and the tracking data do not contain any signal due to rotation.

This allows us to understand that the quality of measuring the rotation state of Mercury from gravimetry is proportional to the magnitude of the harmonic coefficients of the planet gravity field.

One of the main instruments of the ESA BepiColombo mission to Mercury is the so called Mercury Orbiter Radio Science Experiment, (*MORE*, see [Benkhoff et al. 2010]), which has to address scientific goals in geodesy, geophysics and fundamental physics. It consists in the determination of a large number of parameters characterizing the entire dynamics of the spacecraft tracked from the Earth, e.g. the spherical harmonics of the gravity field of Mercury C_{lm}, S_{lm}, some general relativity PPN parameters, the initial conditions of Mercury's center of mass, the initial conditions of the spacecraft and several other quantities such as the Mercury rotation parameters (obliquity and libration in longitude), in a global least squares fit of the observable tracking data and on-board camera images (see e.g. [Milani et al. 2001] and [Milani et al. 2002]).

In this work we analyze the problem of the determination of the rotation of Mercury, and the principal aspects related to the state of its core, in the framework of a global parameter estimation process. The parameters describing the rotation of Mercury are determined by a global least squares fit of the tracking data alone (*the gravimetry experiment*), this gives a contribution to the separate experiment that includes the data from the high resolution camera (*the rotation experiment*). The simulation and the data analysis is performed with realistic measurement accuracy.

The work is organized as follows: in Chapter 1 we give a general description of the Mercury rotation theory. In Chapter 2 we describe the technique proposed for the determination of the rotation of Mercury and the state of its core, and we study this problem both with an analytic simplified model and with a realistic numerical simulation giving concrete and quantitative results about the feasibility of the *gravimetry experiment*. In the Appendices A and B, the main difficulties in modeling the global dynamics affecting the observables are reported and discussed, in particular the relativistic models used in the Solar System motion of Mercury and the Earth, and the observation model.

Chapter 1

The rotation of the planet Mercury and the state of its core

Outline. In Section 1.1 a general description of the secular solution for the rotation of Mercury is given, with its spin-orbit resonance and Cassini state. The short-term solution for the rotation of Mercury, along with planetary perturbation effects on the librations in longitude is presented in Section 1.2. In these two Sections the basic explicit relations between the rotation and the parameters describing the state of the core are also given.

1.1 Secular theory: Laplace plane and Cassini state

The planet Mercury follows a highly eccentric orbit around the Sun ($e \cong 0.206$) and it shows a particular spin-orbit resonance of $3:2$ (Fig.1.1). This resonance is explained by the theory of G. Colombo [Colombo and Shapiro 1966], which considers Mercury as a rigid body and combines the ellipticity of the orbit and of Mercury's equator with the Sun gravitational torque acting on it, in a secular perturbation approach. The exact resonance is a minimum energy condition of the system, and the longest axis of the elliptic equator has to be aligned with the Sun when Mercury is at perihelion.

A secular theory of the rotation of a rigid Mercury should take also into account the *Cassini laws*, by which the (averaged) spin axis has to belong to the *Cassini plane*, which is the one spanned by the orbital plane normal and the axis around which the orbital plane precesses because of secular planetary perturbations, averaged over long time scales. Generalizing the Cassini's laws for the Moon, Colombo [Colombo and Shapiro 1966], and later Peale [Peale 1969], proposed a rotation model for Mercury according to which the planet actually occupies a Cassini state of type 1, meaning that the orbit normal lies between the spin axis and the precessional axis. This "precessional axis" is also commonly called the *Laplace pole* $\mathbf{Z}_L$, and it can be determined by averaging the perturbations over a suitable time span (e.g. see [Yseeboodt and Margot 2006], [Peale 2006], [D'Hoedt et al. 2009]). The precession period obtained from the theory is

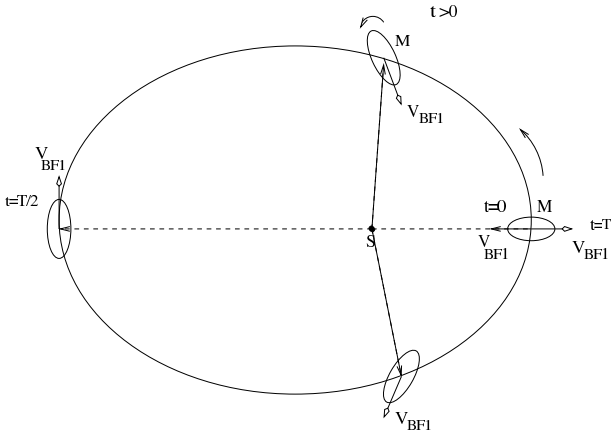

Figure 1.1: The 3 : 2 spin-orbit resonance of Mercury. The figure shows the elliptic equator of Mercury, whose longest axis is aligned towards the Sun only twice per orbit, resulting in a tidal torque with period half the orbital period of the planet.

$\sim 250\,000$ years, and the angle η between the orbit normal $\mathbf{Z}_1$ and the spin axis $\mathbf{V}_s$ is called the *obliquity*. The estimated position of $\mathbf{Z}_L$ in the in the Ecliptic J2000 reference frame (latitude and longitude) is:

$$\beta_L = 87.2883^\circ, \quad \lambda_L = 41.8068^\circ.$$

We will assume the spin axis coincident with the maximum moment of inertia axis of Mercury $\mathbf{Z}_3$ (no wobbling), and we indicate the Cassini state equilibrium position for the spin axis with $\mathbf{V}_s \equiv \mathbf{V}_c$ (Fig.1.2).

1.1.1 Reference systems

We now introduce the fundamental reference systems that will be used in the following.

Let us assume as inertial reference system for the description of Mercury rotation the Ecliptic J2000, denoted by $(\mathbf{X}_0, \mathbf{Y}_0, \mathbf{Z}_0)$. We also associate an inertial reference frame to the orbit of Mercury at J2000: $(\mathbf{X}_1, \mathbf{Y}_1, \mathbf{Z}_1)$ is the reference frame where $\mathbf{Z}_1$ is the orbital plane normal and $\mathbf{X}_1 = -\mathbf{X}_{peri}$, being $\mathbf{X}_{peri}$ the pericenter direction at J2000. For our purposes, this can be considered a quasi-inertial frame.

Let $(\mathbf{X}_3, \mathbf{Y}_3, \mathbf{Z}_3)$ be the Mercury body-fixed principal of inertia reference frame. $\mathbf{X}_3$ is the unit vector along the longest axis of the equator of Mercury (minimum moment of inertia), assumed as rotational reference meridian.

1.1.2 The Peale's experiment

With some approximations, in particular by assuming Mercury in a permanent Cassini state with constant obliquity, [Peale 1988] proposes that, with the global gravity field and the rotation state, it is possible to constrain the internal structure of the planet,

determining if there is decoupling between a solid surface (mantle) and an inner core (presumably due to a liquid layer). Let's call $A < B < C$ the principal moments of inertia of Mercury as a rigid body (rotating around the axis of maximum moment of inertia). From this secular theory, the obliquity of Mercury η_c, occupying the Cassini state 1 equilibrium position $\mathbf{V}_c$, is given by the following approximated formula ([Peale 1988], [Peale 2006], Fig.1.2):

$$\frac{1}{\eta_c} = \frac{1}{\sin i_L} \left(\frac{n\, J_2\, f(e)}{w_L} \frac{MR^2}{C} - \cos i_L \right) , \tag{1.1}$$

where M is the mass of Mercury, R is its mean radius, $f(e) = G_{210}(e) + 2C_{22}G_{201}(e)/J_2$, $J_2 = -C_{20}$ and C_{22} are the degree 2 potential coefficients of Mercury gravity field (in the principal of inertia body-fixed reference system), G_{210}, G_{201} are eccentricity functions (defined in [Kaula 1966]), n is the orbital mean motion, i_L is the inclination of the orbit with respect to the Laplace pole $\mathbf{Z}_L$ and w_L is the nearly constant rate of the precession of the orbit of Mercury around $\mathbf{Z}_L$ ($2\pi/w_L \sim 250\,000$ years). Thus the obliquity is directly related to the quantity C/MR^2, called the *concentration coefficient*.

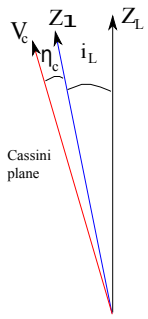

Figure 1.2: Vectors and angles involved in the Cassini state. η_c is the *proper*, nominal, obliquity.

Let's now suppose that there is a core decoupled from a rigid mantle, and that the core does not follow the mantle over short time scales (while it does over long time scales, [Peale 1988]). This means that the moments of inertia reacting to the torques over short time scales are the ones of the mantle alone $A_m < B_m < C_m$. In particular, assuming rotation around principal axis of inertia, the moment appearing in the rotational kinetic energy is only C_m, i.e. the one with respect to the spin axis. Then, if Mercury has a core decoupled from the rigid mantle, the ratio C_m/C is not equal to 1, and it is expected to be ~ 0.5 for a planet with an important liquid layer. Also the concentration coefficient C/MR^2 is 0.4 for an homogeneous planet while it is expected to be significantly less for Mercury. Peale proposed to determine this ratio by the following relation:

$$\frac{C_m}{C} = \frac{C_m}{B-A} \frac{M\,R^2}{C} \frac{B-A}{M\,R^2} , \tag{1.2}$$

where the first factor can be determined by measuring the short term effects on the rotation of Mercury (librations in longitude, see next Section 1.2), the second factor is measured by the obliquity $\eta \cong \eta_c$, and the third by the harmonic coefficient C_{22}:

$$\frac{B-A}{M\,R^2} = 4\,C_{22}. \tag{1.3}$$

Thus it should be possible, by measuring the rotation state of Mercury along with its gravity field, to constrain both the physical state and the state of Mercury's core. An error budget for the study of the interior structure of Mercury would consist in measuring C_m/C with a relative accuracy around 10 % and C/MR^2 with a relative accuracy around 1 % [Milani et al. 2001].

Possible secular deviations of the spin axis $\mathbf{Z}_3$ from the Cassini state equilibrium position $\mathbf{V}_c$ can be modeled by suitable corrective constants.

1.2 Short-term perturbation theory: the librations in longitude

We have seen that, according to [Peale 1988], an interior model of Mercury consisting in a multi-layer, rigid mantle decoupled from the core, implies that the short-term rotation of the planet refers to the rotation of the mantle alone. Thus, assuming no wobbling, the moment of inertia appearing in the kinetic energy is C_m. A first general analysis of the short-term effects has been done considering only the torque of the Sun on the elliptic equator of Mercury. More recently, the indirect effects of planetary perturbations on the rotation of Mercury have been considered (e.g. see [Peale et al. 2007],[Peale et al. 2009],[Dufey et al. 2008], [Dufey et al. 2009] and [Yseeboodt et al. 2010]).

1.2.1 Librations effects without planetary perturbations

The gravitational torque from the Sun causes the phenomenon of libration in longitude, which is an oscillation around the secular equilibrium condition of the 3 : 2 spin-orbit resonance. Let's consider as a first approximation that the obliquity of Mercury is zero, with Mercury rotating around an axis parallel to the orbital angular momentum, and in a 2-body approximation. Let ϕ be the Mercury rotation angle, measured from the direction of pericenter to the zero meridian on the planet surface given by the axis of minimum moment of inertia (Mercury's equatorial long axis). Then, introducing the libration angle $\gamma = \phi - 3/2\,\ell$ (ℓ being the mean anomaly), it is possible to solve analytically for the small oscillations of γ around the equilibrium position $\gamma = 0$ (Fig. 1.3). For a more detailed discussion and for the following results see e.g. [Balogh et al. 2002] or [Jehn et al. 2004].

Assuming that the free oscillations (which have a period of $\sim$ 12 years) have been damped by dissipation effects, it turns out that the main oscillation term has the orbital

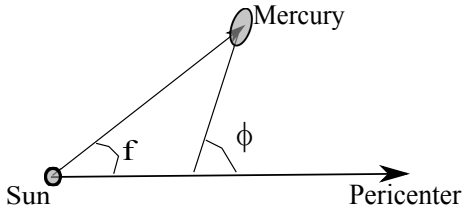

Figure 1.3: Geometry of the rotation of Mercury: f is the true anomaly, ϕ is the rotation angle measured from the direction of pericenter. $\phi - 3/2\ell$ is the libration angle, being ℓ the mean anomaly of Mercury.

period of Mercury (~ 88 days). A good approximation of ϕ is of the form:

$$\phi = \frac{3}{2}M + \epsilon \sin M + \frac{\epsilon}{\mu} \sin 2M \ , \tag{1.4}$$

where $\mu \cong -9.483$ is a numerical constant depending only on the eccentricity of Mercury e and ϵ is the *libration in longitude amplitude*.

It is also possible to find an approximated formula for ϵ. A spherical liquid core implies $B_m - A_m = B - A$, and an approximated formula for the libration amplitude ϵ is

$$\epsilon = \frac{3}{2}\frac{B-A}{C_m}(1 - 11e^2 + \frac{959}{48}e^4 + ...) \ , \tag{1.5}$$

An reference value for ϵ is $\sim 35\,\mathrm{arcsec}$ ($(B-A)/C_m = 2 \times 10^{-4}$).

1.2.2 Librations effects with planetary perturbations

A more complete rotation theory, including also planetary perturbations, has been developed by many authors. Among them, we recall again [Dufey et al. 2009] and [Yseeboodt et al. 2010].

As we already pointed out, the difficulty of finding a reliable model for the rotation of Mercury lies in the fact that over long time scales Mercury should behave as a rigid body, instead over short time scales it should behave as a multi-layer body. One of the main properties of these two models are the proper free libration period and free precession period, being respectively ~ 15.85 and ~ 1065 years for the rigid case ([D'Hoedt & Lemaitre 2004]), and ~ 12.06 and ~ 616 years for the multi-layer model ([Dufey et al. 2009]), with a value for the ratio of the polar moments of inertia $C_m/C = 0.579$ ([Margot et al. 2007]). As regards the librations in longitude, being the multi-layer model the one commonly used, the ~ 12.06 years free libration term represents a critical value for the amplitudes of planetary perturbation effects with periods close to it. In particular, the ~ 11.8 years Jupiter period is evidently close to a resonance and the effect of its perturbation on Mercury's libration could be large. This near

resonance, ruled by the value of C_m, plays a key role in all the studies about planetary perturbations on the rotation of Mercury.

In [Yseeboodt et al. 2010], a completely analytical study on the forced planetary perturbations on the librations in longitude is performed, obtaining explicit formulas for the libration amplitudes and phases in an analogous way to the case without planetary perturbations (formula (1.4)). An analytical formula for the rotation angle of Mercury, from an inertial direction to the axis of minimum moment of inertia, is given in the form ([Yseeboodt et al. 2010], Sec. 7):

$$\phi = \alpha t + \sum_{i=1}^{\infty} \phi_i \cos\left(w_i t + \varphi_i\right) + \phi_0 \,. \tag{1.6}$$

where α is the secular rate of the rotation angle, ϕ_i, w_i and φ_i are the amplitudes, periods and phases of the periodic part and ϕ_0 is a constant. This formula is valid over a few tens of years around J2000. All the quantities appearing in (1.6) are computed assuming as reference epoch J2000, and as inertial reference direction the intersection between the Ecliptic and the orbital plane of Mercury at J2000. In this way an approximated value for α is $\alpha = 3/2\, n + \dot{\varpi}_t$, where n is the mean motion of Mercury at J2000 and ϖ_t is the mean angular velocity of the longitude of pericenter. The periodic part includes the main terms with periods multiples of the orbital period of Mercury and the terms due to planetary perturbations, while the free libration is assumed to be damped. Moreover, all the amplitudes and phases can be expressed as functions of $(B - A)/C_m$ (like in formula (1.5)) and a dissipation parameter.

Among the various trigonometric terms in the series, only few of them are significant (above the ~ 1 arcsec level): at most four waves of basic period $2\pi/n$ (whose first and second amplitudes are the same as in Sec. 1.2.1 and the phases are zero with respect to the solar anomaly as in formula (1.4)), and five terms with the basic periods depending on Venus, Jupiter, Earth and Saturn ([Yseeboodt et al. 2010], Tab. 2), see Tab. 1.1. Besides the main ~ 88 days libration term, the largest perturbation is due to Jupiter and it is explained by the proximity to the resonance with the ~ 12.06 years free libration period.

	Period $2\pi/w_i$ (years)	ϕ_i (arcsec)	φ_i (deg)	$\phi_i w_i$ (arcsec/year)
Jupiter	11.86	40.25	-8.43	21.18
Jupiter	5.93	1.37	-175.85	1.46
Venus	5.66	3.59	-92.84	4.02
Earth	6.57	0.58	152.14	0.73
Saturn	14.72	1.6	34.90	0.73

Table 1.1: Values for the largest forced libration effects on the libration in longitude of Mercury at J2000, for a nominal value of $(B - A)/C_m = 2.03 \times 10^{-4}$ (from [Yseeboodt et al. 2010]).

In [Dufey et al. 2009] a comparative analytical and numerical analysis of the rotation of Mercury is performed. The dynamics is described in an Hamiltonian formalism, applying the Lie averaging process in the analytical study. Here in the following we briefly recall the main points of the numerical approach used in the paper.

First, let ω_0, Ω_0, i_0 be the argument of pericenter, the longitude of the ascending node and the inclination of the orbit of Mercury with respect to the Ecliptic J2000 system respectively ($\varpi_0 = \Omega_0 + \omega_0$ is measured from $\mathbf{X}_0$ to $\mathbf{X}_{peri}$). Moreover, let h, g, K be the longitude of the ascending node of the equatorial plane of Mercury in the Ecliptic plane (the longitude of the rotational node), the rotation angle from the rotational node to the meridian $\mathbf{X}_3$, and the obliquity K between the ecliptic pole $\mathbf{Z}_0$ and the spin pole $\mathbf{Z}_3$ respectively (Fig.1.4).

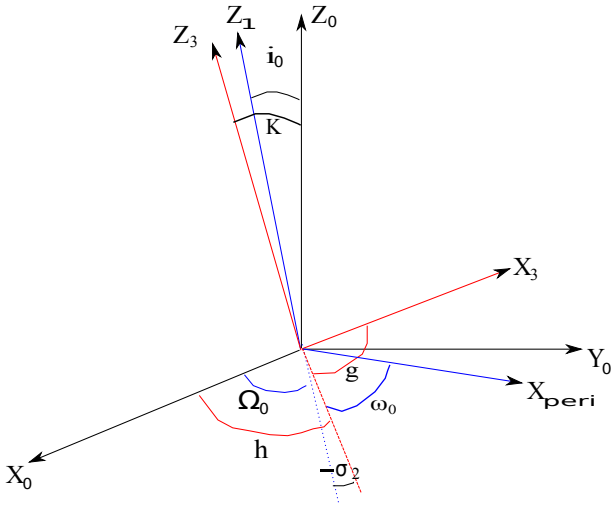

Figure 1.4: Vectors and angles involved in the Mercury rotation model.

Assuming no wobble motion, the rotational kinetic energy is:

$$T = \frac{\Lambda_1^2}{2C_m} \,, \tag{1.7}$$

where Λ_1 is the rotational angular momentum magnitude. In addition to this kinetic energy, the gravitational potential of the Sun (in fact the effective part on the rotation) is:

$$V_G = \frac{GM_S M\, R^2}{r^3}\left(-\frac{3}{2}C_{20}\frac{(x^2+y^2)}{r^2} + 3C_{22}\frac{(x^2-y^2)}{r^2}\right) \,, \tag{1.8}$$

where G is the gravitational constant, M_S and M are the masses of the Sun and Mercury, R is the mean radius of Mercury, (x,y,z) is the Mercury-Sun vector in the body-fixed principal axes of inertia of Mercury and $r = \sqrt{x^2+y^2+z^2}$ is the Sun-Mercury distance.

If the Mercury-Sun vector (x_i, y_i, z_i) is expressed in the Ecliptic J2000 inertial reference system, to obtain the coordinates x, y and z of the Sun in the body-fixed reference frame of Mercury 3 rotations have to be performed:

$$\begin{pmatrix} x \\ y \\ z \end{pmatrix} = R_3(g)R_1(K)R_3(h) \begin{pmatrix} x_i \\ y_i \\ z_i \end{pmatrix} , \tag{1.9}$$

where $R_i(\alpha)$ is the matrix representing a positive rotation of α about the i-th axis $(i = 1, 2, 3)$. This way, the variables used to describe the rotational motion appear in the potential V_G. Finally, using the Hamiltonian of the system:

$$H = T + V_G, \tag{1.10}$$

and introducing the canonical variables $\lambda_1 = g + h$, $\lambda_2 = -h$, $\Lambda_2 = \Lambda_1(1 - \cos K)$, since $\cos K = 1 - \Lambda_2/\Lambda_1$ the rotational motion of the system can be written in the Hamiltonian form:

$$\begin{aligned} \frac{d\,\lambda_1}{d\,t} &= \frac{\partial H}{\partial \Lambda_1}\,, \qquad \frac{d\,\Lambda_1}{d\,t} = -\frac{\partial H}{\partial \lambda_1}\,, \\ \frac{d\,\lambda_2}{d\,t} &= \frac{\partial H}{\partial \Lambda_2}\,, \qquad \frac{d\,\Lambda_2}{d\,t} = -\frac{\partial H}{\partial \lambda_2}\,, \end{aligned} \tag{1.11}$$

from which we can obtain the differential equations for g, h and also K.

The Hamiltonian system (1.11) has an expected secular equilibrium condition which correspond to the 3 : 2 spin-orbit resonance and the third Cassini's law. Writing the libration angle as $\sigma_1 = \lambda_1 - 3M/2 - \omega_0 - \Omega_0$ and the precession resonant angle $\sigma_2 = \lambda_2 + \Omega_0$ (see Fig. 1.4), the secular equilibrium condition is such that the values of σ_1 and σ_2 averaged over the angular orbital elements and the planetary terms are zero.

The choice of the initial conditions for these angles g_0, h_0, K_0 and of the angular momentum $\Lambda_{1\,0}$ is crucial if we want to reproduce the rotation of Mercury taking into account the secular equilibrium condition (spin-orbit 3 : 2 + Cassini state 1) and the short-term perturbations (librations in longitude and latitude) around it. In fact, being the equilibrium condition computed averaging over long time scales, its value should be computed using a rigid model. We will discuss this problem in the next Sec. 1.2.3.

Choosing the initial conditions close to the equilibrium of the system (1.11) (multi-layer model), and damping the free oscillations by the addition of a dissipation term, the main results for the short period librations of the rotation of Mercury are obtained numerically integrating (1.11) over thousands of years, and are of three types (see [Dufey et al. 2009, Sec. 5.2]):

- Longitudinal librations from the resonant argument σ_1,

- Librations of the argument σ_2, related to the precessional motion and the Cassini state,
- Latitudinal librations from the ecliptic obliquity K.

The numerical values for the constants used in the numerical integration are $C_{20} = -6\times10^{-5}$, $C_{22} = 1\times10^{-5}$ and $C_m = 0.19686$, corresponding to a value of $(B-A)/C_m = 2.0319\times10^{-4}$. The reference values being $C_m/C = 0.579$ and $C/MR^2 = 0.34$.

The frequency analysis performed to the solution shows that the periodic perturbation terms in the librations in σ_2 and K are well below the arcsec level. The significant effects are in the longitudinal librations σ_1: the results from the numerical study ([Dufey et al. 2009], Tab. 4, 5, 6) show that the main terms are the 88-day forced term due to the orbital motion of Mercury, with an amplitude of ~ 35 arcsec, and the planetary terms due to Jupiter (largest effect), Venus and Saturn.

The corresponding analytical study ([Dufey et al. 2009], Sec. 5.1, Tab. 1, 2, 3), mostly coincides with the numerical one apart from some critical terms present in the frequency analysis of σ_2 and K. They have a period of ~ 63000 years and an amplitude of few arcsec, terms which cannot appear in the numerical study. It is claimed in the paper that this analysis is not reliable for low frequencies, considered the problem of modeling Mercury as a rigid or multi-layer body over different time scales. It might happen that the numerical approach leaves some significant terms unmodeled in the rotation, and so it remains unsolved the problem of how to model Mercury for intermediate time scales. Possible experimental solutions to this problem are discussed in Section 1.2.3. The analytical results for σ_1 are very similar to the ones obtained in [Yseeboodt et al. 2010] if we approximate the orbital elements ℓ, Ω_0 and ω_0 as linear functions of time.

1.2.3 Choice of the initial conditions: an hybrid rotation model

The problem of the choice of the initial conditions for the rotational equations (1.11) consists in combining together the rigid body model for the long period behavior and the multi-layer model for the short-term behavior. In other words, the problem is to find the physical and mathematical dependence of the system (1.11) from the moment of inertia C (or C/MR^2). A possible solution to this problem is described in [Noyelles & D'Hoedt 2011], where a fitted precessional motion of Mercury is suitably included in averaged rotational equations for a rigid Mercury. In this way the laws ruling the behavior of the obliquity over long time scales are simulated and they can be used also in the short-term model of Sec. 1.2.2 under the form of initial conditions.

However, discussing the limitations and the difficulties in the dynamical theory for the rotation of Mercury is beyond the purpose of this thesis, which is dedicated to the feasibility of the *gravimetry-rotation* joint experiment. The aim of this work is not to describe how we can determine the rotation model, but to establish what can be determined by the experiments and thus to constrain the rotation model.

Chapter 2

Determination of the rotation state of Mercury from satellite gravimetry

Outline. In this Chapter we analyze the problem of the determination of the rotation state of Mercury and the state of its core. In Sec. 2.1 the main methods used to solve this problem are considered, focusing on pure gravimetry. In Sections 2.2 and 2.4 some important theoretical aspects of the problem are discussed. Sec. 2.3 is dedicated to a simplified model useful to reach some analytical results. Sec. 2.5 describes the Mercurycentric dynamics of a spacecraft (s/c) in details. Finally, in Sec. 2.6 and 2.7 the results of a numerical simulation for orbit determination and parameter estimation are presented, i.e. the rotation state of Mercury from satellite gravimetry by a global least squares fit analysis.

2.1 Possible methods for the determination of the rotation of Mercury and the state of its core.

As mentioned in the previous Chapter, the "Peale's experiment" ([Peale 1988]) proposes to determine the state of Mercury's core, in terms of the ratio C_m/C, by determining Mercury's rotation, through the obliquity η and the libration in longitude amplitude ϵ, and Mercury's gravity field, through the potential coefficients C_{20} and C_{22}.

After [Wu et al. 1995], where a possible experiment for the determination of the rotation of Mercury by a lander-orbiter system is investigated, a few other possible methods for have been considered in the last decades:

1. Radar observations of the surface of the planet from the Earth;
2. Pure satellite gravimetry by tracking of an orbiter around Mercury from the Earth;

3. On board high-resolution camera imaging combined with satellite gravimetry by tracking of an orbiter around Mercury from the Earth.

Method number 1 was proposed by [Margot et al. 2007], while methods 2 and 3 were first proposed and studied in [Milani et al. 2001] and [Sanchez et al. 2006]. The main features of these three methods are described in the following.

2.1.1 Radar observations of the surface from the Earth

According to [Margot et al. 2007], it is possible to determine the rotation state of the planet Mercury by direct radar measurements from Earth stations.

Citing from the paper: "radar echoes from solid planets exhibit spatial irregularities in the wavefront caused by the constructive and destructive interference of waves scattered by the irregular surface. Because of the rotation of the planet, the corrugations in the wavefront, also called speckles, will sweep over the receiving station and give rise to fluctuations of the electromagnetic signal with time. Observations of radar speckle patterns tied to the rotation of Mercury establish that the planet occupies a Cassini state with obliquity of 2.11 ± 0.1 arc minutes. The measurements show that the planet exhibits librations in longitude that are forced at the 88-day orbital period, as predicted by theory. The large amplitude of the oscillations, 35.8 ± 2 arc seconds, together with the Mariner 10 determination of the gravitational harmonic coefficient C_{22} ([Anderson et al. 1987]), indicates that the mantle of Mercury is decoupled from a core that is at least partially molten".

2.1.2 Pure remote gravimetry

This method is based on the classical tools of satellite geodesy [Kaula 1966], applied on a satellite orbiting around another planet instead of the Earth (see also [Milani & Gronchi 2010, Chap. 17]).

A static rigid body distributed in a region W generates outside W a potential V. With the center of mass in the origin of the adopted reference frame, using spherical coordinates (r, θ, λ), V can be expanded in a spherical harmonics series:

$$V(r,\theta,\lambda) = \frac{GM}{r} + \sum_{l=2}^{+\infty} \frac{GMR^l}{r^{l+1}} \sum_{m=0}^{l} P_{lm}(\sin\theta)[C_{lm}\cos m\lambda + S_{lm}\sin m\lambda]\,, \qquad (2.1)$$

where P_{lm} are the Legendre associated functions and M, R are the planet's mass and mean radius. C_{lm}, S_{lm} are the potential coefficients, whose values depend on the choice of the "body-fixed" reference system. In this way, the orbit of a satellite around the body contains information about C_{lm}, S_{lm}, and measuring accurately enough the orbit, it is possible to solve for them by a least squares fit. Notice that the orbit determination and the gravity field determination are in general not independent, and that other effects such as non gravitational perturbations may have to be considered. This means that in general the orbit determination and parameter estimation must be done by a global least squares fit ([Milani & Gronchi 2010, Chap. 17]).

However, when the rotation state of the body is not well known, the (time dependent) rotation matrix $R = R(t)$ converting from an inertial reference system to a body-fixed one contains uncertain parameters. For example, the approach described in Sec. 1.1 and 1.2 gives a (time dependent) rotation matrix that depends on the unknown obliquity η and the libration in longitude amplitude ϵ: $R = R(\eta, \epsilon, t)$. A different approach like the one in subsection 1.2.2 gives a rotation matrix that depends on more parameters such as GM of Mercury, C_{20}, C_{22} and the moments of inertia C, C_m: $R = R(g, K, h) = R(GM, C_{20}, C_{22}, C, C_m, t)$. In this case the orbit of a satellite around the body contains also information about the rotation parameters. A global orbit determination and parameter estimation process could solve for the unknown parameters. The feasibility and the quality of this parameter estimation is highly affected by the quality of the experimental data and by the intrinsic rank deficiencies that can occur, depending on the interactions between the dynamical and the observation model.

In order to simulate an orbit determination and parameter estimation experiment, we need to set up an observation model along with a dynamical model. Then we can compute the predicted values for the observations to compare with the simulated observational data in a global least squares fit (see 2.1.4). The two main observational techniques used for the orbit determination of an Earth satellite are the classical optical observations (right ascension and declination) and the radar observations (range and range rate). The case of a satellite orbiting around another planet, such as in the *MORE* experiment, is complicated by many factors, but in principle the technique can be simply considered as a tracking from an Earth-based station, giving range and range rate information (more details are in [Iess & Boscagli 2001]).

An overview of the dynamical model used to compute the observable quantities is showed in Fig. 2.1. To compute the range distance from the Earth ground station to the s/c around Mercury, and the corresponding range rate, we need to compute the following state vectors:

- the Mercurycentric position of the s/c $\mathbf{x}_{sat}$,
- the Solar System barycentric positions of Mercury and of the Earth-Moon barycenter (EMB) $\mathbf{x}_M$ and $\mathbf{x}_{EM}$,
- the Geocentric position of the ground antenna $\mathbf{x}_{ant}$,
- the position of the Earth barycenter with respect to the Earth-Moon barycenter $\mathbf{x}_E$.

We refer to Sec. 2.5 and to the Appendices A and B for a discussion on these dynamical and observation models.

2.1.3 High resolution camera imaging and remote gravimetry

Being the determination of the rotation of Mercury one of the main goals of the Bepi-Colombo mission, an additional support has been projected for the experiment. Remain-

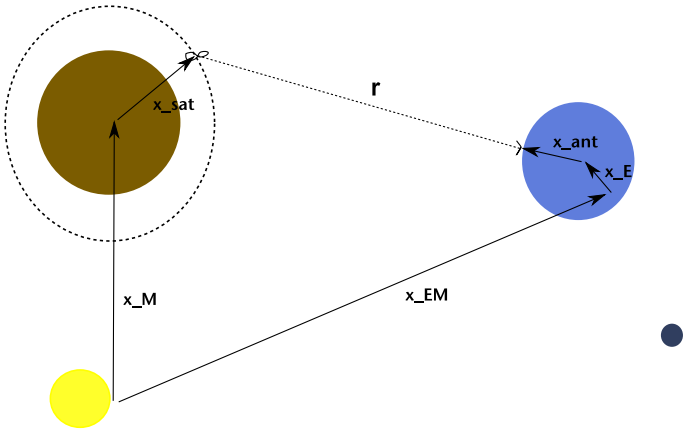

Figure 2.1: Multiple dynamics for the tracking of the s/c around Mercury from the Earth: $\mathbf{x}_{sat}$ is the Mercurycentric position of the s/c, $\mathbf{x}_M$ and $\mathbf{x}_{EM}$ are the Solar System barycentric positions of Mercury and of the Earth-Moon barycenter, $\mathbf{x}_{ant}$ is the Geocentric position of the ground antenna and $\mathbf{x}_E$ is the position of the Earth barycenter with respect to the Earth-Moon barycenter.

ing unchanged all the features of the method using only gravimetry (i.e. only tracking) described above, it is possible to add information on the rotation of Mercury by directly observing the planet surface.

A high resolution camera is expected to be on-board for mapping the planet [Marra et al. 2005], and it will repeatedly look at a number of patches on the surface. The pointing direction of the camera will be well known, because a star mapper will define the orientation of the s/c in a stellar reference frame, which in turn is related to an inertial frame by star catalogs. This can allow to compute the direction from the s/c to a specific footprint on the surface, and by correlating two images it is possible to directly measure the rotation of the planet in an inertial frame (see [Balogh et al. 2000], [Milani et al. 2001], Fig. 2.2).

The following content of this Thesis is dedicated to a rigorous study of all the experimental and main theoretical aspects of the method 2, which is analogous to the BepiColombo *MORE* experiment. The main point of this Thesis is to claim how good would be the determination of the rotation of Mercury, and of the state of its core, in the case we couldn't use the direct observations of the surface provided by the on-board camera.

In order to answer this question we will consider both a simplified model to obtain analytical results, and we will setup a full cycle numerical simulation of the Radio Science Experiment.

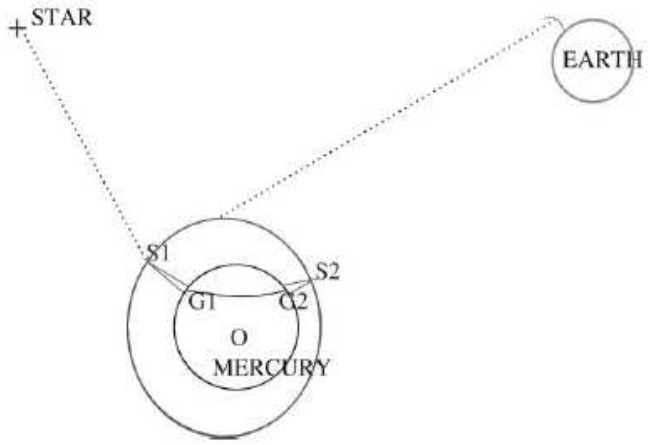

Figure 2.2: Geometry of the rotation experiment. The on-board camera, when the s/c is at S1, S2, takes images of a patch on the surface of Mercury around the points G1, G2 respectively, at times selected in such a way that these two points correspond to the same place on the surface. The tracking of the s/c from the Earth does not need to be done simultaneously. (Figure from [Milani et al. 2001])

2.1.4 Least squares

In the following we will consider as well known the least squares method as the preferred tool to process observational data [Milani & Gronchi 2010, Chap. 5 and 6]. We briefly introduce the main definitions and notations. Starting from a set of m observations $\mathcal{O}$, thanks to an observational model and a dynamical model it is possible to compute a set of corresponding computed observables $\mathcal{C}(\mathbf{X})$, which depend on a certain number of parameters $\mathbf{X}$. The optimal value $\mathbf{X}^*$ for the parameters is the minimum of the target function $Q(\boldsymbol{\xi}(\mathbf{X}))$, where $\boldsymbol{\xi}(\mathbf{X}) = \mathcal{O} - \mathcal{C}(\mathbf{X})$ are the residuals and Q is a quadratic form in $\boldsymbol{\xi}$. Typically

$$Q(\boldsymbol{\xi}(\mathbf{X})) = \frac{1}{m}\boldsymbol{\xi}^T W \boldsymbol{\xi} = \frac{1}{m}\sum_{i=1}^{m}\sum_{k=1}^{m} w_{ik}\xi_i\xi_k \ ,$$

where $W = (w_{ik})$ is the *weight matrix*, a symmetric matrix with non negative eigenvalues used to weight the residuals (i.e. the observations). The minimum of the target function is then found by an iterative *differential corrections* method (which is a variant of the Newton method):

$$\mathbf{X}_{k+1} = \mathbf{X}_k - C^{-1}B^T W \boldsymbol{\xi} \ ,$$

where

$$B = \frac{\partial \boldsymbol{\xi}}{\partial \mathbf{X}}(\mathbf{X}_k) \ , \qquad C = B^T W B \ ,$$

are the *design matrix* and the *normal matrix*. The inverse of the normal matrix $\Gamma = C^{-1}$ has a precise interpretation as *covariance matrix* if we consider the vector $\mathbf{X}$ as a multivariate Gaussian distribution with mean $\mathbf{X}^*$ in the space of parameters.

2.2 Gravity field and rotation state: symmetries and undetermined coefficients

Besides the harmonic coefficients, the internal mass distribution of a planet also defines the inertia tensor $\mathbf{T} = (I_{ij})$. Let us consider, at the same time and in the same reference system, the inertia tensor and the set of five potential coefficients of degree $l = 2$. It can be shown [Milani & Gronchi 2010, Chap. 13] that the following relations hold:

$$C_{20} = \frac{1}{MR^2}\left(\frac{I_{11}+I_{22}}{2} - I_{33}\right),\ C_{22} = \frac{(I_{22}-I_{11})}{4MR^2},$$

$$C_{21} = -\frac{I_{13}}{MR^2},\ S_{21} = -\frac{I_{23}}{MR^2},\ S_{22} = -\frac{I_{12}}{2MR^2}.$$

Thus, knowing the potential coefficients is not enough to know the inertia tensor, because there are five equations in six unknowns. That is, there is a one-parameter symmetry group, by which a change of the inertia tensor of the form

$$\mathbf{T} \longrightarrow s\mathbf{Id} + \mathbf{T}\ ,$$

where $\mathbf{Id}$ is the unit matrix, does not change the potential coefficients. If A, B, C are the principal moments of inertia of the body, the symmetry changes A, B, C by the same additive constant: $A \to A + s$, $B \to B + s$, $C \to C + s$.

In general, the one-parameter symmetry can be broken if we find another independent equation for A, B, C. In the case of Mercury, if we consider decoupling between core and mantle, a further equation is needed to find the parameter C_m. According to [Peale 1988] this can be done if we know the rotation state of the body and the torque acting on it. The problem is then determining the rotation state from the gravity field.

In fact, knowing the gravity field is enough to determine the principal of inertia axes, because they are the same for $\mathbf{T}$ and $s\mathbf{Id} + \mathbf{T}$. At a fixed time, we can diagonalize the tensor $\mathbf{T}$ and find the directions of the principal of inertia axes. In the case of a triaxial body ($A < B < C$), this defines instantaneously the rotation state of the body. On the contrary, in case of some rotational symmetry, ($A = B < C$) or ($A = B = C$), it would be clearly impossible to discriminate a rotation around the symmetry axis (or axes) since the gravity field does not change. As discussed in [Milani & Gronchi 2010, Chap. 6], when the rotation symmetry is broken for a realistic planet, there is still an approximate symmetry that could be significant.

2.3 Analytical study: the model problem

In this Section we set up a simplified model to obtain analytically some results on the determination of the rotation of Mercury from the gravity field.

2.3.1 Rotation of the gravity field

The spherical harmonics development (2.1) describes the gravity field generated by a rigid mass with respect to a body-fixed reference frame. If we consider the same development with respect to a reference frame in which the mass is rigidly rotating, formula (2.1) is valid instantaneously, and we can use it introducing time dependence in the coefficients:

$$V(r,\theta,\lambda,t) = \frac{GM}{r} + \sum_{l=2}^{+\infty} \frac{GMR^l}{r^{l+1}} \sum_{m=0}^{l} P_{lm}(\sin\theta)[\tilde{C}_{lm}(t)\cos m\lambda + \tilde{S}_{lm}(t)\sin m\lambda]. \quad (2.2)$$

If the mass is rotating around a fixed axis $\mathbf{V}_s$, whose inertial direction is given by two angles (η,ξ) (e.g. η colatitude), and that $\phi = \phi(t)$ is the rotation angle, then the rotation from the inertial to the body-fixed system is the composition of a rotation of η around axis-2, a rotation of ξ around axis-1 and a rotation of ϕ around axis-3.

If C_{lm}, S_{lm} are the potential coefficients in a body-fixed system (uniquely determining the gravity field), then the explicit formulas for $\tilde{C}_{lm}(t), \tilde{S}_{lm}(t)$ as functions of C_{lm}, S_{lm} can be obtained either by the methods of spherical trigonometry (e.g. [Kaula 1966]) or from the representation theory of the rotation group $SO(3)$ into the spherical harmonic space of degree l [Wigner 1959].

In the following we present the explicit formulas for degree $l = 2$, assuming also $\xi = 0$ and η small:

$$\begin{aligned}
\tilde{C}_{20} &= C_{20} - 3\eta C_{21}\cos\phi + 3\eta S_{21}\sin\phi + \mathcal{O}(\eta^2), && (2.3)\\
\tilde{C}_{21} &= \eta C_{20} - 2\eta C_{22}\cos 2\phi + 2\eta S_{22}\sin 2\phi + C_{21}\cos\phi + S_{21}\sin\phi + \mathcal{O}(\eta^2), && (2.4)\\
\tilde{C}_{22} &= C_{22}\cos 2\phi - S_{22}\sin 2\phi + \frac{1}{2}\eta C_{21}\cos\phi + \frac{1}{2}\eta S_{21}\sin\phi + \mathcal{O}(\eta^2), && (2.5)\\
\tilde{S}_{21} &= -2\eta C_{22}\sin 2\phi - 2\eta S_{22}\cos 2\phi + C_{21}\sin\phi + S_{21}\cos\phi + \mathcal{O}(\eta^2), && (2.6)\\
\tilde{S}_{22} &= C_{22}\sin 2\phi + S_{22}\cos 2\phi + \frac{1}{2}\eta C_{21}\sin\phi + \frac{1}{2}\eta S_{21}\cos\phi + \mathcal{O}(\eta^2). && (2.7)
\end{aligned}$$

We will assume as rotation angle:

$$\phi = \frac{3}{2}\ell + \epsilon\sin\ell, \quad (2.8)$$

where ℓ is the mean anomaly of Mercury and ϵ the libration in longitude amplitude. For the purpose of the analytic study, we have neglected the $\sim \sin 2\ell$ term appearing in (1.4) because it is smaller. In this way ϵ appears in the equations (2.3) through the angle ϕ. A first order approximation in the couple of parameters η, ϵ is also considered.

2.3.2 Simplifying assumptions

In order to be able to handle the problem analytically, we must make some approximations:

Inertial reference system. We use as inertial reference system the system $(\mathbf{X}_1, \mathbf{Y}_1, \mathbf{Z}_1)$ defined in 1.1.1.

Rotation State. Mercury is rotating around an inertially fixed axis $\mathbf{V}_s$ by the rotation angle ϕ. The rotation from the inertial to the body-fixed system is given by a rotation of an angle η (the obliquity) around axis-2 and a rotation of ϕ around axis-3. Consistently with Sec. 1.2.1, the formula for the angle ϕ is given by (2.8). We also assume that the body-fixed reference system is principal of inertia.

Gravity field. We consider in the spherical harmonics series of the gravity potential truncated to degree $l = 2$. Given that the body-fixed reference frame is principal of inertia, the only parameters appearing in the right hand side of equations (2.3) are C_{20} and C_{22} (which represent the oblateness and the equatorial ellipticity), the obliquity η and the libration amplitude ϵ through the angle ϕ.

Reference satellite orbit. Finally, in order to describe analytically the perturbed orbit of the satellite by a first order theory, we define a reference unperturbed orbit. We define a circular reference orbit of radius r_0, inclination $I = \pi/2$ and longitude of the ascending node Ω with respect to the frame $(\mathbf{X}_1, \mathbf{Y}_1, \mathbf{Z}_1)$. We indicate with ν the true anomaly of the satellite. $t = 0$ is the time of perihelion passage and we assume also $t_0 = 0$ the initial time of the satellite orbit. We also indicate with n_s the satellite mean motion while n is the mean motion of Mercury.

Notice that the hypothesis of nearly polar orbit is a very good approximation of the expected inclination of the BepiColombo s/c around Mercury. The hypothesis of circular orbit is a less accurate approximation, since the real orbit is expected to have an eccentricity of ~ 0.16.

2.3.3 Hill's equations

Let $(\mathbf{r}_0, \mathbf{v}_0)$ be a reference satellite in a circular orbit with radius r_0, with local coordinates in the radial $\hat{\mathbf{r}}_0$, along-track $\hat{\mathbf{v}}_0$ and out of plane $\hat{\mathbf{w}}_0 = \hat{\mathbf{r}}_0 \times \hat{\mathbf{v}}_0$ direction respectively (RTW coordinates). Let the perturbing potential be $\mathcal{D} = V - GM/r$, small compared to the monopole term GM/r. We can describe the perturbed satellite relative motion $(\mathbf{r} - \mathbf{r}_0, \mathbf{v} - \mathbf{v}_0)$, assuming $\mid r - r_0 \mid << r_0$, through the so called *Hill's equations* [Dunning 1973]:

$$\begin{cases} \ddot{u} - 2n_s\dot{v} - 3n_s^2 u = f_u \\ \ddot{v} + 2n_s\dot{u} = f_v \\ \ddot{w} + n_s^2 w = f_w \end{cases}$$

where $[\mathbf{r}]_{RTW} = (r_0 + u, v, w)$, $[\mathbf{v}]_{RTW} = (\dot{u} - n_s v, \dot{v} + n_s(r_0 + u), \dot{w})$, $n_s = \sqrt{GM/r_0^3}$ is the reference mean motion and (f_u, f_v, f_w) is the perturbing force, i.e. the gradient of the perturbing potential $\mathcal{D}$ calculated in the reference satellite position.

Combining formulas (2.2), (2.3), (2.8) and the simplifying assumptions above, we have:

$$\mathcal{D} = \mathcal{A}_1 + \sum_{i=2}^{11}(\mathcal{A}_i \cos(\alpha_i \nu + \beta_i \ell) + \mathcal{B}_i \sin(\alpha_i \nu + \beta_i \ell)) \,, \tag{2.9}$$

where $\alpha_i \in \{0, 2\}$ and $\beta_i \in \{0, \pm 2, \pm 3, \pm 4\}$ in all the possible combinations with α_i, β_i not simultaneously zero. $\mathcal{A}_i, \mathcal{B}_i$ are known functions of C_{20}, C_{22}, η, ϵ, r_0 and Ω, while the frequencies $\sigma_i = \alpha_i n_s + \beta_i n$, including also the zero frequency, are summarized in Tab. 2.1.

Table 2.1: The 11 frequencies appearing in the perturbing potential $\mathcal{D}$.

$\sigma_1 = 0$	$\sigma_2 = 2n_s$	$\sigma_3 = 2n_s + 2n$
$\sigma_4 = 2n_s + 3n$	$\sigma_5 = 2n_s + 4n$	$\sigma_6 = 2n_s - 2n$
$\sigma_7 = 2n_s - 3n$	$\sigma_8 = 2n_s - 4n$	$\sigma_9 = 2n$
$\sigma_{10} = 3n$	$\sigma_{11} = 4n$	

Finally, the perturbing force is:

$$f_u = \frac{\partial \mathcal{D}}{\partial r_0}; \quad f_v = \frac{1}{r_0}\frac{\partial \mathcal{D}}{\partial \nu}; \quad f_w = -\frac{1}{r_0 \cos\nu}\frac{\partial \mathcal{D}}{\partial \Omega}. \tag{2.10}$$

2.3.4 Rotation from gravimetry analytical results

From a comparison of the expected accuracies for the range and rage-rate measurements of the BepiColombo mission (see Sec. 2.6.2), it turns out that the gravimetry experiment is performed mainly with the range-rate, being more accurate than the range in measuring short term changes. Thus, we will focus only on the perturbed velocity $\mathbf{v} - \mathbf{v}_0$ and in particular on the along-track component $\dot{v} + n_s u$. From formulas (2.10) we deduce that f_u and f_v are of the form:

$$f_u = A_1 + \sum_{i=2}^{17}(A_i \cos(\sigma_i t) + B_i \sin(\sigma_i t)), \tag{2.11}$$

$$f_v = \sum_{i=2}^{17}(C_i \cos(\sigma_i t) + D_i \sin(\sigma_i t)), \tag{2.12}$$

where A_i, B_i, C_i, D_i are given by:

$$A_i = \frac{\partial \mathcal{A}_i}{\partial r_0} = -\frac{3}{r_0}\mathcal{A}_i, \qquad B_i = \frac{\partial \mathcal{B}_i}{\partial r_0} = -\frac{3}{r_0}\mathcal{B}_i, \tag{2.13}$$

$$C_i = \frac{1}{r_0}\alpha_i \mathcal{B}_i, \qquad D_i = -\frac{1}{r_0}\alpha_i \mathcal{A}_i. \tag{2.14}$$

Because Hill's equations are linear, it is possible to obtain a particular solution of the form:

$$\begin{aligned} u &= a_1 + \sum_{i=2}^{11}(a_i \cos(\sigma_i t) + b_i \sin(\sigma_i t)), \\ \dot{u} &= \sum_{i=2}^{11}(\tilde{a}_i \cos(\sigma_i t) + \tilde{b}_i \sin(\sigma_i t)), \end{aligned} \tag{2.15}$$

$$\begin{aligned} v &= \sum_{i=2}^{11}(c_i \cos(\sigma_i t) + d_i \sin(\sigma_i t)), \\ \dot{v} &= \sum_{i=2}^{11}(\tilde{c}_i \cos(\sigma_i t) + \tilde{d}_i \sin(\sigma_i t)), \end{aligned} \tag{2.16}$$

where

$$\begin{aligned} a_1 &= \frac{1}{r_0 n_s^2}\mathcal{A}_1, \\ b_1 = c_1 = d_1 = \tilde{a}_1 &= \tilde{b}_1 = \tilde{c}_1 = \tilde{d}_1 = 0, \end{aligned} \tag{2.17}$$

and $\forall i > 1$:

$$a_i = \frac{-3\sigma_i + 2n_s\alpha_i}{r_0\sigma_i(n_s^2 - \sigma_i^2)}\mathcal{A}_i, \tag{2.18}$$

$$b_i = \frac{-3\sigma_i + 2n_s\alpha_i}{r_0\sigma_i(n_s^2 - \sigma_i^2)}\mathcal{B}_i, \tag{2.19}$$

$$c_i = \frac{3n_s^2\alpha_i + \alpha_i\sigma_i^2 - 6n_s\sigma_i}{r_0\sigma_i^2(n_s^2 - \sigma_i^2)}\mathcal{B}_i, \tag{2.20}$$

$$d_i = -\frac{3n_s^2\alpha_i + \alpha_i\sigma_i^2 - 6n_s\sigma_i}{r_0\sigma_i^2(n_s^2 - \sigma_i^2)}\mathcal{A}_i, \tag{2.21}$$

$$\tilde{a}_i = \sigma_i b_i, \quad \tilde{b}_i = -\sigma_i a_i, \quad \tilde{c}_i = \sigma_i d_i, \quad \tilde{d}_i = -\sigma_i c_i. \tag{2.22}$$

The particular solution has to be summed to the homogeneous solution ($f_u = f_v = f_w = 0$):

$$\begin{aligned} u^0 &= -\frac{2}{3n}z_2 - \frac{1}{2}z_3 \cos n_s t - \frac{1}{2}z_4 \sin n_s t, \\ v^0 &= z_1 + z_2 t + z_3 \sin n_s t + z_4 \cos n_s t, \end{aligned}$$

to obtain a general solution. However, by definition, the homogeneous solutions does not contain the signal of the perturbation $\mathcal{D}$, it only contains the signal of the variations of the actual orbit with respect to the circular reference orbit. In particular, focusing on the along-track component, it contains the signal due to a variation in mean motion, initial phase angle, eccentricity and longitude of pericenter $e\sin\omega$, $e\cos\omega$.

To justify the validity of the Hill's equations for a long time span (e.g. one Mercury orbital period), we assume that we have a priori observed the orbit of the s/c for long enough to constrain the reference mean motion n_s and the initial phase to the real mean motion and initial phase. Moreover, we assume that the true orbit does not deviate too much from a circular one ($|\mathbf{v} - \mathbf{v}_0|/(n_s r_0) << 1$). Thus, we don't consider the homogeneous solution because it doesn't contain the signal of the perturbation, and to reach some analytical conclusions we concentrate our analysis on the solution $\dot{v} + n_s u$. We assume to be able to measure the corresponding signal with an accuracy $\delta_{\dot{v}}$, for a time span long enough to determine independently all the amplitudes $\tilde{c}_i + n_s a_i$, $\tilde{d}_i + n_s b_i$, with the same accuracy δ_a (actually, the constant term $n_s a_1$ with accuracy $\delta_a/2$). Then it is possible to compute the uncertainties in the determination of the parameters C_{20}, C_{22}, η, ϵ from the observation of the amplitudes of the signal $\dot{v} + n_s u$. The explicit formulas for the amplitudes $\tilde{c}_i + n_s a_i$, $\tilde{d}_i + n_s b_i$, are given in Tab. 2.2, where we have also used the following approximation ($n_s >> n$):

$$\frac{3n_s^2\alpha_i + \alpha_i\sigma_i^2 - 6n_s\sigma_i}{\sigma_i(n_s^2 - \sigma_i^2)} \cong -\frac{1}{3n_s} \qquad \text{for } i = 2, .., 8;$$

$$\frac{3n_s^2\alpha_i + \alpha_i\sigma_i^2 - 6n_s\sigma_i}{\sigma_i(n_s^2 - \sigma_i^2)} \cong -\frac{6}{n_s} \qquad \text{for } i = 9, 10, 11.$$

Table 2.2: Amplitudes of the along-track velocity perturbed signal. All the terms have to be multiplied by the factor $\frac{GMR^2}{r_0^4 n_s}$.

$n_s a_1 = \frac{1}{4} C_{20}$	
$\tilde{c}_2 + n_s a_2 = -\frac{1}{2} C_{20}$	$\tilde{d}_2 + n_s b_2 = \eta C_{20} \cos\Omega$
$\tilde{c}_3 + n_s a_3 = -\frac{1}{2}\epsilon C_{22} \cos 2\Omega$	$\tilde{d}_3 + n_s b_3 = -\frac{1}{2}\epsilon C_{22} \sin 2\Omega$
$\tilde{c}_4 + n_s a_4 = \eta C_{22} \sin\Omega + \frac{1}{2} C_{22} \cos 2\Omega$	$\tilde{d}_4 + n_s b_4 = -\eta C_{22} \cos\Omega + \frac{1}{2} C_{22} \sin 2\Omega$
$\tilde{c}_5 + n_s a_5 = \frac{1}{2}\epsilon C_{22} \cos 2\Omega$	$\tilde{d}_5 + n_s b_5 = \frac{1}{2}\epsilon C_{22} \sin 2\Omega$
$\tilde{c}_6 + n_s a_6 = -\frac{1}{2}\epsilon C_{22} \cos 2\Omega$	$\tilde{d}_6 + n_s b_6 = \frac{1}{2}\epsilon C_{22} \sin 2\Omega$
$\tilde{c}_7 + n_s a_7 = -\eta C_{22} \sin\Omega + \frac{1}{2} C_{22} \cos 2\Omega$	$\tilde{d}_7 + n_s b_7 = -\eta C_{22} \cos\Omega$
$\tilde{c}_8 + n_s a_8 = \frac{1}{2}\epsilon C_{22} \cos 2\Omega$	$\tilde{d}_8 + n_s b_8 = -\frac{1}{2}\epsilon C_{22} \sin 2\Omega$
$\tilde{c}_9 + n_s a_9 = -\frac{9}{2}\epsilon C_{22} \cos 2\Omega$	$\tilde{d}_9 + n_s b_9 = \frac{9}{2}\epsilon C_{22} \sin 2\Omega$
$\tilde{c}_{10} + n_s a_{10} = \frac{9}{2} C_{22} \cos 2\Omega$	$\tilde{d}_{10} + n_s b_{10} = \frac{9}{2} C_{22} \sin 2\Omega$
$\tilde{c}_{11} + n_s a_{11} = \frac{9}{2}\epsilon C_{22} \cos 2\Omega$	$\tilde{d}_{11} + n_s b_{11} = \frac{9}{2}\epsilon C_{22} \sin 2\Omega$

We immediately deduce from Tab. 2.2 that the rotation parameters appear in the potential always multiplied by the potential coefficients. This is the approximated symmetry that we have introduced in Sec. 2.2, by which the smaller are the potential coefficients the weaker is the signal of the rotation in the gravity field. Moreover, assuming low correlations between the gravity field and the rotation parameters, justified by the fact that C_{20}, C_{22} also appear independently from the rotation parameters at

frequencies $2n_s$ and $3n$ with phase $\pi/2$, the formal uncertainty (standard deviation) associated to the determination of each parameter of interest x, can be approximated by:

$$\sigma_x \cong \frac{\delta_a}{\sqrt{\sum_{i=1}^{11} \left(\frac{\partial(\tilde{c}_i + n_s a_i)}{\partial x}\right)^2 + \left(\frac{\partial(\tilde{d}_i + n_s b_i)}{\partial x}\right)^2}}. \tag{2.23}$$

Finally, applying formula (2.23) to C_{20}, C_{22}, η and ϵ we obtain the following approximate results for the determination of the rotation state of Mercury from the gravity field:

$$\sigma_\eta \cong \frac{\sqrt{3/8}}{\sqrt{\cos\Omega^2 + 2(C_{22}/C_{20})^2}} \frac{\sigma_{C_{20}}}{C_{20}}, \tag{2.24}$$

$$\sigma_\epsilon \cong \frac{\sqrt{2}}{2} \frac{\sigma_{C_{22}}}{C_{22}}. \tag{2.25}$$

2.4 Rank deficiency in the orbit determination around another planet

When the orbit determination of an object orbiting around another planet is performed by radial and radial velocity observations (e.g. using radar), there is an important symmetry responsible for the weakness of the orbit determination that is an approximate version of the exact symmetry found in [Bonanno & Milani 2002]. In our case, if the Mercurycentric orbit is rotated around an axis $\hat{\boldsymbol{\rho}}$ in the direction from the Earth to the center of Mercury, then there would be an exact symmetry in the range and range-rate observations if $\hat{\boldsymbol{\rho}}$ were constant and Mercury spherical. Given that $\hat{\boldsymbol{\rho}}$ changes with time, the small parameter in the approximate symmetry is the displacement angle by which $\hat{\boldsymbol{\rho}}$ rotates (in an inertial reference system) during the observation arc time span. The weak directions $\hat{\mathbf{w}}_{dp}$ and $\hat{\mathbf{w}}_{dv}$ of the orbit determination in the 3-dimensional subspaces of the s/c initial position $\mathbf{r}_0$ and velocity $\mathbf{v}_0$, are given by:

$$\hat{\mathbf{w}}_{dp} = \frac{\hat{\boldsymbol{\rho}} \times \mathbf{r}_0}{|\hat{\boldsymbol{\rho}} \times \mathbf{r}_0|}, \qquad \hat{\mathbf{w}}_{dv} = \frac{\hat{\boldsymbol{\rho}} \times \mathbf{v}_0}{|\hat{\boldsymbol{\rho}} \times \mathbf{v}_0|}. \tag{2.26}$$

Different solutions can be adopted to stabilize the solution for the local parameters. A set of a priori observations weakly constraining the initial conditions (with an uncertainty of 3 m in position and 3 m/day in velocity) would be enough to stabilize the solution [Milani et al. 2001]. As an alternative approach, the initial conditions for two consecutive arcs could be weakly constrained together, by using a covariance matrix for the prediction at the next day enlarged[1] with respect to the deterministic covariance propagation of [Milani & Gronchi 2010, Chap. 5]. Possible strategies are discussed in Sec. 2.6.3, and they are applied in the full scale simulations described in Sec. 2.6.

[1] This approach is closely related with the Kalman filter class of algorithms.

We now step into the description of a realistic dynamical model of a s/c around Mercury. The rest of the dynamical model and of the observational model are described in the Appendices A and B.

2.5 Realistic Mercurycentric dynamics

Let $\mathbf{r}$ be the Mercurycentric position of the s/c and $\mathbf{a}$ its acceleration with respect to an inertial reference system (e.g. the Ecliptic J2000). Then $\mathbf{a} = \mathbf{F}/m$ where $\mathbf{F}$ is the force exerted on the s/c and m is its mass. The orbit of a s/c around Mercury has an equation of motion $\ddot{\mathbf{r}} = \mathbf{a}$ which must contain: the spherical harmonics of the Mercury gravity field; the solar and planetary differential attractions and tidal perturbations; the non gravitational perturbations, possibly replaced by on-board accelerometer readings; relativistic corrections.

Let $\mathbf{r}_{IN}$ and $\mathbf{r}_{BF}$ be the s/c coordinates with respect to the inertial and the body-fixed reference system respectively. The coordinates of the acceleration due to the static gravity field of Mercury in the body-fixed system are $\mathbf{a}_{BF} = \nabla V(\mathbf{r}_{BF})$, where V is the gravitational potential given by formula (2.1). If R is the rotation matrix that converts from the inertial to the body-fixed coordinates, we have: $\mathbf{r}_{BF} = R\,\mathbf{r}_{IN}$, $\mathbf{a}_{BF} = R\,\mathbf{a}_{IN}$ and $\mathbf{a}_{IN} = R^T \nabla V(R\,\mathbf{r}_{IN})$.

2.5.1 Rotational dynamics: semi-empirical model

For the computation of the rotation matrix R, we use a semi-empirical model: an explicit analytical formula for the rotation of Mercury is obtained combining the discussions in Sec. 1.1 (direction of the spin axis) and in Sec. 1.2.1, 1.2.2 (librations in longitude).

We use the reference systems defined in 1.1.1, where the body-fixed system considered Ψ_{BF} is the one with principal of inertia axes. The principal axis $\mathbf{X}_3$ is assumed as zero meridian. Let R_0 be the rotation matrix converting from the inertial Ecliptic J2000 $(\mathbf{X}_0, \mathbf{Y}_0, \mathbf{Z}_0)$ to the inertial orbital reference system $(\mathbf{X}_1, \mathbf{Y}_1, \mathbf{Z}_1)$.

Then we need to compute the rotation from the orbital to the body-fixed system (for time scales of the order of few years).

As a first approximation, we define the direction of the spin axis with respect to the orbital reference system by two constant angles (δ_1, δ_2):

$$[\mathbf{Z}_3]_1 = (\sin\delta_1 \cos\delta_2, -\sin\delta_2, \cos\delta_2 \cos\delta_1)^T.$$

The obliquity η is simply given by

$$\cos\eta = \cos\delta_2 \cos\delta_1\,. \tag{2.27}$$

In this way, the spin direction is "model independent", meaning that we solve for its direction without assuming Cassini state. In our simulation we chose the reference values for the direction of the spin axis in an arbitrary way, without assuming any knowledge of the Cassini plane from the theory.

If ϕ is the rotation angle, we define the rotation matrix R by:

$$R = R_3(\phi)R_1(\delta_2)R_2(\delta_1)R_0\,,$$

where $R_i(\alpha)$ is the matrix associated to the rotation by an angle α about the i-th axis ($i = 1, 2, 3$). The explicit formula for the rotation angle ϕ can be obtained from formula (1.6) keeping only the terms significant over a one year mission time span. In general it is the sum of a secular term, some periodic libration terms and a constant which depends on the choice of the zero meridian.

At this point, we need to specify what exactly we want to determine and what we do not. We've seen that, if the threshold of accuracy of the experiment is of the order of 1 arcsec, we would need to keep about ten trigonometric terms in the formula for ϕ. However, the largest effects are by far the following three:

- the main ~ 88 days term due to Mercury: $\epsilon_1 \sin(n\,t)$;
- the second harmonic term of ~ 44 days due to Mercury: $\epsilon_1/\mu \sin(2\,n\,t)$ where $\mu = -9.483$ from [Jehn et al. 2004] depends only on the eccentricity and it is considered here as a known constant;
- the ~ 11.8 years near resonant term due to Jupiter: $\epsilon_2 \cos(w_j\,t + \varphi_j)$;

while the other effects due to Venus, Earth and Saturn are smaller effects that it is impossible to determine independently in one year mission time span, because of the closeness of their periods and the smallness of their amplitudes. Since they are far from the resonance, a good nominal value for their amplitudes can be provided by the theory, and a possible small error in the nominal amplitudes can be absorbed by a constant (see the following discussion about the S_{22} coefficient). In order to simplify the analysis in this simulation, we have chosen not to add these effects at all.

The libration amplitudes that we want to determine in the simulated experiment are just ϵ_1 and ϵ_2. However, it is not obvious a priori under which conditions ϵ_2 can be determined with only few months observation time span, depending strongly on the magnitude of its amplitude and on the phase of the signal at the time of the simulation (see Sec. 2.7). The libration term with period ~ 88 days instead should be always detectable.

Finally, the analytical formula adopted for ϕ is:

$$\begin{aligned}\phi = {} & \frac{3}{2} n\,(t - t_p) + \epsilon_1 \sin(n\,(t - t_p)) + \\ & + \frac{\epsilon_1}{\mu} \sin(2\,n\,(t - t_p)) + \epsilon_2 \cos(w_j\,(t - t_p) + \varphi_j)\,,\end{aligned} \tag{2.28}$$

where we use as reference values for the frequencies n, w_j and the time of perihelion t_p the ones at epoch J2000. Because of the different reference time, the phase φ_j above is

shifted from the one given in Tab.1.1 by

$$\varphi_j \to \varphi_j + w_j(t_p - t_{J2000}) \cong -11.97^\circ.$$

It is important to notice that we haven't added any constant phase lag $\phi_0 = \phi(t_0)$ to be determined in the experiment. This is done on purpose, because of a rank deficiency that occurs when we try to solve also for the gravity field coefficient S_{22}. Being, by our definition, the rotation matrix R converting to the principal of inertia reference system Ψ_{BF}, the simulated values for the gravity field coefficients C_{lm}^{PI}, S_{lm}^{PI} have to be such that $C_{21}^{PI} = S_{21}^{PI} = S_{22}^{PI} = 0$. Let's suppose we are solving simultaneously for ϕ_0 and S_{22}, and let ζ be an error in ϕ_0. In this case, the coefficients S_{22} and C_{22} with respect to the reference system rotated by ϕ_0 are

$$S_{22} = C_{22}^{PI} \sin 2\zeta, \qquad C_{22} = C_{22}^{PI} \cos 2\zeta\,. \tag{2.29}$$

Thus, if ζ is small, as it should be if we are performing convergent differential corrections, we will have $C_{22} \cong C_{22}^{PI}$ and $S_{22} \cong 2\zeta C_{22}^{PI}$, giving a correlation between S_{22} and ϕ_0 equal to 1. The coefficient S_{22} and the constant phase angle ϕ_0 cannot be determined independently.

It follows that the value of S_{22} represents the offset of the axis of minimum moment of inertia of Mercury with respect to the zero meridian defined by $\phi_0 = \phi(t_0)$. In other words, if there is a constant (or quasi-constant) error ζ in the libration with respect to our model, then the value of S_{22} obtained by fitting the data should be different from zero consistently with formula (2.29). Moreover, all the other spherical harmonics coefficients should be consistent to the following formula ([Milani & Gronchi 2010, Chap. 13]):

$$\begin{pmatrix} C_{lm} \\ S_{lm} \end{pmatrix} = \begin{pmatrix} \cos(m\zeta) & -\sin(m\zeta) \\ \sin(m\zeta) & \cos(m\zeta) \end{pmatrix} \begin{pmatrix} C_{lm}^{PI} \\ S_{lm}^{PI} \end{pmatrix}. \tag{2.30}$$

The case in which the error ζ is not constant but it significantly changes in time, as it would be an error in the libration term due to Jupiter ϵ_2, is a little bit different and it will be discussed at the end of Sec. 2.7.

2.5.2 Sun, planetary and tidal perturbations

The Solar and planetary perturbative acceleration $\mathbf{a}_p$, on a satellite orbiting around Mercury, consist of a "third-body" relative term due to the Sun, Venus, Earth-Moon, Mars, Jupiter, Saturn, Uranus and Neptune:

$$\mathbf{a}_p = \sum_{bodies} GM_b\left(\frac{\mathbf{d}_b}{d_b^3} - \frac{\mathbf{x}_b}{x_b^3}\right), \tag{2.31}$$

where $\mathbf{d}_b$ is the position of a body (of mass M_b) with respect to the satellite and $\mathbf{x}_b$ is its position with respect to Mercury (see e.g. [Roy 2005]).

So far we have considered the rotation of a rigid body. If we introduce an elastic component and the body is subject to some external force, then it could be deformed. This is the case for Mercury under the tidal field of the Sun, the effect is a classic tidal bulge oriented, at each instant, in the direction of the Sun. This deformation changes the expression of the Newtonian potential V (formula (2.1)) by a quantity V_L called *Love potential* [Kozai 1965]:

$$V_L = \frac{GM_S k_2 R^5}{r_S^3 r^3}(\frac{3}{2}\cos^2\psi - \frac{1}{2}), \tag{2.32}$$

where M_S is Sun's mass, r_S is the Mercury-Sun distance and ψ is the angle between the s/c Mercurycentric position $\mathbf{r}$ and the Sun Mercurycentric position. The Love number k_2 is the elastic constant that characterizes the effect, for this simulation we have used a value 0.25.

2.5.3 Non gravitational perturbations and accelerometer

Being Mercury so close to the Sun, the solar radiation pressure at the planet is very high. Thus it must be considered as a source of perturbation to the orbit of the s/c, not only its direct component on the satellite, but also the reflected radiation from the planet surface (albedo radiation pressure).

The direct radiation pressure $\mathbf{a}_{rad}$ is modeled assuming a spherical satellite with coefficient 1 (neglecting the diffusive term, see [Milani et al. 1987]). The shadow of the planet is computed accurately, taking into account the penumbra effects. The albedo radiation pressure $\mathbf{a}_{alb}$ is described assuming a zero relaxation time for the thermal reemission on Mercury. In this simple setting we do not need information about the distribution of the albedo on the Mercury's surface since it is effectively equal to 1 (this model has been supplied by D. Vokrouhlicky, Charles University of Prague). We are not including thermal thrust and other indirect radiation pressure effects (see [Milani et al. 1987, Chap. 5]).

In general, modeling these non gravitational effects $\mathbf{a}_{ng} = \mathbf{a}_{rad} + \mathbf{a}_{alb}$ is difficult and the determination of the unknown parameters appearing in the equations is a tough problem. Trying to determine these parameters could degrade the results of the whole experiment, being the non gravitational effects poorly modeled.

It is possible to overcome this problem by using an on-board instrument called *accelerometer*, which measures differential accelerations between a sensitive element and its rigid frame (cage) (see [Iafolla and Nozzoli 2001] and [Milani & Gronchi 2010, Chap. 16]). Let $\mathbf{x}$ be the inertial position of the s/c center of mass (CoM), then, if V is the gravitational potential, the equation for $\mathbf{x}$ is:

$$\ddot{\mathbf{x}} = \nabla V(\mathbf{x}) + \mathbf{a}_{ng}. \tag{2.33}$$

In principle, since the non gravitational perturbations $\mathbf{a}_{ng}$ do not act on the sensitive element inside the cage, on condition that the accelerometer is placed in the CoM of the

s/c, the instrument measures the acceleration $\mathbf{a}_{acc} = -\mathbf{a}_{ng}$. Thus the non gravitational perturbations can be removed from the list of unknowns by replacing them with the reading of the on-board accelerometer. However, in doing this there are a number of things to take into account carefully.

First of all, the accelerometer cannot be placed exactly at $\mathbf{x}$, but at some position displaced by a vector $\mathbf{Y}$ from the CoM in a s/c fixed reference system; let $\mathbf{y} = R_{sc}\,\mathbf{Y}$ be the same displacement in the inertial system, with R_{sc} a time dependent rotation. The accelerometer velocity in an inertial frame is

$$\dot{\mathbf{y}} = \dot{R}_{sc}\,R_{sc}^T\mathbf{y} + R_{sc}\,\dot{\mathbf{Y}} = \boldsymbol{\omega}\times\mathbf{y} + R_{sc}\,\dot{\mathbf{Y}}\ ,$$

with $\boldsymbol{\omega}$ the angular velocity of the s/c as a rigid body. The inertial acceleration is

$$\ddot{\mathbf{y}} = [\boldsymbol{\omega}\times(\boldsymbol{\omega}\times\mathbf{y}) + \dot{\boldsymbol{\omega}}\times\mathbf{y}] + 2\boldsymbol{\omega}\times R_{sc}\,\dot{\mathbf{Y}} + R_{sc}\,\ddot{\mathbf{Y}} = \mathbf{a}_{rot} + \mathbf{a}_Y\ , \tag{2.34}$$

where the part inside square brackets is the rotation acceleration $\mathbf{a}_{rot}$ of the accelerometer, $\mathbf{a}_Y$ is the acceleration due to a possible drift of the CoM in the s/c frame, due to either movable parts or fuel consumption. Both are applied by solid state forces on the accelerometer cage.

Moreover, the accelerometer sensitive element is accelerated by the gravity field $\nabla V(\mathbf{x}+\mathbf{y})$, while the cage is accelerated by the gravity field at the CoM: thus the accelerometer also measures a gravity gradient acceleration. This acceleration can be computed, neglecting $\mathcal{O}(|\mathbf{y}|^2)$ terms, from the matrix of second derivatives of the gravitational potential V:

$$\mathbf{a}_{gg}(\mathbf{y}) = \frac{\partial^2 V}{\partial\mathbf{x}^2}(\mathbf{x})\ \mathbf{y}\ .$$

Thus there are differential accelerations, functions of $\mathbf{y}$, while $\mathbf{a}_{ng}$ does not depend upon $\mathbf{y}$, and the accelerometer measures the combination

$$\mathbf{a}_{acc}(\mathbf{y}) = -\mathbf{a}_{ng} - \mathbf{a}_{rot}(\mathbf{y}) - \mathbf{a}_Y + \mathbf{a}_{gg}(\mathbf{y})\ , \tag{2.35}$$

where the minus sign applies to accelerations acting on the cage, plus when acting on the sensing element directly. The equation of motion of the CoM using the accelerometer is obtained by substituting (2.35) into (2.33):

$$\ddot{\mathbf{x}} = \nabla V(\mathbf{x}) - \mathbf{a}_{acc} - \mathbf{a}_{rot}(\mathbf{y}) - \mathbf{a}_Y + \mathbf{a}_{gg}(\mathbf{y})\ . \tag{2.36}$$

It is possible to compute the equation of motion for the accelerometer $\mathbf{x}+\mathbf{y}$ by adding equation (2.36) to (2.34), with cancellation of $\mathbf{a}_{rot}$, $\mathbf{a}_Y$:

$$\ddot{\mathbf{x}} + \ddot{\mathbf{y}} = \nabla V(\mathbf{x}) - \mathbf{a}_{acc} + \nabla\left(\nabla V\right)(\mathbf{x})\ \mathbf{y} = \nabla V(\mathbf{x}+\mathbf{y}) - \mathbf{a}_{acc}\ , \tag{2.37}$$

with the important result that, when using the data from the accelerometer as a term in the equation of motion, the equations of motion for the accelerometer are simpler than the ones for the CoM[2].

[2]This method was suggested by H.-R. Schulte of EADS-Astrium in 2007

The above presentation is quite simplified: care needs to be taken of three points. First, the tracking instruments are neither in $\mathbf{x}$ nor in $\mathbf{x}+\mathbf{y}$, but have some other reference point (e.g., the antenna phase center) displaced by a vector $\mathbf{Z}$ in s/c axes from the CoM. If the tracking data are s/c positions, they refer to $\mathbf{x}+\mathbf{z}$ (where $\mathbf{z}=R_{sc}\,\mathbf{Z}$) and have to be corrected by subtracting $\mathbf{z}-\mathbf{y}$; on the other hand, $\mathbf{Z}-\mathbf{Y}$ is better known than $\mathbf{Z}$, since the position of the CoM inside the s/c structure may depend upon the poorly known content of fuel in the tanks. If the tracking data are range and range-rate, corrections containing $\mathbf{z}-\mathbf{y}$ and $\dot{\mathbf{z}}-\dot{\mathbf{y}}$, respectively, have to be applied, and the requirements on the knowledge of $\mathbf{Z}-\mathbf{Y}$ and $\dot{\mathbf{Z}}-\dot{\mathbf{Y}}$ are very important.

Second, for a spring accelerometer, there are three separate sensitive points $\mathbf{Y}_i$, $i=1,2,3$, with mutual distances of several cm which cannot be ignored. The solution is to select a conventional reference point $\mathbf{Y}$ in the accelerometer structure, then correct the readings of the three channels for the displacements $R_{sc}\,(\mathbf{Y}_i-\mathbf{Y})$, with $\mathbf{Y}_i-\mathbf{Y}$ well known (and presumably constant).

Third, this discussion assumes that the rotation state, not just R_{sc} but also $\boldsymbol{\omega}$ and $\dot{\boldsymbol{\omega}}$, are well known. In reality there should be a contribution from the knowledge of these quantities in the error budget.

The other fundamental issue to consider is the so called *calibration* of the accelerometer. Since the accelerometer measures only differential accelerations, the zero of the measurement scale is a critical point. In other words, there are sources of error in the accelerometer measurements that inevitably shift the zero of the scale. Let's call them $\boldsymbol{\epsilon}$, so that $\mathbf{a}_{acc}\rightarrow\mathbf{a}_{acc}+\boldsymbol{\epsilon}$. In particular the thermic effects are very important, because the accelerometer is sensitive to the temperature and it acts also as a thermometer (see [Iafolla and Nozzoli 2001] and Section 2.6.2). This error is not included in the dynamical model and so it can be source of systematic error in the orbit determination fit.

In order to absorb the error $\boldsymbol{\epsilon}$, we must calibrate the accelerometer reading $\mathbf{a}_{acc}$ with an additional term $\mathbf{c}$, which is in principle a function of time and of a certain number of unknown parameters depending on how we try to model the error. As a first approximation we could consider $\mathbf{c}$ as constant for time scales of the order of 10^4 s (see [Milani et al. 2001]). With this approach $\mathbf{c}(t)$ is approximated as a discontinuous piecewise constant function.

A more refined approach consists in representing $\mathbf{c}(t)$ as a Hermite cubic spline. For the whole interval going from the central time of the arc $k-1$, say t_{k-1}, to the central time of the arc k, say t_k, (see Fig. 2.3 and Sec. 2.6.3) we have:

$$\mathbf{c}_{k-1,k}(t)=\boldsymbol{\alpha}_{k-1,k}+\boldsymbol{\beta}_{k-1,k}t+\boldsymbol{\gamma}_{k-1,k}t^2+\boldsymbol{\eta}_{k-1,k}t^3, \tag{2.38}$$

where the constants $\boldsymbol{\alpha}_{k-1,k}$, $\boldsymbol{\beta}_{k-1,k}$, $\boldsymbol{\gamma}_{k-1,k}$ and $\boldsymbol{\eta}_{k-1,k}$ are obtained by solving the linear

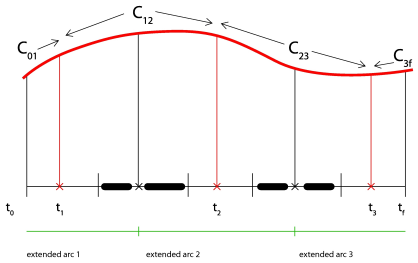

Figure 2.3: Spline sketched representation.

system of equations:

$$\begin{cases} \mathbf{c}_{k-1,k}(t_{k-1}) = \boldsymbol{\zeta}_{k-1}, \\ \dot{\mathbf{c}}_{k-1,k}(t_{k-1}) = \dot{\boldsymbol{\zeta}}_{k-1}, \\ \mathbf{c}_{k-1,k}(t_k) = \boldsymbol{\zeta}_k, \\ \dot{\mathbf{c}}_{k-1,k}(t_k) = \dot{\boldsymbol{\zeta}}_k, \end{cases} \tag{2.39}$$

where $\boldsymbol{\zeta}_k = \mathbf{c}_{k-1,k}(t_k) = \mathbf{c}_{k,k+1}(t_k)$ and $\dot{\boldsymbol{\zeta}}_k$ (the corresponding derivatives) are the quantities to be determined. For each extended arc k the solve for quantities are $\boldsymbol{\zeta}_k$, $\dot{\boldsymbol{\zeta}}_k$, plus the boundary conditions, 6 associated with the first observation time and 6 with the last one.

Eventually, we have

$$\mathbf{a}_{ng} = -(\mathbf{a}_{acc} + \mathbf{c}), \tag{2.40}$$

and the parameters to solve for become only the ones contained in the calibration $\mathbf{c}$.

In conclusion, the simulation of the accelerometer readings can be done by using the previous model for the non gravitational perturbations, along with a suitable noise and calibration model. At the correction stage, no modeling at all of the perturbations is necessary, the accelerometer readings are just added to the right hand side of the equations of motion by formula (2.40). Even if the non gravitational perturbations model is rough, the results of the simulation do not depend upon the accuracy of the model, but only upon the accuracy of the accelerometer measurements and of its calibration.

2.5.4 Maneuvers

Additional sources of perturbation on the orbit of the s/c around Mercury are the maneuvers performed on it. As a consequence of the torque on the satellite, and in particular the terms due to the high radiation pressure, the reaction wheels that counterbalance the external torque have to be periodically desaturated. This is done by desaturation (dump) maneuvers performed by the use of impulsive thrusters [Iafolla et al. 2011]. Such maneuvers could be modeled in different ways. The easiest one is by giving a total

$\Delta\,\mathbf{v}$, a time at which the maneuver starts, and a $\Delta\,h$ time duration of the maneuver. According to [Iafolla et al. 2011], a desaturation maneuver $\Delta\mathbf{v}$ is formed by 60 pulses of 9 seconds and takes place about every 12 hours.

Given the three components of $\Delta\mathbf{v}$ in the radial, transversal and out-of-plane directions $(\hat{\mathbf{r}}, \hat{\mathbf{t}}, \hat{\mathbf{w}})$, we model the corresponding accelerations in such a way that the integral over a given time span coincides with Δv_r, Δv_t and Δv_w respectively. In particular, we simulate a smooth signal consisting in a trapezoid composed by a degree 5 polynomial on the two sides plus a constant term on the minor base (Fig. 2.4). The components in the $(\hat{\mathbf{r}}, \hat{\mathbf{t}}, \hat{\mathbf{w}})$ system are given in Tab. 2.3. We notice that Δv_t is entirely due to thruster errors.

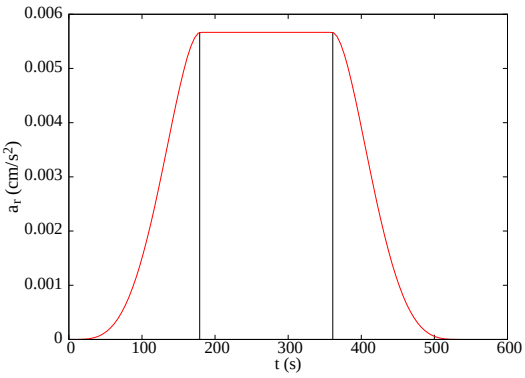

Figure 2.4: Trapezoid model implemented for the acceleration acting on the probe due to the desaturation maneuvers (radial component).

In each direction $(\hat{\mathbf{r}}, \hat{\mathbf{t}}, \hat{\mathbf{w}})$ we have

$$a^{man}_{r,t,w} = \begin{cases} b_4 t^4 + b_5 t^5 & \text{if } t \leq \Delta s, \\ b_4(\Delta h - t)^4 + b_5(\Delta h - t)^5 & \text{if } t \geq \Delta h - \Delta s, \\ b_4 \Delta s^4 + b_5 \Delta s^5 & \text{otherwise,} \end{cases} \tag{2.41}$$

where $\Delta h = 540$ s is the time interval where the maneuver extends, $\Delta s = 180$ s determines how fast the s/c reaches the acceleration peak and b_4 and b_5 depend on $\Delta v_{r,t,w}$, Δh and Δs.

Δv_r (cm/s)	Δv_t (cm/s)	Δv_w (cm/s)
1.7	0.2	4.2

Table 2.3: Components associated with each desaturation maneuver in the $(\hat{\mathbf{r}}, \hat{\mathbf{t}}, \hat{\mathbf{w}})$ reference system [Iafolla et al. 2011].

Notice that this model has a slightly different result with respect to that of an

instantaneous maneuver because over 9 minutes the s/c is subjected to other effects that sum up with $\mathbf{a}^{man}$.

If a maneuver occurs during a non-tracking session, to obtain an accurate determination of the s/c state vector at the beginning of the subsequent observed arc could become problematic. We just notice that, until the knowledge of the $\Delta\,\mathbf{v}$ will be provided by independent sources and with enough accuracy, it will be added to the list of solve for parameters. In this case, problems related to rank deficiencies in the determination of the maneuvers have to be considered.

We will assume as a general scenario to have at most one dump maneuver during tracking and at most one dump maneuver in the "dark" periods without tracking. We found that in principle we are able to estimate, by a least squares fit, the three components of each performed maneuver. The presence of orbital maneuvers is not considered at this stage, assuming not to perform orbit determination around them.

2.5.5 Relativistic corrections

The main relativistic correction in the Mercurycentric orbit is due to the need to use proper time, that is a **Mercury Dynamical Time (TDM)** affected by the gravitational potential at Mercury. See [Milani et al. 2010] and Appendix A.2.

2.6 Numerical simulation

In this Section we describe the main aspects of the numerical experiment. The main purpose is to test the feasibility of the determination of a certain number of physical parameters, in particular the ones related to the rotation of Mercury, from remote gravimetry.

2.6.1 Architecture of the *Orbit_14* software system

The numerical simulation of the Radio Science Experiment will be performed by an orbit determination and parameter estimation software developed by the Celestial Mechanics group of the University of Pisa, to which the author of this Thesis belongs. The software is called *Orbit_14*. In the following a general overview of the architecture of the software is given.

The software needs to include all the parameters which might affect the observables at the level of accuracy which corresponds to the quality of the measurements. In principle, all of them could be the object of determination in a global least squares fit to the observables. However, some of the parameters, do appear in the observables but have to be handled as *consider parameters*, not to be determined, after checking that their present uncertainty is such that their contribution to the uncertainty of the observable is negligible.

Simulator and corrector. The global structure of the program is outlined in Fig.2.5. The main programs belong to two categories: *data simulator* and *differential corrector*. The simulator generates simulated observables (range and range-rate, accelerometer readings) and preliminary orbital elements. The corrector solves for all the parameters which can be determined by a least squares fit (possibly constrained and decomposed in a multi-arc structure, see Sec. 2.6.3).

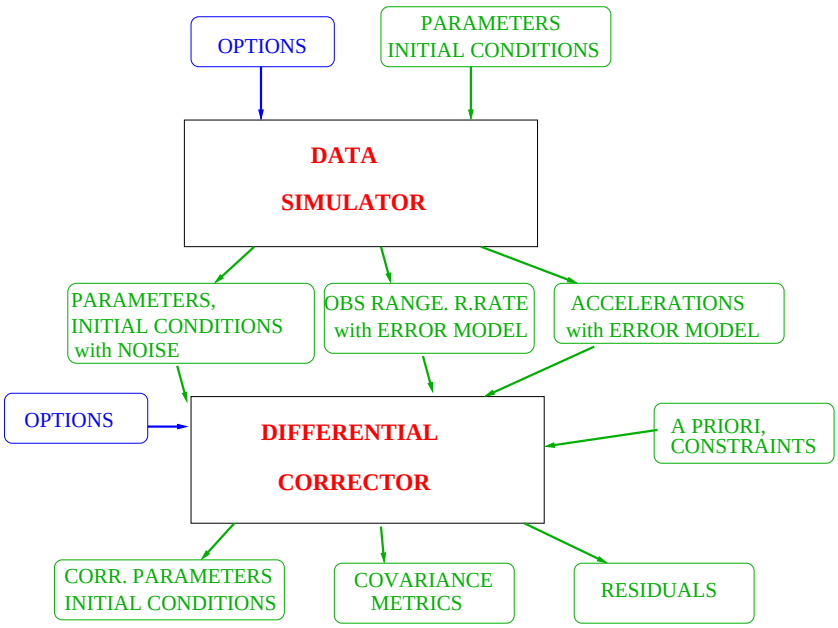

Figure 2.5: The block diagram of a simulator-corrector setup. The black rectangles indicate the main programs, the green rectangles with smoothed corners the data structures; in blue the option files for controls.

The program structure of the simulator is comparatively simple, with all the complexity in the dynamic, observation and error models. The corrector structure has to be designed in a very careful way (Fig.2.6). One of the goals of this software development was to be able to exploit parallel computing, especially for the most computationally expensive portion of the processing. The propagation of the planetocentric orbit contains most of the computational complexity, together with the light time computation. Thus we have parallelized the computation of the planetocentric dynamics and of the observables, with the relative partial derivatives.

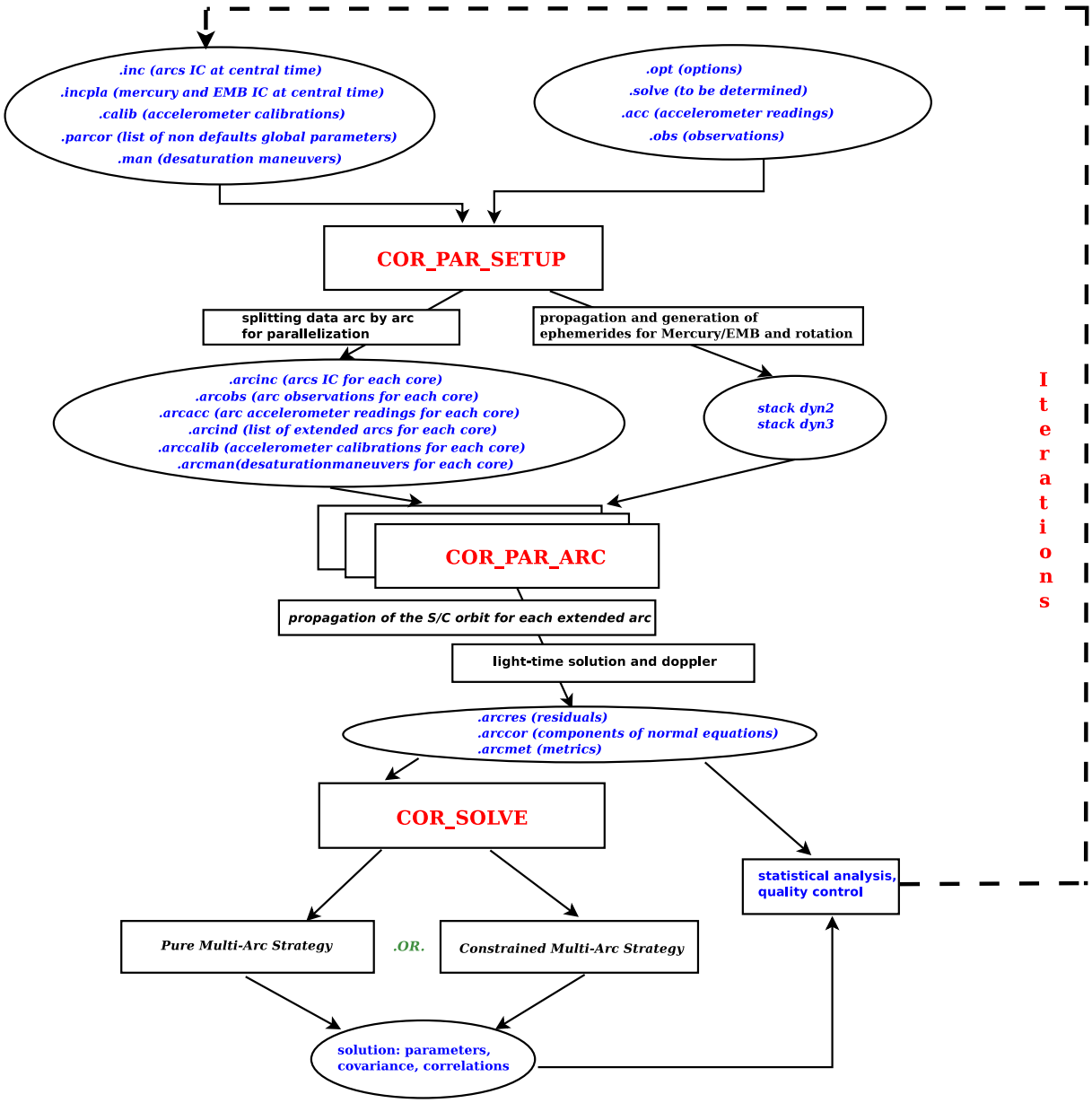

Figure 2.6: The block diagram of a differential corrector decomposed in three steps. The second one contains most of the computations and it is parallelized, by executing multiple copies of the same code, without any need for interprocess communication.

Propagators and multiple dynamics. Because of the multiple dynamics upon which the observables depend, the main programs need to have the propagated state available for each dynamics (for the list of dynamics, see Sec. 2.1.2). This is obtained in different ways, depending upon the dynamics:

- For the dynamics which have to be propagated by numerical integration, that is the Mercurycentric orbit of the s/c and the Solar System orbits of Mercury and the EMB, we call a propagator which solves the equation of motion, for the requested time interval. The states (time, position, velocity, acceleration, etc.) are stored in a memory stack, from which interpolation is possible with the required accuracy. Then, when the state is needed to compute the observables range/range-rate, the dynamics stacks are consulted and interpolated.

- In the case of the Earth rotational dynamics and of the planetary ephemerides, an interpolation table is already available from external sources (IERS, JPL).

2.6.2 Error models

The error models for the measurements are provided by the University of Rome "La Sapienza" (Prof. L. Iess and his group) for the range/range rate measurements and by the Italian Spring Accelerometer team (ISA, V. Iafolla and his group) for the accelerometer measurements.

The error models contain not only random errors, but systematic errors as well, the latter being more important to determine the true accuracy of the results (as opposed to the formal accuracy). Knowledge of the specific functional structure of the systematic errors would allow to remove them by calibration. Thus the information on the error models used in our simulation is only at the interface level.

Range and range rate error model

The reference values for the white noise, in terms of standard deviation, of the range and range-rate measurements are based on [Iess & Boscagli 2001]. At 1000 s integration time we have:

$$\sigma_r^{@1000s} = 10\,cm, \qquad \sigma_{rr}^{@1000s} = 3 \times 10^{-4}\,cm/s, \tag{2.42}$$

for a Ka-band tracking, and

$$\sigma_r^{@1000s} = 100\,cm, \qquad \sigma_{rr}^{@1000s} = 3 \times 10^{-3}\,cm/s, \tag{2.43}$$

for an X-band tracking. If the integration time Δt is less than 1000 s, the standard deviation associated to the measurements is simply obtained by

$$\sigma = \sigma^{@1000s}\sqrt{\frac{1000}{\Delta t}}.$$

From a comparison of the accuracies for the range and the range-rate it turns out that $\sigma_r^{@1000s}/\sigma_{rr}^{@1000s} = 3 \times 10^4$ s, which implies that the range-rate measurements are more

accurate than the range when we are observing phenomena with period shorter than 3×10^4 s. Since the s/c orbital period, and then the periods related to the gravity field perturbations, is of the order of 10^4 s, the gravimetry experiment is performed mainly with the range-rate tracking data. While it is the opposite in the Relativity Experiment context ([Milani et al. 2002]). For this reason, in this work we considered only the systematic errors in the range-rate measurements. The assumed error model contains also random errors with standard deviation $\sigma_{rr}^{@1000s} \cong 2.14 \times 10^{-4}\, cm/s$.

Accelerometer error model

For each arc, three sequences of errors are computed, to be interpreted as errors in the three sensing units (one dimensional accelerometers). However, the sensitive axis of the three accelerometers are aligned with the s/c axes, not with the axes of the ecliptic reference system used in the orbit propagation. Thus we have to use an assumption on the s/c attitude to convert the accelerometer errors to the propagation system.

We are assuming, for the purposes of this simulation, that the three sensitive axes are aligned in the radial, transversal, out of plane directions $\hat{\mathbf{r}}, \hat{\mathbf{t}}, \hat{\mathbf{w}}$ defined by the instantaneous Mercurycentric orbit plane. Thus the rotation to convert to the propagation system is a simple function of the s/c Mercurycentric position $\mathbf{r}$ and velocity $\mathbf{v}$.

After this coordinate transformation, the error vector is summed to the non gravitational perturbations as modeled by the simulator (see Sec. 2.5.3) and then written to one of the simulation output files. The corrector has access only to this corrupted data file, and cannot use the accelerometer noise.

However, we are assuming that the accelerometer data can be calibrated, by adding calibration parameters to the list of solve for parameters (see formula (2.40)).

The error includes both a standard deviation and systematic effects. However, the accelerometer measurements are not weighted, because they do not appear in the measurement equations. The effect of the accelerometer errors appears as a systematic one in the orbit propagation.

The main parameters which appear in the error model are: the amplitude δT_{ORB} of the temperature change (at the contact between the accelerometer and the holding structure) over one orbital period of the s/c and the amplitude δT_{SID} over one sidereal period of Mercury. These changes are modeled with trigonometric functions with periods 8 355 s and 3 800 000 s, respectively. Note that the main effect depending upon the orbit of Mercury is modeled with the frequency $2\,n$ (n is the mean motion of Mercury). The exact functional dependence of these effects upon time is something we must ignore at the correction stage. The values of the two parameters δT_{ORB}, δT_{SID} and the Fortran code actually computing the error model are provided by the ISA group. The values currently in use are, in degrees Kelvin:

$$\delta T_{ORB} = 0.1\,\mathrm{K}, \qquad \delta T_{SID} = 1.18\,\mathrm{K}.$$

The effect of this thermal input on the measurements depends upon the design of the accelerometer, and this requires a very accurate thermal calibration of the accelerometer in terms of active temperature control.

2.6.3 Pure and Correlated-Constrained Multi-arc method

In this subsection we define three different possible choices for the target function to process the data (Sec. 2.1.4), along with the definition of arc.

Arcs and extended arcs

We call an *observed arc* each set of range and range-rate tracking data, separated by several hours because of the visibility conditions of the s/c from the Earth (typically one set per day). Between two subsequent observed arcs we have a "dark" period without tracking. We define an *extended arc* an observed arc extended from half of the dark period before it to half of the dark period after it. In this way two subsequent extended arcs have one connection time (Fig.2.7). Finally, an *orbital arc* is a sequence of causally connected subsequent extended arcs. Two different orbital arcs are considered as belonging to different objects.

Let's call $(\mathbf{x}_0, \mathbf{v}_0)^k$ the initial condition of the $k-$th arc (assumed to be at the arc central time $t_{0\,k}$), which is the same of the $k-$th extended arc.

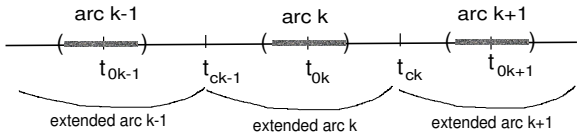

Figure 2.7: Temporal structure of the observed arcs and extended arcs.

Let n be the total number of observed arcs, n_k the number of observations of the arc k, and $m = \sum_k n_k$ the total number of observations. Let's suppose that all the residuals $\boldsymbol{\xi}^1, ..., \boldsymbol{\xi}^n$ are weighted with a $n_k \times n_k$ diagonal matrix $W_k = diag(1/\sigma_i^2)$ (see Sec. 2.6.2).

Ignoring the dark periods between the arcs we can define the target function

$$Q_\xi = \frac{1}{m} \sum_{k=1}^{n} \boldsymbol{\xi}^k \cdot W_k \boldsymbol{\xi}^k.$$

This target function defines the *pure multi-arc* method: in this case a set of independent initial conditions have to be determined for each arc (see [Milani & Gronchi 2010], Chap.15).

In the case of tracking an orbiter around Mercury, the problem is affected by the *Symmetries and rank deficiency in the orbit determination around another planet* (Sec. 2.4), thus a pure multi-arc method in which the observed arcs are not causally connected can be weak and unstable. However, exploiting the fact that each observed arc belongs to the same object (the s/c), we can add information by considering that at the connection

times between two subsequent extended arcs the orbits should coincide. Let's consider the discrepancy vectors

$$\mathbf{d}^{k,k+1} = \mathbf{y}_{k+1} - \mathbf{y}_k \,,$$

where $\mathbf{y}_k = \Phi_{t_{0\,k}}^{t_{c\,k}}[(\mathbf{x}_0, \mathbf{v}_0)^k]$, $\mathbf{y}_{k+1} = \Phi_{t_{0\,k+1}}^{t_{c\,k}}[(\mathbf{x}_0, \mathbf{v}_0)^{k+1}]$, $t_{0\,k}$, $t_{0\,k+1}$ are the central times of the $k-$th and the $(k+1)-$th arcs, $t_{c\,k}$ is the connection time between the two extended arcs, and Φ is the propagation of the state $(\mathbf{x}, \mathbf{v})$.

Once we have fixed the dynamical and observational model, the pure multi-arc method consists in fitting the residuals $\boldsymbol{\xi}^1, ..., \boldsymbol{\xi}^n$ by least squares. If we also consider that all the observed arcs actually belongs to the same object, we can state the following constraints:

$$\mathbf{d}^{k,k+1} = 0 \qquad \forall k = 1, .., n.$$

Each constraint can be incorporated as an additional quadratic form in the target function to minimize in the least square fit. Let's generically define this term by

$$Q_d = \frac{1}{6(n-1)} \sum_{k=1}^{n-1} \mathbf{d}^{k,k+1} \cdot C_{k,k+1} \mathbf{d}^{k,k+1},$$

where the 6×6 matrices $C_{k,k+1}$ are the weights for the constraints. The total target function Q taking into account both residuals and constraints will be a linear combination of Q_ξ and Q_d. We consider two different approaches to define the weights $C_{k,k+1}$ and the target function Q. The first approach exploits the linear orbit identification theory (see [Milani & Gronchi 2010] Chap.7), and we call it *internal correlated-constrained multi-arc*, while the second approach is based on the a priori observation theory (see [Milani & Gronchi 2010] Chap.6), and we call it *a priori correlated-constrained multi-arc*.

It is worth noticing that with this approach the additional information in Q_d does not derive from any arbitrary consideration on the dynamics or on the observational model, but only from the fact that we know that we are always observing the same object.

Internal correlated-constrained multi-arc

In order to define the weighting matrices of the discrepancies $\mathbf{d}^{k,k+1}$ we will follow the linear orbit identification theory described in [Milani & Gronchi 2010] Chap.7. First, we need to associate a covariance (or normal) matrix to each initial condition $(\mathbf{x}_0, \mathbf{v}_0)^k$. Since at the beginning of the experiment we don't have any orbit determination yet, the easiest way to do this is the following:

- Using the residuals of a single observed arc $\boldsymbol{\xi}^k$, we compute the 6×6 normal matrix

$$C_k = B_k^T W_k B_k \,, \qquad B_k = \frac{\partial \boldsymbol{\xi}^k}{\partial (\mathbf{x}_0, \mathbf{v}_0)^k},$$

relative to the initial conditions $(\mathbf{x}_0, \mathbf{v}_0)^k$ at times $t_{0\,k}$, $\forall k = 1, .., n$. Its associated covariance matrix (notice that in this case it is a conditional covariance matrix) is $\Gamma_k = C_k^{-1}$.

A more sophisticated way to do this is to try a pure multi-arc orbit determination and then associate to each $k-$th arc's initial condition its marginal covariance matrix Γ_k. After that we can propagate C_k and Γ_k at times $t_{c\,k-1}$ and $t_{c\,k}$ using the state transition matrix. Let's use the same notation for the propagated matrices. Since the covariance is linear, we associate to the discrepancy $\mathbf{d}^{k,k+1}$ the covariance $\Gamma_{k,k+1} = \Gamma_k + \Gamma_{k+1}$, then the weight matrix for the corresponding constraint $\mathbf{d}^{k,k+1} = 0$ is

$$C_{k,k+1} = \Gamma_{k,k+1}^{-1} = C_{k+1}(C_k + C_{k+1})^{-1}C_k = C_k(C_k + C_{k+1})^{-1}C_{k+1}. \tag{2.44}$$

The quantity $\sum_{k=1}^{n-1} \mathbf{d}^{k,k+1} \cdot C_{k,k+1}\mathbf{d}^{k,k+1}$ represents the minimum identification penalty for each couple of subsequent arcs. Here in the following are summarized the main points of this problem:

- The identification of two subsequent arcs at the connection point $t_{c\,k}$ consists in minimizing the target function

$$(n_k + n_{k+1})\Delta Q(\mathbf{y}) = \boldsymbol{\xi}^k \cdot W_k\boldsymbol{\xi}^k + \boldsymbol{\xi}^{k+1} \cdot W_{k+1}\boldsymbol{\xi}^{k+1} =$$

$$= (\mathbf{y} - \mathbf{y}_k) \cdot C_k(\mathbf{y} - \mathbf{y}_k) + (\mathbf{y} - \mathbf{y}_{k+1}) \cdot C_{k+1}(\mathbf{y} - \mathbf{y}_{k+1}) + \dots$$

- It is possible to approximate the minimum value of the function $(n_k + n_{k+1})\Delta Q(\mathbf{y})$ by the "identification penalty"

$$min[(n_k + n_{k+1})\Delta Q(\mathbf{y})] \cong (\mathbf{y}_{k+1} - \mathbf{y}_k) \cdot C(\mathbf{y}_{k+1} - \mathbf{y}_k)$$

  where

$$C = C_k - C_k\Gamma_0 C_k = C_{k+1} - C_{k+1}\Gamma_0 C_{k+1}\,,$$
$$\Gamma_0 = C_0^{-1} = (C_k + C_{k+1})^{-1}\,.$$

Notice that

$$C = C_k - C_k\Gamma_0 C_k = C_{k+1} - C_{k+1}\Gamma_0 C_{k+1} = C_k(C_k + C_{k+1})^{-1}C_{k+1} = C_{k,k+1}\,.$$

Then the total Target Function can be written in the form:

$$Q = \frac{1}{m}\left(\sum_{k=1}^{n} \boldsymbol{\xi}^k \cdot W_k\boldsymbol{\xi}^k + \sum_{k=1}^{n-1} \mathbf{d}^{k,k+1} \cdot C_{k,k+1}\mathbf{d}^{k,k+1}\right). \tag{2.45}$$

In general the number of constraints $\mathbf{d}^{k,k+1}$ could be less than $n-1$ when we have more than one orbital arc.

A priori correlated-constrained multi-arc

This approach is based on the a priori observation theory (see [Milani & Gronchi 2010] Chap.6), and it consists in considering the constraints $\mathbf{d}^{k,k+1} = 0$ as a priori observations of the s/c, associating to each constraint an a priori uncertainty $\Gamma_{k,k+1}$. For the sake of simplicity we adopt an isotropic uncertainty for position and velocity, i.e. $\Gamma_{k,k+1}$ is a diagonal matrix:

$$\Gamma_{k,k+1} = diag(\sigma_p^2, \sigma_p^2, \sigma_p^2, \sigma_v^2, \sigma_v^2, \sigma_v^2).$$

Moreover, keeping the ratio σ_p/σ_v to a fixed value given by the averaged ratio between the s/c position and velocity $\sim 10^3$ s, we can write the uncertainty as

$$\Gamma_{k,k+1} = \mu \; diag(1, 1, 1, 10^{-6}, 10^{-6}, 10^{-6}),$$

and the weight matrix for the discrepancy becomes

$$C_{k,k+1} = \frac{1}{\mu} \; diag(1, 1, 1, 10^{6}, 10^{6}, 10^{6}).$$

In this way we can modify the value of μ in order to have more smoothness at the connection times. The choice of μ can be made both once for all or it can be modified at every iteration of the differential correction process. For example, if σj_p and σj_v are the standard deviations of the discrepancies in position and in velocity, we can use the following rule for the choice of μ at a certain iteration:

$$\mu = max\left(\frac{\sigma j_p^2}{\Delta\mu^2}, \frac{\sigma j_v^2 \times 10^6}{\Delta\mu^2}, \mu_{min}\right),$$

where μ_{min} is the minimum value allowed for μ and $\Delta\mu$ is the rate of decrease of the standard deviations of the discrepancies at each iteration step. In this case

$$Q = \frac{1}{m + 6(n-1)} \left(\sum_{k=1}^{n} \boldsymbol{\xi}^k \cdot W_k \boldsymbol{\xi}^k + \sum_{k=1}^{n-1} \mathbf{d}^{k,k+1} \cdot C_{k,k+1} \mathbf{d}^{k,k+1} \right). \tag{2.46}$$

Finally, if X is the vector of solve for parameters, the differential corrections procedure to compute the minimum of the target function can be written as (see Section 2.1.4)

$$X_{i+1} = X_i - C^{-1} \, B^T \, W \, (\boldsymbol{\xi}^1, \mathbf{d}^{1,2}, \boldsymbol{\xi}^2, ..., \mathbf{d}^{n-1,n}, \boldsymbol{\xi}^n)^T,$$

where

$$B = \frac{\partial(\boldsymbol{\xi}^1, \mathbf{d}^{1,2}, \boldsymbol{\xi}^2, ..., \mathbf{d}^{n-1,n}, \boldsymbol{\xi}^n)}{\partial X},$$

is the design matrix, and the Normal matrix is

$$C = B^T W B, \qquad W = diag(W_k, C_{k,k+1}).$$

Parameters classification

In order to obtain a convenient structure for the Design and the Normal matrix, it is useful to classify the solve for parameters in different categories. A preliminary useful classification is the following:

- **Global parameters (g)**: parameters which affect the dynamic equations of every (extended) arc. Examples: C_{20}, C_{22}, etc...
- **Local parameters (l^k)**: parameters which affect only the dynamic equations of a single observed (and extended) arc k. Examples: the arc initial conditions $(\mathbf{x}_0, \mathbf{v}_0)^k$, a dump maneuver $\Delta\mathbf{v}$ which takes place during tracking.
- **Local external parameters ($le^{k,k+1}$)**: parameters which affect only the dynamic equations in the dark period between two subsequent observed arcs k and $k+1$. Examples: a dump maneuver $\Delta\mathbf{v}$ which takes place out of the observed arcs.

Notice that this classification does not exclude other kinds of parameters, e.g. particular attention is needed for the classification of the accelerometer calibrations parameters.

By this classification we have for each $k-$th observed arc:

$$\boldsymbol{\xi}^k = \boldsymbol{\xi}^k(g, l^k), \qquad \mathbf{d}^{k,k+1} = \mathbf{d}^{k,k+1}(g, l^k, le^{k,k+1}, l^{k+1}).$$

It is evident from these formulas that with the constrained multi-arc method it is possible to determine also the maneuvers taking place out of tracking, while it would have been impossible with a pure multi-arc method.

We assume as solve for parameters order the following:

$$X = (g, l^1, le^{1,2}, l^2, le^{2,3}, ..., l^{n-1}, le^{n-1,n}, l^n).$$

Design matrix

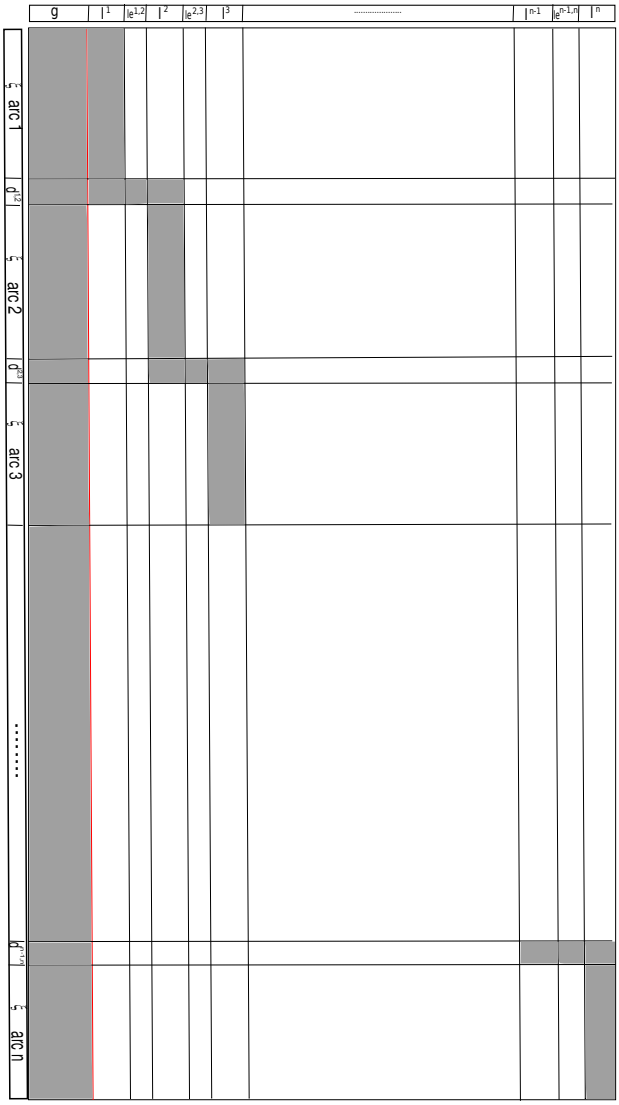

Figure 2.8: General structure of the Design matrix for the MORE experiment, the blank blocks in the matrix are zeros.

Weight matrix

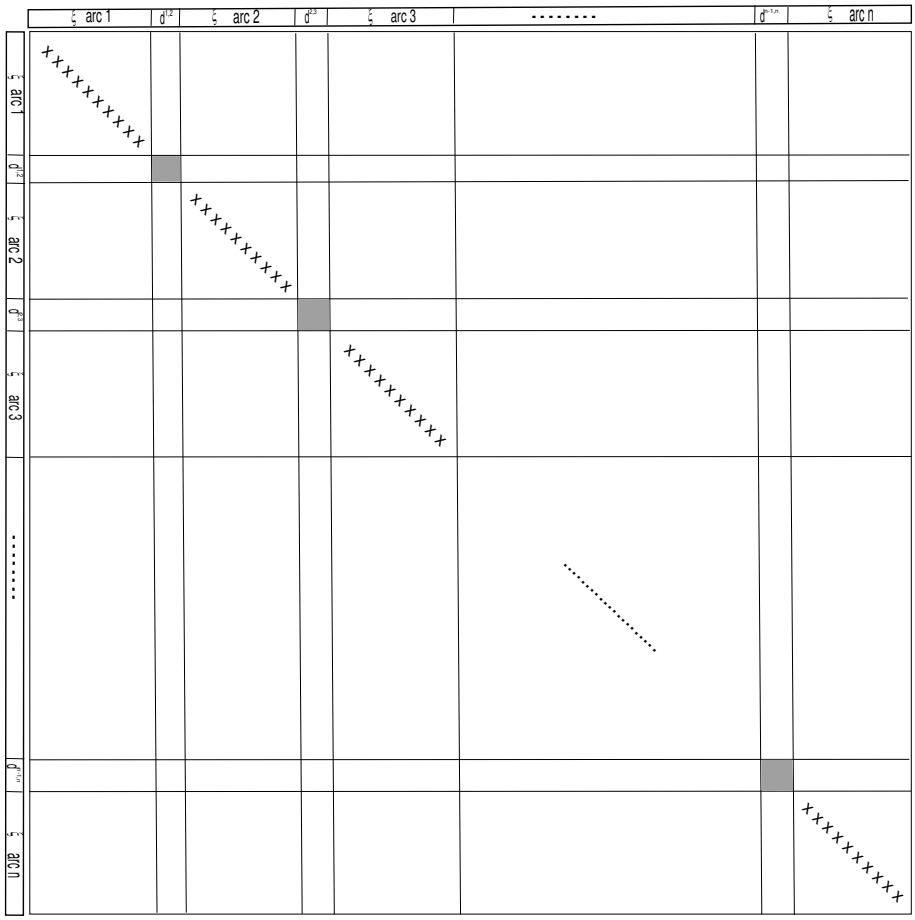

Figure 2.9: General structure of the Weight matrix for the MORE experiment, the blank blocks in the matrix are zeros.

Normal matrix

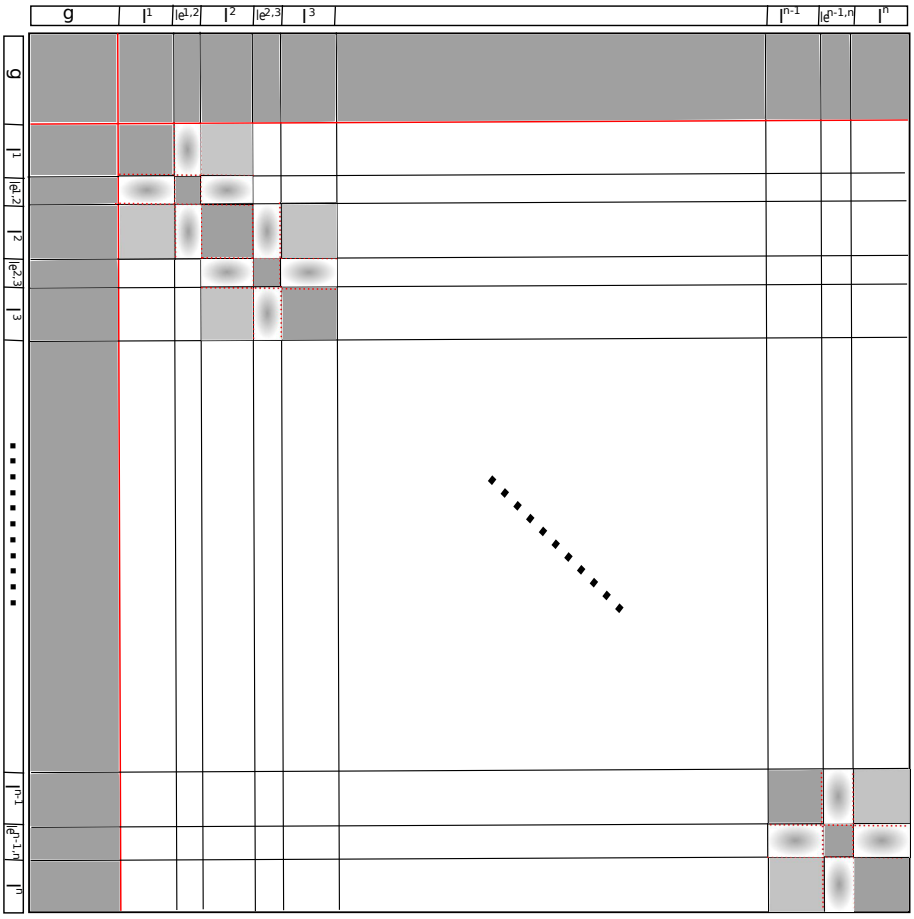

Figure 2.10: General structure of the Normal matrix for the MORE experiment, the blank blocks in the matrix are zeros.

2.7 Results and statistical analysis

2.7.1 Assumptions

1. Two ground stations are available for tracking, one in X-band (in Madrid, Spain) and one in Ka-band (in Goldstone, CA). Range measurements are taken every 120 s while range-rate measurements are every 30 s.

2. Range-rate is measured with top accuracy. Random and systematic error in range-rate for Ka-band tracking, random only for X-band tracking are added to the simulated observables, as described by the error model in Sec. 2.6.2.

3. Range is measured with top accuracy. Only random error is added to the simulated observables, as described by the error model in Sec. 2.6.2.

4. The observation time span covers 88 arcs (about one Mercury orbital period).

5. Gravity field spherical harmonics up to degree $l_{max} = 25$, plus tidal effects represented by the Love number k_2. The nominal values for the normalized gravity field coefficients, with respect to the body-fixed principal of inertia reference system, used in the simulator, are:

   - degree 2: $C_{20} = -2.7 \times 10^{-5}$, $C_{22} = 1.6 \times 10^{-5}$ (from [Anderson et al. 1987]), $C_{21} = S_{21} = S_{22} = 0$;
   - degree >2: scaled from the ones of the Earth by a factor 3;
   - $k_2 = 0.25$.

6. The rotation model assumed is the semi-empirical one, described in Sec. 2.5.1. The nominal values for the rotation parameters assumed in the simulator are:

$$\begin{aligned} &\delta_1 = 4.3\,\text{arcmin}, \quad \delta_2 = 0, \\ &\epsilon_1 = 35\,\text{arcsec}, \quad \epsilon_2 = 40\,\text{arcsec}. \end{aligned} \tag{2.47}$$

7. Solar radiation pressure and indirect Mercury albedo radiation pressure are present in the simulation of the observables.

8. The accelerometer is always on, and is operated in such a way that its error model is as given in 2.6.2; when there is no tracking, the data are stored and retransmitted later. The calibration is modeled using a cubic spline.

9. Two dump maneuvers are performed for each arc, one during tracking and one in the dark period between two subsequent arcs, as described in 2.5.4. Notice that they are assumed not included in accelerometer reading.

10. The strategy used to process the simulated observations is the a priori correlated-constrained multi-arc method, as defined in Sec. 2.6.3, with $\mu = 1$ cm.

11. The s/c initial conditions with respect to the reference system $(\mathbf{X}_1, \mathbf{Y}_1, \mathbf{Z}_1)$ are the following (in classic Keplerian elements, values from [Garcia et al. 2009]) at epoch *September 1 2020*:

$$\begin{aligned} &a = 3.394 \times 10^3\,\mathrm{km}; \quad e = 0.16; \quad i = 90^\circ; \\ &\Omega = 67.7^\circ; \quad \omega = 16^\circ; \quad \nu_0 = 0. \end{aligned} \tag{2.48}$$

The correction step is defined by the list of solve-for parameters:

- **Global dynamical**: Coefficients of the (normalized) spherical harmonics of the gravity field of Mercury, static part; of degrees from 2 to 25, all possible orders.
- **Global dynamical**: Dynamical Love number k_2.
- **Global dynamical**: Rotation parameters δ_1, δ_2, ϵ_1, ϵ_2.
- **Global dynamical**: 6 accelerometer calibration constants $(\boldsymbol{\zeta}_k, \dot{\boldsymbol{\zeta}}_k)$, for each arc, plus 6+6 boundary conditions.
- **Local dynamical**: 6 initial conditions, Mercurycentric position and velocity in the Ecliptic J2000 inertial frame, for each arc.
- **Local dynamical**: 3 dump maneuver components, taking place during tracking, for each observed arc.
- **Local external dynamical**: 3 dump maneuver components, taking place in the dark period between each pair of subsequent observed arcs.

We are assuming that an arc is terminated when either the station to s/c (up-leg) radio wave path or the s/c to station (down-leg) path have an elevation at the station with respect to the station horizon below a critical value El_0; the default used is $El_0 = 20^\circ$. Note that both the down-leg and the up-leg condition has to be verified, since the two are separated by about 1/4 of an hour. The arc is also terminated if the angle between the spacecraft and the Sun, as seen from the ground station, is less than a critical value ψ_0. As default we use $\psi_0 = 2^\circ$. In practice we terminate the arc whenever there is an interruption of the range-rate observation longer than $t_{gap} = 1$ hour: this interval is longer than the longest possible interruption due to occultation of the s/c by Mercury (and by the s/c itself). Thus the observed arc can contain shorter gaps due to occultations. We also discard arcs with total duration below a minimum (2 hours), because the initial conditions would be too poorly determined; this indeed occur for some arcs near the superior conjunctions. An example of visibility conditions is shown in Fig. 2.11)

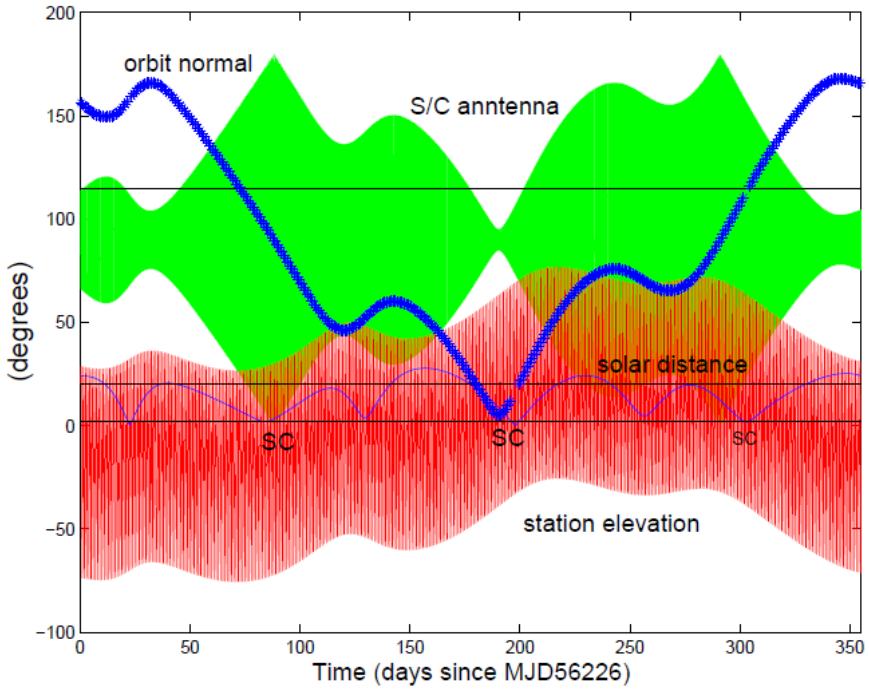

Figure 2.11: Example of visibility conditions for the s/c over an year (time is in days). The plot shows four lines. (1) The angle between the normal to the s/c Mercurycentric orbit and the direction of the Earth. (2) The angle between the mast of the high gain antenna and the direction of the Earth; it is assumed that communication with the ground station is impossible if this angle is more than 115° (this occultation by the spacecraft itself is slightly longer than the occultation by Mercury); this results in interruptions of the observing sessions by up to $\simeq$ 1 hour during one Mercurycentric orbit (2.3 hours). These occultations occur when the angle (1) is in the neighborhood of 90°. (3) The elevation of Mercury (and the spacecraft) above the horizon at the observing station; it is assumed that observations are impossible (or at least inaccurate) when the elevation is below 20°. (4) The angle between Mercury (and the spacecraft) and the Sun as seen from Earth; it is assumed that the observations are not possible/not used when this angle is less than 2°.

2.7.2 Results

All the results presented in the following are intended to be at convergence of the differential correction process (Sec. 2.6.3). The analysis is performed both on formal statistics (standard deviations and correlations), as given from the formal covariance matrix $\Gamma = C^{-1}$, and on the actual (true) errors between the parameters value at convergence and the value used in the simulation of the observables.

Notice that an error of a few times the formal uncertainty is introduced in the first guess in order to test the convergence power. A detailed analysis on the convergence basin of the differential corrections is beyond the purpose of this Thesis, even though it is a crucial point in a real experiment context where nobody knows the exact value of the solve for parameters.

Gravity field determination. The main goal of the gravimetry experiment is to solve for the harmonic coefficients of the gravity field of Mercury. The results can be effectively summarized by Fig.2.12, showing the gravity field signal as simulated (and the Kaula's rule approximation) together with the formal error and the actual error including possible systematic effects. The error is given as R.M.S. value for all the normalized harmonic coefficients of a given degree.

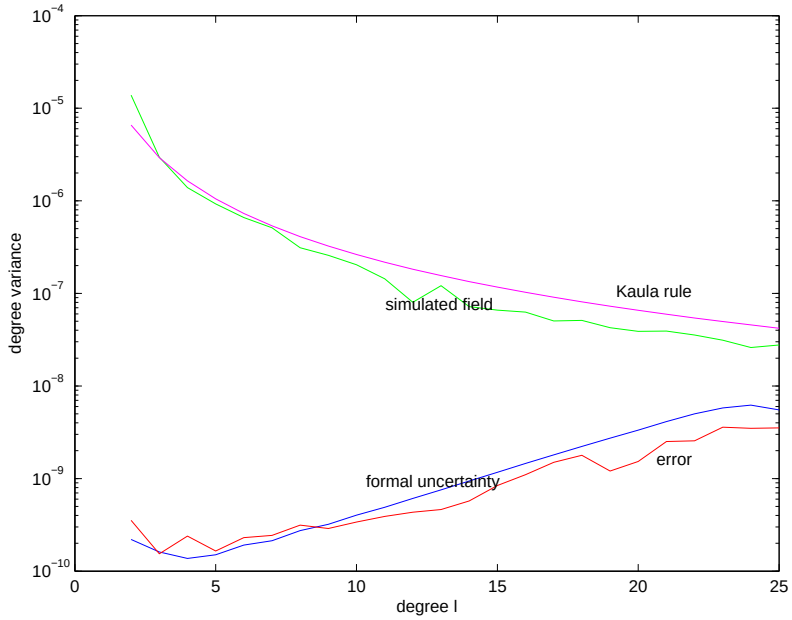

Figure 2.12: Signal and error for the numerical simulation, expressed for each degree ℓ in terms of the RMS value for the $2\ell+1$ normalized harmonic coefficients with different order m.

With all the assumptions we have made, the signal to error is above 1 still at degree 25. Moreover, the decrease in the error is roughly by a factor 10 over the entire spectrum of degrees up to 25.

The results for the determination of the Love number k_2, describing the non-static gravity field of Mercury (equation (2.32)), are shown in Tab. 2.4. A formal relative

	True value	Formal Sigma	True Error
k_2	0.25	9.0×10^{-4}	4.5×10^{-5}

Table 2.4: Results for the determination of the Love number k_2.

accuracy of ~ 0.36 %, much better than 1 %, over only 88 days of observations is a significantly good result.

Initial conditions determination. We describe here the main results on the determination of the initial conditions for each arc.

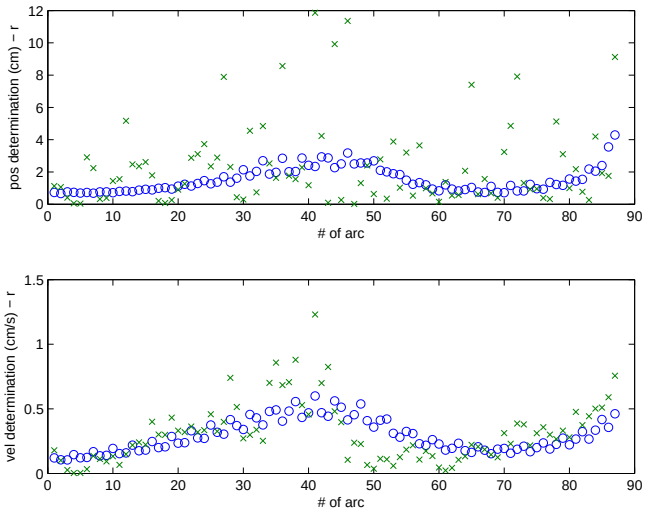

Figure 2.13: Formal error (circles) compared to true errors (crosses) for the initial conditions in position (top) and velocity (bottom) - radial component.

The quality of the initial conditions determination for each arc are shown in Figures 2.13, 2.14, 2.15 for the radial, weak (formula (2.26)) and Earth-Mercury component, respectively. This can be measured by comparing the length of the actual position error vector (difference between the "true" value used in the simulation and the solution determined at the correction stage) with the longest axis of the confidence ellipsoid (corresponding to 1 σ, as defined by the formal covariance matrix). The arcs are

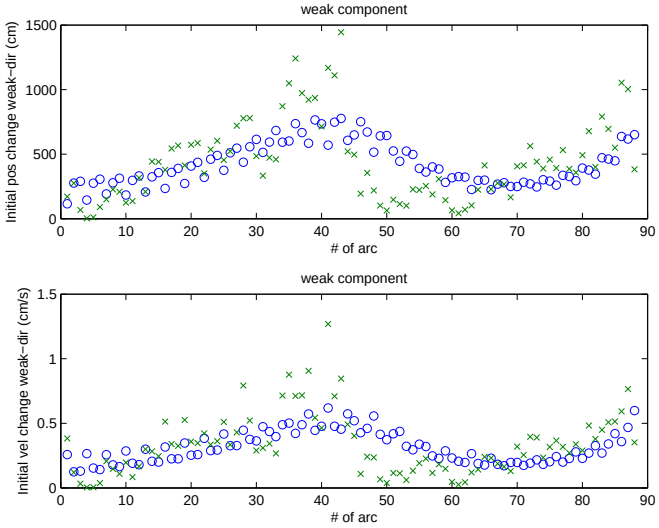

Figure 2.14: Formal error (circles) compared to true errors (crosses) for the initial conditions in position (top) and velocity (bottom) - in the weak direction component (formula (2.26)).

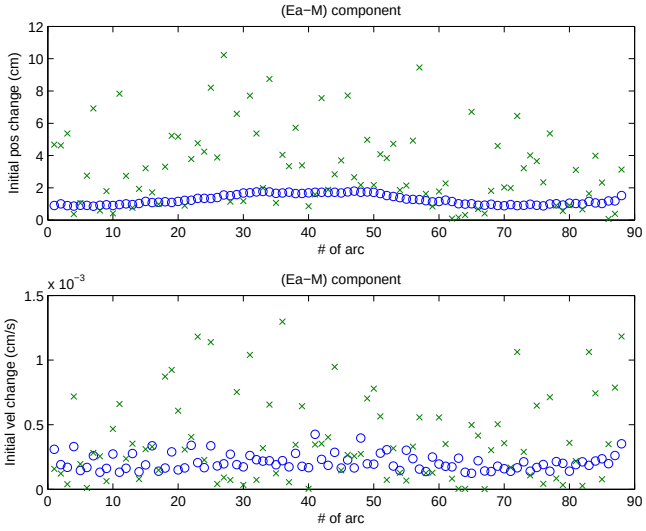

Figure 2.15: Formal error (circles) compared to true errors (crosses) for the initial conditions in position (top) and velocity (bottom) - Earth-Mercury component.

essentially one per day. The tentative conclusion from these Figures is that the systematic dynamic model errors resulting from the lack/inaccuracy of the accelerometer calibration are amplified by the weakness of the orbit determination, as discussed in [Bonanno & Milani 2002]. This effect is not uniform over the simulation time span and depends upon many factors, including the duration of the observing session (a seasonal effect) and the angle between the orbit plane and the direction of the Earth (see details in Fig. 2.16. Anyway, the initial conditions are determined with an accuracy of several tens of centimeters to a few meters (both in "true error" and in formal uncertainty).

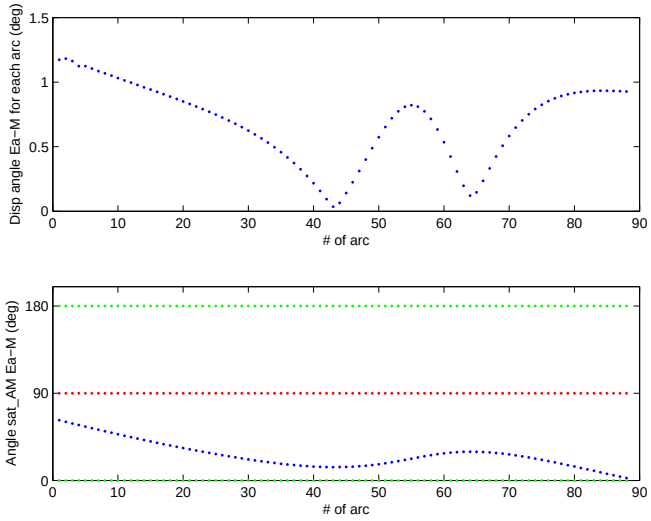

Figure 2.16: Top: Displacement angle of the Earth-Mercury direction over each arc. Bottom: angle between the satellite orbital angular momentum and the Earth-Mercury direction.

Accelerometer calibration. The most critical issue about the accelerometer calibration is that the accelerometer measures only relative values of the non gravitational perturbations, then we need to derive the average of these values from the tracking data. If this determination is inaccurate, this directly impacts the accuracy of the orbit and propagates, through the correlations present in the solution for all parameters, to the gravity field solution. In our simulation, thanks to the assumed moderate accelerometer error and the efficiency of the spline calibration model, this problem is not too severe, as shown in Figures 2.17, 2.18, 2.19. The average of the transversal component is determined to an accuracy of few times 10^{-8} cm/s^2, while the radial and out-of-plane components are determined less accurately ($\sim 10^{-6}$ cm/s^2). The transversal component is quite well represented, while the other two are not. What turns out from this result is that the transversal calibration is certainly useful in absorbing the error, but the one in the other components should be improved, e.g. by imposing an a priori constraint on their oscillations amplitude.

It is important to underline that the numerical experiments have shown the accelerometer calibration to be crucial in affecting the quality of the orbit determination and parameter estimation. From one hand, the current accelerometer error model, if not calibrated, is a source of very large systematic errors in the solution, which makes the results based on formal statistics unreliable. On the other hand, the calibration we have introduced consists in determining 6 quantities for each observed arc, which means $\mathcal{O}(10^3)$ solve for parameters, with their high mutual correlations. This turns out to be effective in reducing significantly the systematic errors, but it unavoidably makes worse the formal accuracies of the orbit determination with respect to the case without accelerometer error.

It is clear that possible improvements both in the reduction of the accelerometer error and in its calibration model would be desirable for a better success of the Radio Science Experiment.

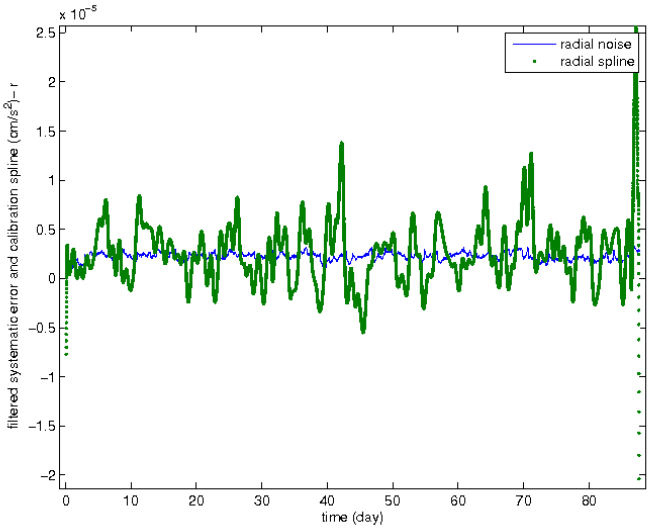

Figure 2.17: Accelerometer noise (blue curve) compared to spline calibration (green curve), radial component.

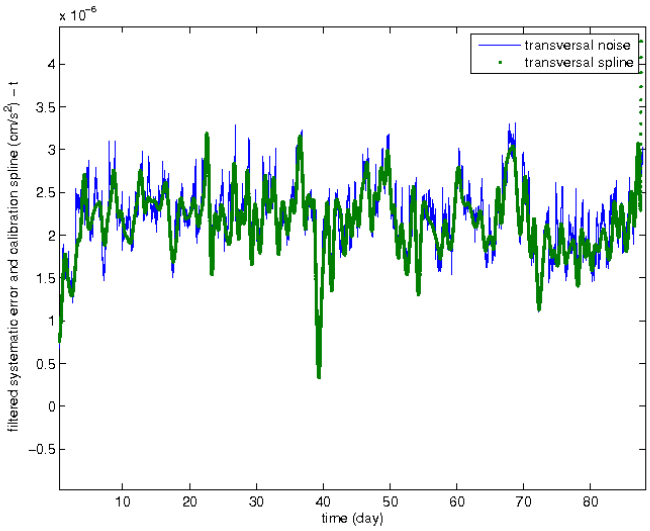

Figure 2.18: Accelerometer noise (blue curve) compared to spline calibration (green curve), transversal component.

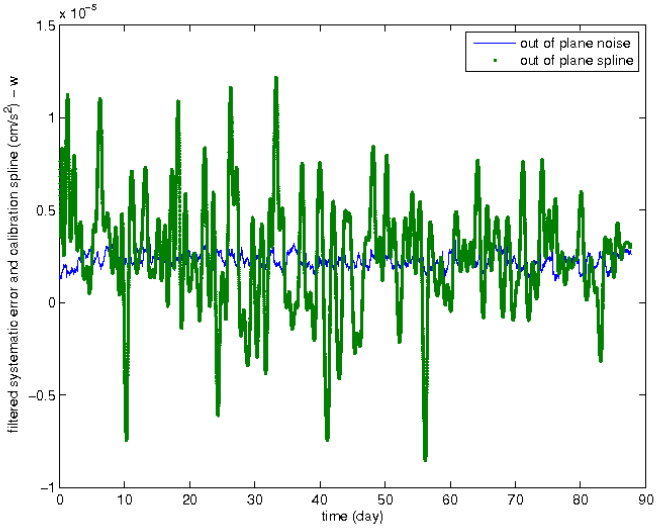

Figure 2.19: Accelerometer noise (blue curve) compared to spline calibration (green curve), out of plane component.

Desaturation maneuvers. The results for the determination of the desaturation maneuvers (taking place during tracking and in the dark) are described in Figures 2.20, 2.21, 2.22. As we can see, these quantities are the most affected by systematic errors coming from the unavoidable lack/inaccuracy of the accelerometer calibration model. The true error dominates the formal uncertainty up to an order of magnitude in several cases. However, even in the worst cases, the error does not exceed the order of $\sim 10^{-2}$ cm/s and a relative accuracy of the order of few percents of the nominal value.

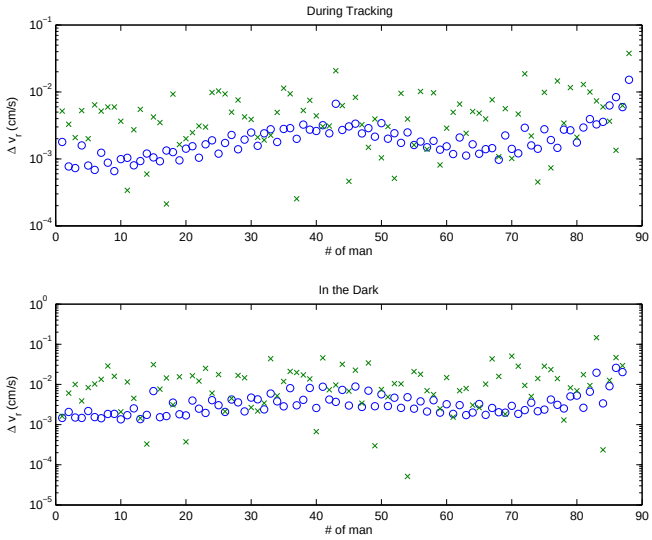

Figure 2.20: Formal error (circles) compared to true errors (crosses) for the dump maneuver Δv radial component.

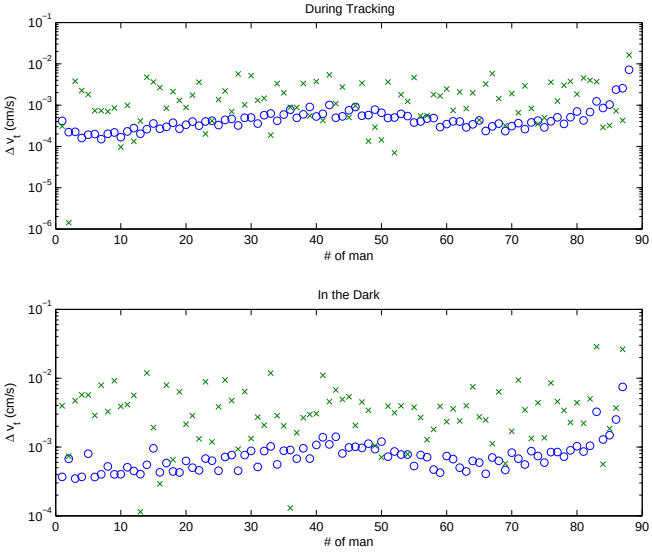

Figure 2.21: Formal error (circles) compared to true errors (crosses) for the dump maneuver Δv transversal component.

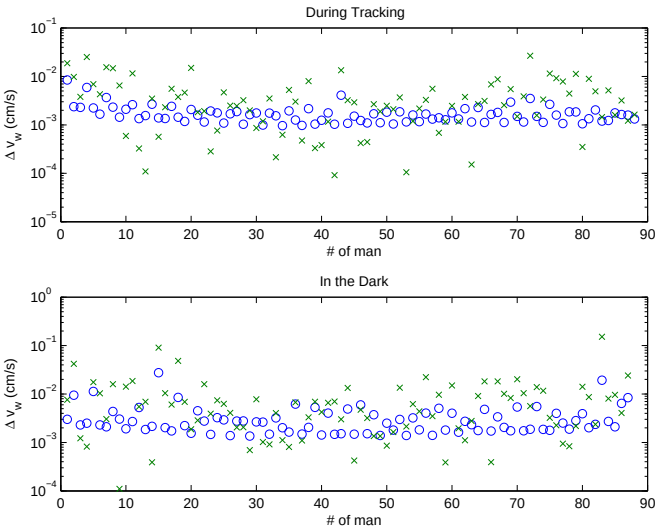

Figure 2.22: Formal error (circles) compared to true errors (crosses) for the dump maneuver Δv out of plane component.

Rotation from gravimetry. The results for the determination of the rotation state of Mercury, in terms of the semi-empirical rotation model defined in Sec. 2.5.1, are gathered in Tab. 2.5. These results show a very good accuracy in the determination of both the direction of the spin axis and the amplitude of the libration in longitude. The formal relative accuracies for the obliquity δ_1 and the libration in longitude amplitude ϵ_1 are

$$\frac{\Delta\delta_1}{\delta_1} \cong 0.07\ \%\ , \qquad \frac{\Delta\epsilon_1}{\epsilon_1} \cong 2.7\ \%\ ,$$

giving the same relative accuracies for the quantities C/MR^2 and $C_m/(B-A)$ respectively (from the approximated formulas (1.1) and (1.5)).

	True value	Formal Sigma	True Error
δ_1	4.2 am	0.17 as	-0.02 as
δ_2	0 am	0.32 as	-0.01 as
ϵ_1	35 as	0.89 as	-2.14 as
ϵ_2	40 as	12.83 as	$+0.13$ as

Table 2.5: Results for the determination of the rotation state of Mercury from gravimetry. The results for the angles δ_1, δ_2, ϵ_1, ϵ_2 are given in arc minutes (am) and arc seconds (as), semi-empirical model 2.5.1.

The Peale's experiment, as introduced in Sec. 1.1.2, needs also a good determination of the gravity field degree 2 spherical harmonics, and this is expressed by Fig. 2.12. The details of the five degree 2 coefficients are presented in Tab. 2.6.

	True value	Formal Sigma	True Error
C_{20}	-2.7×10^{-5}	1.2×10^{-10}	$+2.5 \times 10^{-11}$
S_{21}	0	8.2×10^{-11}	-1.5×10^{-10}
C_{21}	0	7.8×10^{-11}	-1.2×10^{-10}
S_{22}	0	3.9×10^{-10}	-4.0×10^{-10}
C_{22}	1.6×10^{-5}	2.5×10^{-10}	-6.5×10^{-10}

Table 2.6: Results for the determination of the gravity field degree 2 spherical harmonics.

The relative accuracy in the determination of the ratio C_m/C from formula (1.2) is then the following:

$$\frac{\Delta(C_m/C)}{C_m/C} \cong 2.7\ \%,$$

which is better than the required accuracy of 10 % proposed in [Milani et al. 2001].

These accuracies appear to be competitive with respect to the ones expected from the rotation experiment performed with the on-board camera. This result should not be interpreted as a replacement of the camera experiment: the fact that the results

are comparable at least in terms of order of magnitude allows us to cross check the two independent experiments to confirm their correctness. The presence of any form of inconsistency between them can be exploited to seek for sources of systematic errors.

Moreover, there could be also room for improvement for the experiment with the camera independently from the gravimetry experiment and the mix of the two techniques must give better and more robust results than both methods alone.

Another important thing to underline is that all of these results are obtained with only three months of observations (one Mercury orbit). This is encouraging in the concrete terms of the BepiColombo mission. The expected time span of the mission is around one year, but having the possibility to obtain valuable scientific results just from one fourth of the mission is certainly an insurance against shortening of the mission.

Finally, a comparison between these numerical results and formulas (2.24), (2.25) is presented in Table 2.7, where we have considered $\eta = \delta_1$ and a value of $\Omega = 67.7°$. It turns out that at least the order of magnitude is respected, but the two results are different by a factor of ~ 3. To explain clearly such a difference in terms of the much more complicated features of the numerical simulation, compared to the extreme simplifications of the analytical model, is a very tough problem. This is why complex and full numerical simulations are needed for the analysis of such rich and interrelated dynamical systems.

	$\sigma_\eta C_{20}/\sigma_{C_{20}}$	$\sigma_\epsilon C_{22}/\sigma_{C_{22}}$
Analytical result	0.66	0.70
Numerical simulation	0.19	0.27

Table 2.7: Comparison between the expected values, at least in terms of order of magnitude, for the formal uncertainties of δ_1 and ϵ_1 computed from formulas (2.24), (2.25).

A final comment turns to be very appropriate at this point, and it comes from the first approach to these problems by [Milani et al. 2001] and later by the same research group in 2003:

"It is not always the case that the results of a complex numerical simulation can be explained in simple terms. Indeed, the main reason why numerical simulations are needed is to take into account the full complexity of the solutions, with thousands of correlated parameters to be solved for. The relevance of each single parameter in isolation could be discussed with some analytical theory, or at least by order of magnitude arguments; the complexity of all the interactions is behind the reach of any analytical argument".

The Jupiter term. Few considerations must be made about the determination of the libration amplitude ϵ_2 due to Jupiter. As we anticipated in Sec. 2.5.1, the

determination of ϵ_2 is quite unstable and its success is strongly affected by the duration of the mission and by the phase of the periodic signal at the observation times. Additional experiments have been performed in order to test this problem.

With a period of ~ 11.8 years, the signal of $\epsilon_2 \cos(w_j (t - t_p) + \varphi_j)$ over ~ 88 days can be seen as a linear variation in ϕ of few arcsec, depending on the size of ϵ_2 and on the phase of the cosine at the time of the mission. For example, in the numerical simulation above, the choice of the initial condition is such that the variation due to the Jupiter term is about 5 arcsec/88 days. In this case the conditions are good enough to determine the rotation from gravimetry in a satisfactory way.

Other tests have been made in the worst cases, in which the variation is of $\sim 10^{-1}$ arcsec/88 days. In these cases the differential corrections give a solution for the gravity field orders of magnitude less accurate than the one in Fig. 2.12, a completely wrong solution for ϵ_2, and very high formal correlations (e.g. the correlation between S_{22} and ϵ_2 is ~ 0.9999, while in the previous favorable case was around 0.8).

The reasons for this instability lies in the fact that the Jupiter term contribution is a sinusoid whose behavior oscillates between a quasi-constant shift in ϕ, if the time of the mission is close to a stationary point, and a small secular variation, if the time of the mission is close to a stationary point of its derivative. If the secular variation is too small, the formal correlation between ϵ_2 and S_{22}, and in general with the whole gravity field, becomes very close to 1 because of formulas (2.29), (2.30). If we try to solve for both of them simultaneously, the global differential corrections can have numerical instabilities and even diverge, or they can give inaccurate results. Notice also that trying to absorb the Jupiter term by the constant S_{22} without determining ϵ_2 would introduce high systematic errors if the variation of ϕ is too large (e.g. more than one arcsec).

The conclusion is that, unless we are in favorable conditions with the phase of Jupiter to have a large variation of $\epsilon_2 \cos(w_j (t - t_p) + \varphi_j)$ (e.g. > 5 arcsec), we should recur to one of the following options:

- we have an a-priori knowledge of ϵ_2 with a good accuracy such that the error is small and it can be absorbed by the constant S_{22};
- we consider a more refined model for the libration in longitude, for example the semi-analytic ones described in [Dufey et al. 2009] and [Yseeboodt et al. 2010], which contain only the dynamical parameter $(B - A)/C_m$ to be determined.

2.8 Conclusions

The problem of the determination of the rotation state of Mercury from remote gravimetry has been described and analyzed in details. Even though not all of the complicated aspects of the theory of the rotation of Mercury have been included in the model, we have shown that the main quantities, obliquity and 88 days forced libration in longitude, can be determined processing three months of range and range rate tracking data in a

global least squares fit. Moreover, under suitable conditions, a significant libration term due to the Jupiter perturbation on Mercury's orbit can be also determined. In this context, global least squares fit means that a very large number of solve for parameters are determined all together:

- the coefficients of the spherical harmonics of the static gravity field of Mercury of degrees from 2 to 25, all (possible) orders;
- the tidal Love number for the second harmonic tides k_2;
- the rotation parameters δ_1, δ_2 for the direction of the spin axis of Mercury, the 88 days forced libration in longitude amplitude ϵ_1 and the 11.8 years forced libration in longitude amplitude ϵ_2 due to Jupiter;
- the accelerometer calibration parameters;
- the Mercurycentric initial conditions in some inertial frame for each arc.
- the dump maneuvers components, taking place during tracking and in the dark periods between each pair of subsequent arcs.

Some new features in the problem of the orbit determination of a s/c around Mercury have also been presented.

A new method to stabilize the orbit determination decomposed in a multi-arc structure has been proposed and successfully tested. In this way it has been possible to partially remove the rank deficiency due to the orbit determination around another planet [Bonanno & Milani 2002]. Moreover, special care has been taken in including dump maneuvers in the dynamics and in calibrating the on-board accelerometer by a new model based on cubic splines.

All the results turned out to be consistent with the standard requirements of the MORE experiment. In particular, the results regarding the rotation of Mercury were particularly good and encouraging, also in terms of the understanding the interior of Mercury. It is clear that several improvements need to be considered in modeling the rotation and in including it in a global least squares fit, especially to process real measurements. However, such complex numerical simulations, including thousands of parameters to be determined, need to be carefully designed, implemented and tested step by step.

Appendix A

The observation model

In this Appendix the observation model for the tracking range and range-rate, which has been used in the previous Chapter 2, is described in more detail. In principle, handling the observations is complicated not in terms of program structure, but because many conceptual problems have to be solved.

A.1 The light time iterations

As it is well known in space navigation [Moyer 2000], the *distance* to a spacecraft cannot be computed by an explicit analytic formula from the state of the ground station and the spacecraft at the same time. As discussed in [Milani & Gronchi 2010, Sec. 17.2] and [Tommei et al. 2010], the range is a function of five state vectors:

$$r = |(\mathbf{x}_{sat} + \mathbf{x}_M) - (\mathbf{x}_{EM} + \mathbf{x}_E + \mathbf{x}_{ant})| + S(\gamma), \tag{A.1}$$

where $\mathbf{x}_{sat}$ is the Mercurycentric position of the orbiter, $\mathbf{x}_M$ is the position of the center of mass of Mercury in a reference system with origin at the Solar System center of mass, $\mathbf{x}_{EM}$ is the position of the Earth-Moon center of mass in the same reference system, $\mathbf{x}_E$ is the vector from the Earth-Moon barycenter to the center of mass of the Earth, $\mathbf{x}_{ant}$ is the position of the reference point of the ground antenna with respect to the center of mass of the Earth. $S(\gamma)$ is the *Shapiro effect*, that is the difference between distance in flat space and the geodesic length in curved space-time, depending upon the relativistic Post Newtonian parameter γ.

These five vectors have to be computed at their own time, the epoch of different events in different time coordinates: e.g., $\mathbf{x}_{ant}$ is in Terrestrial Dynamical Time (TDT), $\mathbf{x}_{EM}$ and $\mathbf{x}_E$ are in Barycentric Dynamical Time (TDB), all these are measured at both the antenna *transmit time* t_t and the *receive time* t_r of the signal. $\mathbf{x}_M$ is computed in TDB, but at the *bounce time* t_b (when the signal has arrived to the orbiter and is sent back, with correction for the delay of the transponder). $\mathbf{x}_{sat}$ is computed at t_b in the time coordinate appropriate for the equations of motion for the Mercurycentric orbit, the Mercury Dynamical Time (TDM).

It can be shown that this implies the need for as many as four iteration loops, to compute $r, \dot{r}$ in the down-leg and up-leg paths. The computation of $\dot{r}$ needs to take into account that the derivatives with respect to the receive time contain corrections of order v/c for the light time and of order v^2/c^2 for the time coordinate transformations (where v is the relative velocity and c the velocity of light).

A.2 The time corrections

The changes in the time coordinates contain relativistic terms, and there are subtle problems in the PPN formulation. We believe a simple General Relativistic formulation (with $\beta = \gamma = 1$) will be accurate enough for our needs.

As discussed in Sec. B.1, we are using TDT, TDB and the newly defined proper time for Mercury TDM. The equation of motion of a Mercurycentric satellite can be approximated, to the required level of accuracy, by a Newtonian equation of motion provided the independent variable of the spacecraft equation of motion is the proper time of Mercury. Thus, it is necessary to define a new time coordinate TDM containing terms of post-Newtonian order 1 depending mostly upon the distance from the Sun r_{10} and velocity v_1 of Mercury. The relationship with the TDB scale, truncated to post-Newtonian order 1, is given by a differential equation

$$\frac{dt_{TDM}}{dt_{TDB}} = 1 - \frac{v_1^2}{2\,c^2} - \sum_{k \neq 1} \frac{G\,m_k}{c^2\,r_{1k}}$$

which can be solved by a quadrature formula once the orbits of Mercury, the Sun and the other planets are known. Figure A.1 plots the output of such a computation, showing a drift due to the non-zero average of the post-Newtonian term. The periodic term, with the period of Mercury orbit, is almost an order of magnitude larger than the difference TT-TDB. The time derivative of the periodic correction is $\simeq 10^{-8}$, in the formulas for the time correction of the range rate (see [Tommei et al. 2010]) it is multiplied by the velocity of Mercury $\simeq 50$ km/s, resulting in a change in range-rate by up to 0.05 cm/s, $\simeq 30$ times larger than the accuracy of range-rate with an integration time of 30 s.

A.3 Integrated observables

A problem known to the JPL Radio Science experts is that for top accuracy the range-rate measurement cannot be the instantaneous value $\dot{r}(t_r) = (\dot{r}_{up}(t_r) + \dot{r}_{do}(t_r))/2$. In fact, the measurement is not instantaneous: an accurate measure of a Doppler effect requires to fit the difference of phase between carrier waves, the one generated at the station and the one returned from space, accumulated over some *integration time* Δ, typically between 10 and 1000 s (see [Milani & Gronchi 2010], Chap.17). Thus the observable is really a difference of ranges

$$r(t_b + \Delta/2) - r(t_b - \Delta/2) = \int_{t_b - \Delta/2}^{t_b + \Delta/2} \dot{r}(s)\, ds$$

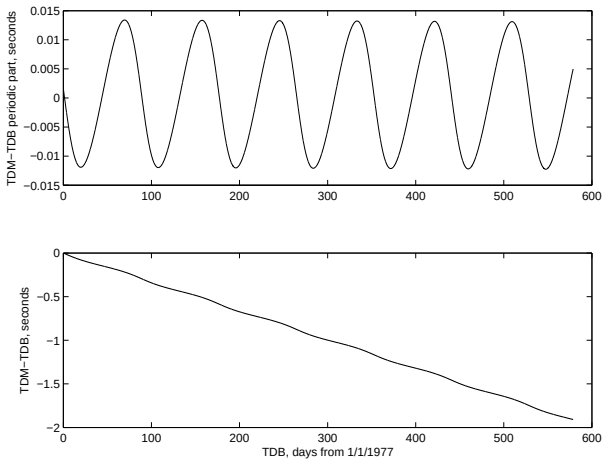

Figure A.1: Bottom: difference between the time coordinate TDM, in which the Mercurycentric orbit of the spacecraft is computed, and TDB, in which the planetary orbits are computed, as function of TDB. Top: the same difference after removing a linear trend, showing the dependence upon the distance between Mercury and the Sun.

or, equivalently, an averaged value of range-rate over the integration interval

$$\dot{r}_\Delta(t_r) = \frac{1}{\Delta} \int_{t_b-\Delta/2}^{t_b+\Delta/2} \dot{r}(s)\, ds \ . \tag{A.2}$$

The accuracy over 30 s of the range-rate measurement can be, by Gaussian statistics, $\simeq 3 \times 10^{-4} \sqrt{1000/30} \simeq 17 \times 10^{-4}$ cm/s, and the required accuracy in the computation of the difference $r(t_b+\Delta/2) - r(t_b-\Delta/2)$ is $\simeq 0.05$ cm. The distances can be as large as $\simeq 2 \times 10^{13}$ cm, thus the relative accuracy in the difference needs to be 2.5×10^{-15}. This implies that *rounding off* is a problem with current computers, with relative rounding off error of $2^{-52} = 2.2 \times 10^{-16}$. Extended precision is supported in software, but with many limitations. The practical consequences are that the computer program processing the tracking observables over interplanetary distances, at this level of precision, needs to use a mixture of ordinary and extended precision variables.

We have found that the use of a quadrature formula to approximate the integral of eq. (A.2) allows to control much better the rounding off problems, because the relative accuracy in range-rate is by no means as extreme as the one required to implement the $r(t_b + \Delta/2) - r(t_b - \Delta/2)$ computation.

Note that the range observations are also integrated, but the software of data preprocessing handles the conversion to a synthetic instantaneous measurement, made easy by the much larger accuracy of range-rate in measuring short term changes (Δ up to few minutes). Thus from the point of view of the orbit determination software, we can consider the range observations as instantaneous, as derived from convergence of the down-leg and up-leg iterations.

Appendix B

Global dynamics and relativistic models

As anticipated in Sec. 2.1.2, the dynamics which affect the observables, in addition to the Mercurycentric one already described in Sec. 2.5, are described in the following. In general, we need to add the consultation of the planetary ephemerides to all these dynamics.

B.1 Solar System Barycentric orbits of Mercury and the Earth-Moon barycenter

The orbit of the planets Mercury and of the Earth-Moon Barycenter (EMB) in the Solar System must have an equation of motion including:

- the Newtonian attraction from the Sun and the planets;
- the relativistic PPN corrections, including the PN parameters γ, β;
- the effects of possible violations of General relativity, including violations of the Strong Equivalence Principle, preferred frame effects and changes in the gravitational constant;
- the dynamic oblateness of the Sun.

Note that for the EMB each one of these attractions has to be computed as the resultant attraction on the Earth and Moon. The time in which these equations apply is the **Barycentric Dynamical Time (TDB)**; care must be taken in the scaling of the mass of the Sun, which is aliased to many other effects, including violation of equivalence principle, problems in time definition, etc.

The current state, as a function of time, of the planets Venus and Mars to Neptune are read from the JPL ephemerides (currently the DE406 version) as Chebichev polynomials, which are interpolated with the JPL well tested algorithm. The same applies to the

geocentric orbit of the Moon, also used to compute the vector from the EMB to the center of the Earth. We have also implemented the algorithms needed to take into account asteroid perturbations on the orbit of the EMB.

The structure for this equation of motion is defined in the following and it is based on a Lagrangian formulation.

The most compact way to describe the orbital effects related to PPN parameters and in general to other perturbations is to express them through additional terms in the Lagrangian description of the planetary dynamics. Let us assume that the motion of the planets is described by the sum of different Lagrangian functions:

$$L = L_{new} + L_{GR} + (\gamma - 1)L_{\gamma} + (\beta - 1)L_{\beta} + \zeta\, L_{\zeta} + J_{2\odot}L_{J2\odot} + \alpha_1 L_{\alpha_1} + \alpha_2 L_{\alpha_2} + \eta L_{\eta}$$

where L_{new} is the Lagrangian of the Newtonian N-body problem, L_{GR} is the corrective term taking into account general relativity in the Post-Newtonian approximation, L_{γ} and L_{β} are the terms taking into account the PPN parameters γ and β respectively, L_{ζ} is the Lagrangian for the time variation of the gravitational parameter of the Sun $Gm_{\odot}$, $L_{J2\odot}$ takes into account the effect due to the oblateness of the Sun, L_{α_1}, L_{α_2} describe the preferred-frame effects through the parameters α_1, α_2, and finally L_{η} checks for possible violations of the strong equivalence principle. Two references describing in more detail this approach are [Milani et al. 2002] and [Milani et al. 2010].

Notation: Hereafter we will follow the notation of [Moyer 2000]:

$$\vec{r}_{ij} = \vec{r}_j - \vec{r}_i, \qquad r_{ij} = |\vec{r}_{ij}|\,,$$

$$\vec{v}_{ij} = \dot{\vec{r}}_j - \dot{\vec{r}}_i = \vec{v}_j - \vec{v}_i, \qquad v_{ij} = |\vec{v}_{ij}|\,,$$

$$\vec{a}_{ij} = \ddot{\vec{r}}_j - \ddot{\vec{r}}_i = \vec{a}_j - \vec{a}_i,$$

for $i, j = 0, N$, where the index 0 refers to the Sun, the indexes $1, 2, 3$ to Mercury, Earth and Moon, respectively. In our software we are going to propagate only for the motion of Mercury and of the EMB, because these are the two dynamics that we need to solve for in the MORE experiment. The other planetary dynamics, as well as the relative positions EMB-Earth and EMB-Moon, are given by the JPL ephemerides. There is no way to determine the masses of the Earth and of the Moon from the MORE experiment independently, so what we determine is the total mass of the EMB $\mu_{EMB} = \mu_2 + \mu_3$, while the mass ratio $emratio = \mu_2/\mu_3$ is assumed to be a consider parameter. If $\mu_E = emratio/(1 + emratio)$ and $\mu_M = 1/(1 + emratio)$ we have:

$$\vec{r}_{EMB} = \mu_E\, \vec{r}_2 + \mu_M\, \vec{r}_3 \tag{B.1}$$

and analogous formulas for velocity and acceleration.

Notice that the usual Lagrangian functions are multiplied by G, so that only the gravitational masses $\mu_i = G\,m_i$ appear in the overall Lagrangian; indeed the gravitational constant cannot be determined by any form of orbit determination (apart artificial systems). The equations of motion for each body remain the same. Each Lagrangian will be described in the following.

N-body Newtonian Lagrangian:

$$L_{new} = \frac{1}{2}\sum_i \mu_i\, v_i^2 + \frac{1}{2}\sum_i \sum_{j\neq i} \frac{\mu_i \mu_j}{r_{ij}}.$$

Post-Newtonian General Relativistic Lagrangian:

$$\begin{aligned} L_{GR} &= \frac{1}{8\,c^2}\sum_i \mu_i v_i^4 - \frac{1}{2\,c^2}\sum_i \sum_{j\neq i}\sum_{k\neq i} \frac{\mu_i\,\mu_j\,\mu_k}{r_{ij}\,r_{ik}} + \\ &+ \frac{1}{2}\sum_i \sum_{j\neq i} \frac{\mu_i\,\mu_j}{r_{ij}}\left[\frac{3}{2c^2}(v_i^2+v_j^2) - \frac{7}{2\,c^2}(\vec{v_i}\cdot\vec{v_j}) - \frac{1}{2\,c^2}(\vec{n_{ij}}\cdot\vec{v_i})(\vec{n_{ij}}\cdot\vec{v_j})\right]. \end{aligned}$$

PPN γ Lagrangian:

$$L_\gamma = \frac{1}{2\,c^2}\sum_i \sum_{j\neq i} \frac{\mu_i\,\mu_j}{r_{ij}}(\vec{v_i}-\vec{v_j})^2.$$

PPN β Lagrangian:

$$L_\beta = -\frac{1}{c^2}\sum_i \sum_{j\neq i}\sum_{k\neq i} \frac{\mu_i\,\mu_j\,\mu_k}{r_{ij}\,r_{ik}}.$$

PPN ζ Lagrangian: L_ζ describes the effect due to a time variation of the gravitational parameter of the Sun $\mu_0 = Gm_\odot$:

$$\mu_0 = \mu_0(t_0) + \dot{\mu}_0(t_0)(t-t_0) + \ldots$$

defining

$$\zeta = \frac{\dot{\mu}_0(t_0)}{\mu_0(t_0)} = \frac{d}{dt}\ln(\mu_0)(t_0)$$

we have

$$L_\zeta = (t-t_0)\sum_{i\neq 0}\frac{\mu_0\mu_i}{r_{0i}}.$$

$J_{2\odot}$ effect Lagrangian:

$$L_{J_{2\odot}} = -\frac{1}{2}\sum_{i\neq 0}\frac{\mu_0\,\mu_i}{r_{0i}}\left(\frac{R_0}{r_{0i}}\right)^2 [3(\mathbf{n}_{0i}\cdot\mathbf{e}_0)^2 - 1]$$

where R_0 is the radius of the Sun, $\mathbf{n}_{0i} = \mathbf{r}_{0i}/r_{0i}$ is the heliocentric position of the body i and $\mathbf{e}_0$ is the unit vector along the rotation axis of the Sun. The unit vector

$\mathbf{e}_0$ is given in standard equatorial coordinates with equinox J2000 at epoch J2000 in [Seidelmann et al. 2006]: $\alpha_0 = 286.13°$, $\delta_0 = 63.87°$.

Lagrangian for preferred frame effect, PPN α_1 and α_2:

$$L_{\alpha_1} = -\frac{1}{4\,c^2}\sum_j\sum_{i\neq j}\frac{\mu_i\,\mu_j}{r_{ij}}\,(\vec{z}_i\cdot\vec{z}_j)\,,$$

$$L_{\alpha_2} = \frac{1}{4\,c^2}\sum_j\sum_{i\neq j}\frac{\mu_i\,\mu_j}{r_{ij}}\,[(\vec{z}_i\cdot\vec{z}_j) - (\vec{n_{ij}}\cdot\vec{z}_i)\,(\vec{n_{ij}}\cdot\vec{z}_j)]\,,$$

where $\vec{z}_i = \vec{w} + \vec{v_i}$ and $\vec{w}$ is the velocity of the considered reference system with respect to the PPN preferred reference frame, which is a reference frame whose outer regions are at rest with respect to the universe rest frame (see [Will 1993]). In the case of the Solar System barycentric reference frame, that could be the one of cosmic microwave background, $|\vec{w}| = 370 \pm 10$ km/s, in the direction $(\alpha, \delta) = (168°, 7°)$ in the Equatorial J2000 reference frame (see [Milani et al. 2002]). Notice that we can combine the two previous Lagrangian and the parameters α_1 and α_2 obtaining a unique Lagrangian for the preferred frame effects:

$$\begin{aligned} L_\alpha = \alpha_1\,L_{\alpha_1} + \alpha_2\,L_{\alpha_2} &= \frac{\alpha_2-\alpha_1}{4\,c^2}\sum_j\sum_{i\neq j}\frac{\mu_i\,\mu_j}{r_{ij}}\,(\vec{v_i}+\vec{w})\cdot(\vec{v_j}+\vec{w}) + \\ &- \frac{\alpha_2}{4\,c^2}\sum_j\sum_{i\neq j}(\vec{r_{ji}}\cdot(\vec{v_j}+\vec{w}))\,(\vec{r_{ji}}\cdot(\vec{v_i}+\vec{w}))\frac{\mu_i\,\mu_j}{r_{ij}^3}. \end{aligned}$$

Lagrangian for possible violation of the equivalence principle: With the Lagrangian multiplied by G, the Newtonian kinetic energy is

$$T = \frac{1}{2}\sum_i \mu_i\,v_i^2\ ,$$

that is we assume that the inertial mass and the gravitational mass are the same (at least exactly proportional). If some form of mass has a different gravitational coupling, there are for each body i two quantities μ_i and μ_i^I, one appearing in the gravitational potential (including the relativistic part) and the other appearing in the kinetic energy. If there is a violation of the strong equivalence principle involving body i, with a fraction Ω_i of its mass due to gravitational self-energy (for the moment we are using the approximation with constant density: $\Omega_i = -3\mu_i/5Rc^2$, notice that Ω_i is $O(c^{-2})$):

$$\mu_i = (1+\eta\Omega_i)\,\mu_i^I \Longleftrightarrow \mu_i^I = (1-\eta\Omega_i)\,\mu_i + \mathcal{O}(\eta^2)$$

with η a Post-Newtonian parameter for this violation. Neglecting $\mathcal{O}(\eta^2)$ terms (also $\mathcal{O}[\eta\,(\gamma-1)]$ etc.) this is expressed by a Lagrangian term $\eta\,L_\eta$ where

$$L_\eta = -\frac{1}{2}\,\sum_i \Omega_i\,\mu_i\,v_i^2\ .$$

Equations of motion

If we consider an inertial reference system, the equations of motion for the i-th body are described by the Lagrangian equations:

$$\frac{d}{dt}\frac{\partial L}{\partial \vec{v}_i} = \frac{\partial L}{\partial \vec{r}_i},$$

which in general gives an implicit expression for the acceleration of the form $f(\vec{a}_i) = g(\vec{r}_i, \vec{v}_i)$. However, since the main term is the N-body Newtonian acceleration $\vec{a}_i^{new}$ and the other terms are small perturbations, we can use the following approximation for the total acceleration of the i-th body:

$$\mu_i \vec{a}_i = \mu_i \vec{a}_i^{new} + \frac{\partial (L - L_{new})}{\partial \vec{r}_i} - \left[\frac{d}{dt}\frac{\partial (L - L_{new})}{\partial \vec{v}_i}\right] |_{\vec{a}_i = \vec{a}_i^{new}}.$$

Since we are propagating only for the motion of Mercury and of the EMB, if we call $Y = [\vec{r}_1, \vec{r}_{EMB}, \vec{v}_1, \vec{v}_{EMB}]^T$ the 12-dimensional state vector that we want to propagate, we can write the equations of motion in the more complete form:

$$\frac{d}{dt}Y = \begin{pmatrix} \vec{v}_1 \\ \vec{v}_{EMB} \\ \vec{a}_1 \\ \vec{a}_{EMB} \end{pmatrix} = F(\vec{r}_1, \vec{r}_{EMB}, \vec{v}_1, \vec{v}_{EMB}, ...). \tag{B.2}$$

The reference system for these dynamics is centered in the Solar System Barycenter, and it is inertial in the Post-Newtonian approximation. On the other hand, if we consider possible violations from it, as it is the PPN formalism, we need to reconsider the total linear momentum conservation theorem.

Linear momentum

Using Noether's Theorem we can compute the integral of the total linear momentum of the system:

$$\frac{d}{dt}\vec{P} = 0\,, \qquad \text{where} \qquad \vec{P} = \sum_i \frac{\partial L}{\partial \vec{v}_i}.$$

Since L_β, L_ζ, $L_{J2\odot}$ do not depend on velocities and, because of the antisymmetry, $\sum_i \frac{\partial L_\gamma}{\partial \vec{v}_i} = 0$ and L_γ does not contribute, the total linear momentum of the system reads:

$$\vec{P} = \sum_i \frac{\partial (L_{new} + L_{GR} + L_\alpha + \eta L_\eta)}{\partial \vec{v}_i}. \tag{B.3}$$

In the Post-Newtonian approximation the total linear momentum is simply:

$$\vec{P} = \sum_i \frac{\partial (L_{new} + L_{GR})}{\partial \vec{v}_i} = \tag{B.4}$$

$$= \sum_i \mu_i \vec{v}_i \left[1 + \frac{1}{2c^2}v_i^2 - \frac{1}{2\,c^2}\sum_{k\neq i}\frac{\mu_k}{r_{ik}}\right] - \frac{1}{2\,c^2}\sum_i\sum_{k\neq i}\frac{\mu_i\mu_k}{r_{ik}}\left(\vec{n_{ik}}\cdot\vec{v_k}\right)\vec{n_{ik}} \tag{B.5}$$

and the vector

$$\vec{R} = \sum_i \mu_i \vec{r_i} \left(1 + \frac{1}{2c^2} v_i^2 - \frac{1}{2\,c^2} \sum_{k \neq i} \frac{\mu_k}{r_{ik}} \right) \tag{B.6}$$

is such that

$$\frac{d}{dt}\vec{R} = \vec{P}$$

to the $O(c^{-2})$ level of accuracy. Thus $\vec{R}$ (rescaled by the total mass) plays the role of the barycenter of the Solar System and can be used to eliminate the Sun from the equations of motion:

$$\vec{r_0} = -\frac{\sum_{i\neq 0} \mu_i \vec{r_i} \left(1 + \frac{v_i^2}{2\,c^2} - \frac{U_i}{2\,c^2}\right)}{\mu_0 \left(1 + \frac{v_0^2}{2\,c^2} - \frac{U_0}{2\,c^2}\right)}, \qquad U_i = \sum_{k\neq i} \frac{\mu_k}{r_{ik}}.$$

If we now take into account the PPN parameters effects, we can write the linear momentum as

$$\vec{P} = \vec{P_0} + \vec{P_\alpha}\,, \qquad \vec{P_0} = \sum_j \frac{\partial (L_{new} + L_{GR} + \eta\, L_\eta)}{\partial \vec{v_j}}\,, \qquad \vec{P_\alpha} = \sum_j \frac{\partial L_\alpha}{\partial \vec{v_j}}.$$

In this way, defining the center of mass of the system (rescaled by the total mass) as

$$\vec{R} = \sum_i \mu_i (1 - \eta\Omega_i) \vec{r_i} \left(1 + \frac{1}{2c^2} v_i^2 - \frac{1}{2\,c^2} \sum_{k \neq i} \frac{\mu_k}{r_{ik}} \right) \tag{B.7}$$

we have

$$\frac{d}{dt}\vec{R} = \vec{P}_0,$$

and the position of the Sun in this barycentric system is now

$$\vec{r_0} = -\frac{\sum_{i\neq 0} \mu_i (1 - \eta\Omega_i) \vec{r_i} \left(1 + \frac{v_i^2}{2\,c^2} - \frac{U_i}{2\,c^2}\right)}{\mu_0 (1 - \eta\Omega_0) \left(1 + \frac{v_0^2}{2\,c^2} - \frac{U_0}{2\,c^2}\right)}. \tag{B.8}$$

But now, since

$$\dot{\vec{P}} = 0 \Longrightarrow \dot{\vec{P}}_0 = -\dot{\vec{P}}_\alpha \Longrightarrow \ddot{\vec{R}} = -\dot{\vec{P}}_\alpha,$$

it means that the barycentric reference frame is accelerated. Thus the equations of motion for the i-th body in this reference frame need to be corrected by the acceleration of the barycenter $\vec{B}$, keeping the $O(c^{-2})$ level of accuracy:

$$\vec{a}_i = \vec{a}_i^{new} + \frac{1}{\mu_i} \frac{\partial (L - L_{new})}{\partial \vec{r_i}} - \left[\frac{d}{d\,t} \frac{\partial (L - L_{new})}{\partial \vec{v_i}} \right] |_{\vec{a}_i = \vec{a}_i^{new}} - \ddot{\vec{B}},$$

where

$$\vec{B} = \frac{\vec{R}}{\sum_i \mu_i \,(1 - \eta\,\Omega_i) \left(1 + \frac{v_i^2}{2\,c^2} - \frac{U_i}{2\,c^2}\right)}.$$

B.2 Rotational dynamics of the Earth

Since there is no way to solve for Earth rotation parameters from observations at Mercury (at accuracies competitive with other available measurements), we are using the interpolation tables made public by the International Earth Rotation Service (IERS).

The same argument applies to the station coordinates, which we have to assume are supplied by the ground station with the required accuracy, including corrections for the antenna motion.

The IERS tables are currently used in the old (IAU 1976) formulation, later to be replaced by the new (IAU 2000) formulation. The difference is irrelevant for simulations, while it could matter for the processing of the real data at top accuracy.

Acknowledgements

The funding for this work was provided by the University of Pisa, Scuola di Dottorato Galileo Galilei, Department of Mathematics, and by the Mercury Orbiter RadioScience Experiment under Italian Space Agency contract.

Bibliography

[Anderson et al. 1987] Anderson J.D., Colombo G.,Esposito P.B., Lau E.L., Trager T.B.: *The mass, gravity field and ephemeris of Mercury.* Icarus. **71** 337-349, (1987).

[Balogh et al. 2002] Balogh A., Giampieri G., *Mercury: the planet and its orbit.* Reports on Progress in Physics, Space and Atmospheric Physics, Imperial College, London SW7 2BW, UK. **65** 529-560, (2002).

[Balogh et al. 2000] Balogh, A. et al.: *BepiColombo: an interdisciplinary Cornerstone Mission to the planet Mercury.* ESA-SCI (2000)1.

[Benkhoff et al. 2010] Benkhoff J., *BepiColombo-Comprehensive exploration of Mercury: Mission overview and science goals.* Planetary & Space Science , **58**, 2-20 (2010).

[Bonanno & Milani 2002] Bonanno C., Milani A.: *Symmetries and rank deficiency in the orbit determination around another planet.* CM& DA **83**, 17-33, (2002).

[Colombo and Shapiro 1966] Colombo G., Shapiro, I.I., *The rotation of the planet Mercury.* Astrophys. J. 145, 296, (1966).

[D'Hoedt & Lemaitre 2004] D'Hoedt S. & Lemaitre A.: *The spin-orbit resonant rotation of Mercury: A two degree of freedom Hamiltonian model.* Celestial Mechanics and Dynamical Astronomy, 89, 267-283 (2004)

[D'Hoedt et al. 2009] D'Hoedt S., Noyelles B., Dufey J., Lemaitre A.: *Determination of an instantaneous Laplace plane for Mercury's rotation.* Adv. in Space Res. **44**, 597-603 (2009).

[Dufey et al. 2008] Dufey J., Lemaitre A., Rambaux N.: *Planetary perturbations on Mercury's libration in longitude.* Celest Mech Dyn Astr. **101**, 141-157, (2008).

[Dufey et al. 2009] Dufey, J., Noyelles, B., Rambaux, N., Lemaître, A.: *Latitudinal librations of Mercury with a fluid core.* Icarus, 203, 1-12 (2009).

[Dunning 1973] Dunning R.S.: *The orbital mechanics of flight mechanics.* NASA, Langley Research Center and Scientific and Techical Information Office, NTIS, Springfield (1973).

[Garcia et al. 2009] Garcia D.,Jehn R.,Schoenmaekers J.,de Pascale P.: *BepiColombo Mercury Cornerstone Current Report on Mission Analysis* . MAO Working Paper No. 525 BC-ESC-RP-05500, Issue 3.1 (2009).

[Iafolla and Nozzoli 2001] Iafolla V., Nozzoli S., *Italian Spring Accelerometer (ISA): a high sensitive accelerometer for BepiColombo ESA Cornerstone.* Planet. Space Sci. **49**, (2001).

[Iafolla et al. 2011] Iafolla V., Lucchesi D.M., Nozzoli S., Santoli F.: *The Bepicolombo mission to Mercury: Reaction wheels desaturation manoeuvres and the ISA accelerometer* $\Delta \mathbf{v}$ *measurements.* Planet. Space Sci. **59**, 51-62, (2011).

[Iess & Boscagli 2001] Iess L., Boscagli G., *Advanced radio science instrumentation for the mission BepiColombo to Mercury.* Planet. and Space Sci., Volume 49, Issue 14-15, p. 1597-1608, (2001).

[Jehn et al. 2004] Jehn R., Corral C., Giampieri G.: *Estimating Mercury's 88-day libration amplitude from orbit.* Planet. and Space Sci. **52** 727-732, (2004).

[Kaula 1966] Kaula W.M.: *Theory of satellite geodesy.* Blaisdell, Waltham, MA, (1966).

[Kozai 1965] Kozai Y.: *Effects of the Tidal deformation of the Earth on the Motion of Close Earth Satellites* . A.J, **17**, 395 (1965).

[Margot et al. 2007] Margot, J.L., Peale, S.J., Jurgens, R.F., Slade, M.A., Holin, I.V.: *Large longitude libration of Mercury reveals a molten core.* Science 316, 710-714 (2007)

[Marra et al. 2005] Marra G., Colangeli L., Mazzotta Epifani E., Palumbo P., Flamini E., Debei S.: *Optical design of a high-resolution imaging channel for the Bepi Colombo space mission.* Building European OLED Infrastructure. Edited by Pearsall, Thomas P.; Halls, Jonathan. Proceedings of the SPIE, Volume 5962, pp. 501-508 (2005)

[Milani et al. 1987] A. Milani, A.M. Nobili and P. Farinella, *Non-gravitational perturbations and satellite geodesy*, Adam Hilger, Bristol (1987).

[Milani et al. 2001] Milani A., Rossi A., Vokroulicky D., Villani D., Bonanno C.: *Gravity field and rotation state of Mercury from the BepiColombo Radio Science Experiments.* Planet. Space Sci. **49**, 1579-1596, (2001).

[Milani et al. 2002] Milani,A., Vokrouhlicky,D., Villani,D., Bonanno,C., Rossi,A.: *Testing general relativity with the BepiColombo Radio Science Experiment*, Phys. Rev. D **66** (2002).

[Milani et al. 2010] Milani,A., Tommei,G., Vokrouhlicky,D., Latorre,E., Cicalò,S.: *Relativistic models for the BepiColombo radioscience experiment*, Proceedings IAU Symposium No. **261** (2010).

[Milani & Gronchi 2010] Milani A., Gronchi G.F., *Theory of orbit determination*, Cambridge University Press, (2010).

[Moyer 2000] Moyer, T. D. *Formulation for Observed and Computed Values of Deep Space Network Data Types for Navigation*, NASA-JPL, Deep Space Communication and Navigation Series, Monograph 2, October 2000.

[Noyelles et al. 2010] Noyelles, B., Dufey, J., Lemaitre A.: Core-mantle interactions for Mercury, MNRAS, **000**, 1-29 (2010)

[Noyelles & D'Hoedt 2011] Noyelles, B., D'Hoedt S.: *Modeling the obliquity of Mercury,* under revision (2011).

[Peale 1969] Peale S.J., *Generalized Cassini's laws.* The Astronomical Journal, Volume 74, Number 3, 1969.

[Peale 1988] Peale S.J., *Rotational dynamics of Mercury and the state of its core.* IN: Mercury (A89-43751 19-91). University of Arizona press, Tucson, AZ, pp.461-493, 1988.

[Peale 2006] Peale S.J., *The proximity of Mercury's spin to Cassini state 1.* Icarus, Volume 181, Issue 2, p. 338-347, 2006.

[Peale et al. 2007] Peale S.J., Yseboodt M., Margot J.L.: *Long period forcing of Mercury's libration in longitude.* Icarus, Volume 187, p. 365-373, 2007.

[Peale et al. 2009] Peale S.J., Yseboodt M., Margot J.L.: *Resonant forcing onf Mercury's libration in longitude.* Icarus, Volume 199, p. 1-8, 2009.

[Roy 2005] Roy A.E.: *Orbital Motion*, 4th ed., Taylor & Francis Group (2005).

[Sanchez et al. 2006] Sánchez Ortiz N., Belló Mora M., Jehn R.: *BepiColombo mission: Estimation of Mercury gravity field and rotation parameters.* Acta Astronautica, Volume 58, p. 236-242, 2006.

[Stiles et al. 2008] Stiles, B.W., Kirk, R.L., Lorenz, R.D., Hensley, S., Lee, E., Ostro, S.J., Allison, M.D., Callahan, P., Gim, Y., Iess, L., Persi del Marmo, P., Hamilton, G:, Johnson, W.T.K., West, R. and the Cassini RADAR Team: *Determining Titan's Spin State from Cassini RADAR images*, The Astronomical Journal, **135**, 1669-1680, (2008).

[Seidelmann et al. 2006] Seidelmann,P.K. et al.: *Report fo the IAU/IAG Working Group on Cartographic Coordinates and Rotational Elements of the Planets and Satellites*, CM&DA **98** 155-180 (2006).

[Tommei et al. 2010] Tommei G., Milani A., Vokrouhlicky D.: *Light-time computations for the BepiColombo Radio Science Experiment*, CM&DA **107** 285-298 (2010).

[Yseeboodt and Margot 2006] Yseboodt M., Margot J.L., *Evolution of Mercury's obliquity.* Icarus, Volume 181, Issue 2, p. 327-337, 2006.

[Yseeboodt et al. 2010] Yseboodt M., Margot J.L., Peale S.J.: *Analytical model of the long-period forced longitude librations of Mercury.* Icarus, **207**, p. 536-544, 2010.

[Wigner 1959] Wigner, E.P..: *Group Theory and its Applications to the Quantum Mechanics of Atomic Spectra*, Academic Press, New York (1959).

[Will 1993] Will, C.M.: *Theory and experiment in gravitational physics*, Cambridge University Press (1993).

[Wu et al. 1995] Wu X., Bender P.L., Rosborough G.W.: *Probing the interior structure of Mercury from an orbiter plus single lander*, J. of Geophys. Res., **100**, 1515-1525 (1995).

Part II

Rotational dynamics of asteroids under non-gravitational perturbations

Chapter 3

Averaged rotational dynamics of an asteroid in tumbling rotation under the YORP torque

The content of this Chapter was published in April 2010, in the journal with international referee *Celestial Mechanics and Dynamical Astronomy*, Volume 106, Issue 4, pp.301-337.

3.1 Introduction

The aim of this work is to study the rotational dynamics of a celestial body under the YORP torque. The YORP (Yarkovsky-O'Keefe-Radzievskii-Paddack) torque is the consequent effect to infrared thermal emission from the surface of a body irradiated by the Sun, and was first introduced in [Rubincam 2000]. This effect is mainly important for the rotational dynamics of small solar system bodies, particularly asteroids of size < 10 km. Specifically, it can have a strong influence on the evolution of the obliquity and of the rotation rate of these bodies, and it may have also a role in the creation of binary asteroids.

The dynamics of the YORP effect has been previously studied by many authors and in different ways. With numerical models by
[Capek & Vokrouhlicky 2004] and [Vokrouhlicky & Capek 2002].
An analytical description of the effect is given, for example, in
[Nesvorny & Vokrouhlicky 2007], in [Scheeres & Mirrahimi 2008] and more recently in [Mysen 2008]. As the YORP torque is a small torque, it can be treated as a perturbation to the unperturbed rotational motion, and the important effects are then secular ones over long time spans. Thus the analytical solutions given in these papers are basically first order, in the small quantity YORP torque over angular momentum, averaged solutions over the rotational and the orbital motion of the asteroid, and they are based on the hypothesis of principal axis rotation around the maximum moment of inertia.

However, there are examples of asteroids which are not in principal axis rotation,

said to be in tumbling rotation, and in such cases the previous analytical models cannot be applied (see [Hudson & Ostro 1995]). The first work dedicated to the study of these rotators was [Vokrouhlicky et al. 2007], in which a full numerical integration of the equations of motion is performed. In this work we derive a first analytical theory that can explain the secular evolution behavior of a non-principal axis rotator.

In [Neishtadt et al. 2003] and [Sidorenko et al. 2008] the generic evolutionary equations for an outgassing comet nucleus rotation were developed. Here we will follow a similar approach, looking for the averaged first order equations of a generic rigid body under the thermal YORP torques, without the hypothesis of principal axis rotation.

In addition to the so called "Rubincam's approximation", which consists of assuming zero thermal conductivity for the surface of the body, there are some others limitations in our analytical approach, in particular in modelling the illuminated-shaded portion of the body's surface hit by the Sun. We should continue to use general, non-convex bodies in our studies but note that we make the strong approximation that there is no self-shadowing – i.e., model them as locally convex. Thus this work does not pretend to be a complete analytical theory of tumbling rotators under YORP, but is a first step in this direction.

The solution of the evolutionary equations that we find turns out to be easily describable in terms of few suitable quantities. The results and the conclusions that we find here include and are in agreement with the previous analytical results about principal axis rotators, but they are only partially in agreement with the numerical results in [Vokrouhlicky et al. 2007], although they have in common all of the main features seen in that work. Better approximations are needed and we briefly discuss some possible generalizations of the theory in a qualitative way.

In section 2 we describe the full differential equations of the rotational dynamics of a rigid body under a torque, and we define the fundamental reference systems. We describe the equations for the YORP torque and for the energy dissipation dynamics. Under the assumption of no resonance between the rotation of the body and its orbital motion, in section 3 we obtain the first order (in the small parameter YORP torque over angular momentum) averaged equations for the angular momentum vector $\mathbf{L}$ of the asteroid and for the so called dynamic inertia I_D, which is a parameter related to the non-principal rotation mode of the body. In section 4 we discuss the dynamics without energy dissipation for the angular momentum vector and the dynamic inertia along with some important generalizations. In section 5 we describe the chaotic behavior of the rotational dynamics when the body is close to the critical solution $I_D = B$, where B is the intermediate moment of inertia. Finally in section 6 we apply our analytical results to some real asteroid shape models.

3.2 Rotational dynamics

Our dynamical problem is the rotation of a rigid body under a torque. In order to write the differential equations that describe this dynamics, we have to define some suitable reference systems.

3.2.1 Reference systems

The first important reference system is the body fixed, principal axis of inertia system. We indicate with ξ, η, ζ the coordinates relative to the principal inertia axes. In particular ξ is relative to the minimum moment A, η to the intermediate moment B, and ζ to the maximum moment of inertia C.

The second system that we define is the inertial, orbital reference system X, Y, Z. Where $\mathbf{Y}$ is normal to the orbit and $\mathbf{Z}$ is along the perihelion direction.

The third system is the angular momentum reference system, that we indicate with x, y, z. Where $\mathbf{z}$ is along the angular momentum vector direction ($\mathbf{L} = L\mathbf{z}$), and the axis $\mathbf{y}$ lies in the plane $(\mathbf{X}, \mathbf{Y})$.

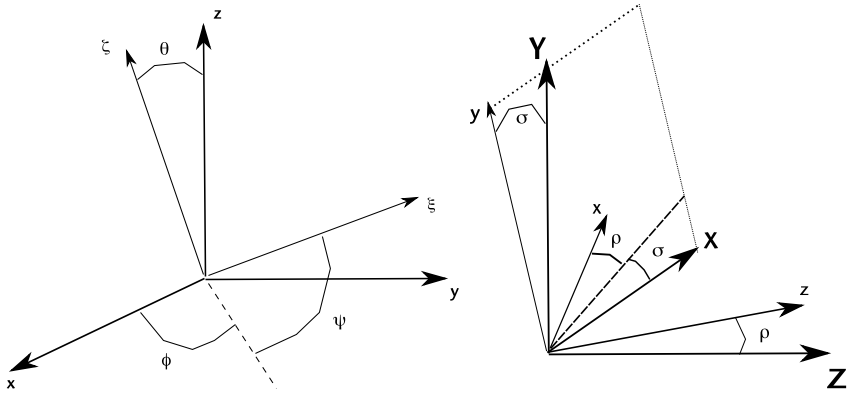

Figure 3.1: On the left the angular momentum reference system x, y, z and the body fixed reference system ξ, η, ζ, related by the Euler angles ϕ, θ, ψ. On the right the orbital reference system X, Y, Z and the angular momentum reference system related by the rotation angles ρ, σ.

3.2.2 Angular variables

The previous reference systems can be related to each other by suitable rotations, and the coordinates by suitable rotation matrices. To move the x, y, z reference system to the ξ, η, ζ, we need one rotation of ϕ around the third axis, one rotation of θ around the first axis and one rotation of ψ around the third axis. To move the X, Y, Z reference

system to the x, y, z, we need one rotation of σ around the third axis and one rotation of ρ around the second axis.

The rotation coefficients are given by the following formulas.

From the inertial orbital system to the angular momentum system:

$$a_{x\,X} = \cos\sigma\cos\rho, \qquad a_{x\,Y} = \sin\sigma\cos\rho, \qquad a_{x\,Z} = -\sin\rho,$$

$$a_{y\,X} = -\sin\sigma, \qquad a_{y\,Y} = \cos\sigma, \qquad a_{y\,Z} = 0,$$

$$a_{z\,X} = \cos\sigma\sin\rho, \qquad a_{z\,Y} = \sin\sigma\sin\rho, \qquad a_{z\,Z} = \cos\rho.$$

From the body fixed system to the angular momentum system (type II Euler angles):

$$a_{x\,\xi} = \cos\phi\cos\psi - \sin\phi\sin\psi\cos\theta,$$

$$a_{x\,\eta} = -\cos\phi\sin\psi - \sin\phi\cos\psi\cos\theta, \qquad a_{x\,\zeta} = \sin\theta\sin\phi,$$

$$a_{y\,\xi} = \sin\phi\cos\psi + \cos\phi\sin\psi\cos\theta,$$

$$a_{y\,\eta} = -\sin\phi\sin\psi + \cos\phi\cos\psi\cos\theta, \qquad a_{y\,\zeta} = -\sin\theta\cos\phi,$$

$$a_{z\,\xi} = \sin\theta\sin\psi, \qquad a_{z\,\eta} = \sin\theta\cos\psi \qquad a_{z\,\zeta} = \cos\theta.$$

Notice that the $a_{z\,*}$ terms are the only ones that do not depend on the angle ϕ.

3.2.3 The rotation dynamical system

We can describe the rotational dynamics of the rigid body using the angles θ, ϕ, ψ, which describe the rigid motion with respect to the angular momentum system, the angles ρ, σ and the angular momentum magnitude L, which describes the inertial motion of the angular momentum vector $\mathbf{L}$.

In the unperturbed problem, i.e., with zero torque, we have an analytical, periodic, solution for the angles θ, ϕ, ψ (Euler-Poinsot solution) in terms of elliptic functions, while ρ, σ, L are constants, see [MacMillan 1936].

According to [Neishtadt et al. 2003], the rotation dynamical system is given by

$$\begin{aligned}
\frac{d\,\theta}{d\,t} &= L\sin\theta\sin\psi\cos\psi(\frac{1}{A} - \frac{1}{B}) + \frac{1}{L}[(M_\xi\sin\psi + M_\eta\cos\psi)\cos\theta - M_\zeta\sin\theta], \\
\frac{d\,\phi}{d\,t} &= L(\frac{\sin^2\psi}{A} + \frac{\cos^2\psi}{B}) - \frac{M_x}{L}\cos\phi\cot\theta - \frac{M_y}{L}(\cot\rho + \sin\phi\cot\theta), \qquad (3.1) \\
\frac{d\,\psi}{d\,t} &= L\cos\theta(\frac{1}{C} - \frac{\sin^2\psi}{A} - \frac{\cos^2\psi}{B}) + \frac{M_\xi\cos\psi - M_\eta\sin\psi}{L\sin\theta}, \\
\frac{d\rho}{d\,t} &= \frac{M_x}{L}, \qquad \frac{d\sigma}{d\,t} = \frac{M_y}{L\sin\rho}, \qquad \frac{dL}{d\,t} = M_z,
\end{aligned}$$

where (M_x, M_y, M_z) and (M_ξ, M_η, M_ζ) are the components of the torque with respect to the angular momentum and the body-fixed systems. Note that these equations are singular for $\theta = 0, \pi$ and $\rho = 0, \pi$, and thus we cannot use them to integrate for principal axis rotation around the maximum momentum of inertia. However we can change coordinate system between the angular momentum system and the body fixed one, using Euler I angles instead of Euler II. With these coordinates the equations are singular for $\theta' = \pm\pi/2$, and the following discussion about the averaged dynamics follows in exactly the same way.

Another important equation is the one for the so called dynamic inertia

$$I_D = \frac{L^2}{2T} = \left(\frac{\sin^2\theta \sin^2\psi}{A} + \frac{\sin^2\theta \cos^2\psi}{B} + \frac{\cos^2\theta}{C} \right)^{-1}, \tag{3.2}$$

$$\frac{d\, I_D}{d\, t} = -\frac{2 I_D}{L} \left[\frac{(I_D - A)}{A} a_{z\,\xi} M_\xi + \frac{(I_D - B)}{B} a_{z\,\eta} M_\eta + \frac{(I_D - C)}{C} a_{z\,\zeta} M_\zeta \right],$$

where T is the rotational kinetic energy. Note that I_D is constant in the unperturbed motion. If $A < I_D < B$ we say that the body is in Long Axis Mode (LAM) rotation as the angular velocity revolves about the axis of minimum inertia, if $B < I_D < C$ we say that it is in Short Axis Model (SAM) rotation, as the angular velocity revolves about the axis of maximum moment of inertia. When $I_D = A, C$ the body is in principal axis rotation around the axes ξ and ζ. In general, we say that the body is in LAM_+ or LAM_- if the rotation axis is closer to the axis ξ in the positive or negative direction. In an analogous way we say that it is in a SAM_+ or SAM_- if the rotation axis is closer to the axis ζ in the positive or negative direction.

When $I_D = B$ the body is in principal axis rotation around the η-axis or its angular velocity moves along a heteroclinic connection between rotations about the η-axis in opposite directions. I_D is an important parameter because it tells us how the body is in intermediate principal axis rotation.

3.2.4 The YORP torque

We first consider a continuous model for the rigid body. Let $d\mathbf{S} = dS\,\mathbf{n}$ be the normal to a surface element of the body, and let $\mathbf{r}$ be its position with respect to the center of mass.

We assume in this first discussion that the body has zero thermal conductivity, which means that the infrared thermal emission takes place immediately after the solar photons have hit the body's surface. We also assume that the body is moving on a Keplerian orbit around the Sun, with semimajor axis a, eccentricity e and orbital period T_{orb}. Thus we can model the thermal YORP torque, due to the thermal radiation force normal to the body's surface, by the formula ([Rubincam 2000]):

$$\mathbf{M} = P(R)\, a_2 \oint f\, dS\, \mathbf{d} \tag{3.3}$$

where $a_2 = 2/3\,(1 - p_v)$ and p_v is the albedo of the body, f is the illumination function that is equal to 0 when the surface element is not illuminated by the Sun, and it is equal to $\mathbf{n} \cdot \mathbf{u}$ when it is, $\mathbf{u}$ is the position of the Sun in the body fixed system,

$$\mathbf{d} = \mathbf{n} \times \mathbf{r}$$

and

$$P(R) = \frac{G_1}{a^2(1-e^2)^2}(1 + e\cos\nu)^2$$

where $G_1 \cong 7.5 \times 10^{23}$ kg km/d^2 (see [Scheeres 2007]) is such that $P(R) = G_1/R^2$ is the solar radiation pressure at R km from the Sun. Finally ν is the true anomaly.

The strongest limitation of this analytical approach is modelling the illumination function f. If we do not take into account possible "self-shadowing" of the body, which means that the Sun is not illuminating a portion of the surface even if it is above its horizon (e.g. for a "banana-shape" asteroid), we can express the illumination function f analytically by:

$$f = \frac{1}{2}(|\mathbf{n} \cdot \mathbf{u}| + \mathbf{n} \cdot \mathbf{u}). \tag{3.4}$$

So a first approximation of this model is to not consider "self-shadowing" bodies. Putting $\mathbf{n} \cdot \mathbf{u} = \cos z$, we can express f by its Fourier series expansion:

$$f(z) = \frac{1}{2}(|\cos z| + \cos z) = \frac{a_0}{2} + \sum_{n=1}^{\infty} a_n \cos nz$$

$$a_n = \frac{1}{\pi}\int_{-\pi}^{\pi} f(z)\cos nz\; dz.$$

Truncating the series to its fourth order term we have:

$$\begin{aligned} f &= \frac{1}{\pi} + \frac{1}{2}\cos z + \frac{2}{3\pi}\cos 2z - \frac{2}{15\pi}\cos 4z + ... && (3.5)\\ &= \frac{1}{5\pi} + \frac{1}{2}(\mathbf{n}\cdot\mathbf{u}) + \frac{12}{5\pi}(\mathbf{n}\cdot\mathbf{u})^2 - \frac{16}{15\pi}(\mathbf{n}\cdot\mathbf{u})^4 + ... && (3.6)\end{aligned}$$

To simplify the analytical results we approximate f by using its second order expansion (following [Mysen 2008]):

$$\begin{aligned} f &= \frac{1}{\pi} + \frac{1}{2}\cos z + \frac{2}{3\pi}\cos 2z + ... && (3.7)\\ &= \frac{1}{3\pi} + \frac{1}{2}(\mathbf{n}\cdot\mathbf{u}) + \frac{4}{3\pi}(\mathbf{n}\cdot\mathbf{u})^2 + ... && (3.8)\end{aligned}$$

However, it is not obvious how much the higher order terms or the effect of self-shadowing will modify the dynamics, and how strong this effect could be for arbitrary shapes. It is then possible that this approximation is not accurate enough, and that we will need

to consider additional terms of the Fourier series in the future. We will come back to this problem later, when we discuss some generalizations. We also notice that, from elementary calculus theory, for a generic regular shape we have the following result (see for example [Mysen 2007]):

$$\oint dS\mathbf{d} = 0,$$

then the constant term in the Fourier series approximation of f does not contribute to the thermal YORP torque $\mathbf{M}$ given by formula (3.3).

Since we also would like to perform some numerical experiments, it is more convenient to model the shape of the rigid body in a discrete way, considering that its surface is formed by N triangular facets. Let A_i be the area of the i-th facet, $\mathbf{r}_i$ the position of the facet's center with respect to the center of mass of the body, and $\mathbf{n}_i$ the unit vector normal to the facet (Fig. 3.2).

Then we have the discrete formula for the thermal YORP, without thermal conductivity:

$$\mathbf{M} = P(R)\, a_2 \sum_i^N f_i\, A_i\, \mathbf{d}_i$$

where in this case

$$f_i = \frac{1}{3\pi} + \frac{1}{2}(\mathbf{n}_i \cdot \mathbf{u}) + \frac{4}{3\pi}(\mathbf{n}_i \cdot \mathbf{u})^2$$

and

$$\mathbf{d}_i = \mathbf{n}_i \times \mathbf{r}_i.$$

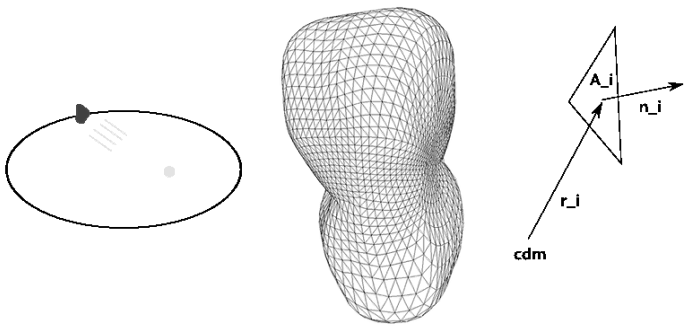

Figure 3.2: A simple cartoon showing an asteroid orbiting around the Sun and hit by the solar photons, and a discrete shape model obtained by a triangulation of the body's surface.

Notice that while the torque can be directly integrated over a single facet for a given obliquity (see [Scheeres 2007]) the resulting formula cannot be subsequently averaged, or at least not easily. The Mysen approximation in (3.7) makes the resultant torque amenable to further averaging and enables our current result.

3.2.5 Dissipation of Energy

For completeness, in this subsection we set up the equations of the rotational dynamics with a small dissipation of energy. If we do not assume a perfect rigid body model, we have to consider energy dissipation. Frictional internal processes tend to dissipate energy of the fluctuating strain field in the body. The fluctuating strain energy is nonzero when the body is in non-principal axis rotation as the rotational acceleration is time varying in the body-fixed frame.

We can model this effect by adding the following torque to the equations of motion, where we discriminate between SAM and LAM rotation states (see [Vokrouhlicky et al. 2007]):

SAM case

$$\mathbf{M}_d = \mp \frac{\varrho a_{eq}^2}{\mu Q C^3} L^3 \sin\theta (b_0 + b_2 \cos^2\theta) \mathbf{L} \times \left(\frac{\mathbf{L} \times \hat{\zeta}}{L \sin\theta} \right) \tag{3.9}$$

where ϱ is the bulk density, μ is the rigidity, Q the quality factor, a_{eq} the (averaged) equatorial radius, and b_0, b_2 are the same known constants given in [Vokrouhlicky et al. 2007]. The sign $-$ is in the SAM_+ case, the sign $+$ is in the SAM_- case.

LAM case

$$\mathbf{M}_d = \pm \frac{\varrho a_{eq}^2}{\mu Q A^3} L^3 \sin\theta' (b_0 + b_2 \cos^2\theta') \mathbf{L} \times \left(\frac{\mathbf{L} \times \hat{\xi}}{L \sin\theta'} \right) \tag{3.10}$$

where θ' is the angle between $\mathbf{L}$ and $\hat{\xi}$. The sign $+$ in in the LAM_+ case, the sign $-$ is in the LAM_- case.

Values for the physical parameters can be (e.g. in [Sharma et al. 2005]):

$$\varrho = 2.5\, g/cm^3 \qquad \mu Q = 5 \times 10^{12}\, g/cm\, s^2.$$

3.3 Analytical formulas for the secular solution

Since the torque $\mathbf{M}$ can be considered a "small torque" with respect to the angular momentum, we can apply a first order perturbation, averaged theory as described in [Arnold et al. 1998], where a tool is introduced for the long term averaged analysis of a certain kind of dynamical system. This is the so called "averaging principle", and, although it is not considered to rigorously be a theorem, we will use this approach as it

is commonly used commonly used to compute long-periodicand secular variations. Following closely the notation of [Arnold et al. 1998], we indicate with I the quantities ρ, σ, L and I_D, which are constants in the unperturbed rotational motion (*slow variables* in the perturbed motion), and with φ the coordinates on the 3-dimensional torus $\mathbf{T}^3$ parameterizing the unperturbed periodic Euler-Poinsot rotational motion (2 independent nonzero frequencies) and the Keplerian orbital motion (1 frequency) (*fast variables*).

The general formulas for this problem are then of the form

$$\dot{I} = 0 \qquad \dot{\varphi} = \omega(I)$$

for the unperturbed Euler-Poinsot rotational motion and the Keplerian orbital motion, while they are

$$\dot{I} = \epsilon f(I, \varphi, \epsilon) \qquad \dot{\varphi} = \omega(I) + \epsilon g(I, \varphi, \epsilon)$$

for the perturbed rotational motion in the small parameter ϵ, ratio of the YORP torque and the angular momentum. Then, we can average over the unperturbed Euler-Poinsot motion and over the Keplerian orbital motion through the angles φ by using the following formula (averaging principle):

$$\dot{\bar{I}} = \epsilon F(\bar{I}) \qquad F(\bar{I}) = (2\pi)^{-3} \oint_{\mathbf{T}^3} f(\bar{I}, \varphi, 0) d\,\varphi$$

where $\bar{I}$ indicates the first order averaged quantities $\bar{\rho}$, $\bar{\sigma}$, $\bar{L}$ and $\bar{I}_D$.

Not being the "averaging principle" a theorem, in general it is untrue that the difference between the true solution and the averaged solution consists in only short periodic oscillations. However, short periodic terms are present and are used in this paper (Sect. 5) just to indicate how much the solution will vary in general, and not to reconstruct the true solution. We believe that studying the level of variation that solutions can have relative to their average values, we can still reach some interesting conclusions on the behavior of the solution.

In the following, in order to obtain the secular evolutionary equations, we compute the first order averaged equations for the slow variables I of the system, constants in the Euler-Poinsot motion. Then we verify the agreement with the full solution obtained from system (3.1) over short time spans. In the next sections we study the averaged solution $\bar{I}$ over long time spans, with the intent to capture the generic evolution of the dynamical system.

According to the previous section 2, not considering the dissipation of energy, in order to compute the averaged equations for the quantities ρ, σ, L and I_D we can write

the YORP torque in the angular momentum frame as:

$$\begin{aligned} M_x &= P(R)\frac{a_2}{2}\oint dS d_x(\mathbf{n}\cdot\mathbf{u}) + P(R)\frac{4a_2}{3\pi}\oint dS d_x(\mathbf{n}\cdot\mathbf{u})^2, \\ M_y &= P(R)\frac{a_2}{2}\oint dS d_y(\mathbf{n}\cdot\mathbf{u}) + P(R)\frac{4a_2}{3\pi}\oint dS d_y(\mathbf{n}\cdot\mathbf{u})^2, \\ M_z &= P(R)\frac{a_2}{2}\oint dS d_z(\mathbf{n}\cdot\mathbf{u}) + P(R)\frac{4a_2}{3\pi}\oint dS d_z(\mathbf{n}\cdot\mathbf{u})^2, \end{aligned}$$

where $(\mathbf{n}\cdot\mathbf{u}) = u_x n_x + u_y n_y + u_z n_z$,

$$(\mathbf{n}\cdot\mathbf{u})^2 = u_x^2 n_x^2 + u_y^2 n_y^2 + u_z^2 n_z^2 + 2u_x u_y n_x n_y + 2u_x u_z n_x n_z + 2u_y u_z n_y n_z,$$

$$\begin{aligned} d_x &= a_{x\,\xi} d_\xi + a_{x\,\eta} d_\eta + a_{x\,\zeta} d_\zeta, & n_x &= a_{x\,\xi} n_\xi + a_{x\,\eta} n_\eta + a_{x\,\zeta} n_\zeta, \\ d_y &= a_{y\,\xi} d_\xi + a_{y\,\eta} d_\eta + a_{y\,\zeta} d_\zeta, & n_y &= a_{y\,\xi} n_\xi + a_{y\,\eta} n_\eta + a_{y\,\zeta} n_\zeta, \\ d_z &= a_{z\,\xi} d_\xi + a_{z\,\eta} d_\eta + a_{z\,\zeta} d_\zeta, & n_z &= a_{z\,\xi} n_\xi + a_{z\,\eta} n_\eta + a_{z\,\zeta} n_\zeta, \end{aligned}$$

$$u_x = -a_{x\,X}\sin\nu - a_{x\,Z}\cos\nu,\ u_y = -a_{y\,X}\sin\nu,\ u_z = -a_{z\,X}\sin\nu - a_{z\,Z}\cos\nu.$$

At this point we need to average M_x, M_y, M_z over the unperturbed rotational motion and over the orbit. Assuming no resonance between the rotational and the orbital motion, we can average separately over them. This computation is done following the same procedure of [Neishtadt et al. 2003], where such resonances are considered (in their section 3.6). We are not considering these resonances in this paper, and reserve their consideration to future work.

Indicating with $< \cdot >_o$ and $< \cdot >_e$ the averaged quantities over the orbital motion and the unperturbed rotational motion , we have the following results:

$$< P(R) >_o = \frac{1}{T}\int_0^T P(R)\,dt = \frac{(1-e^2)^{3/2}}{2\pi}\int_0^{2\pi}\frac{P(R(\nu))\,d\nu}{(1+e\cos\nu)^2} = \frac{G_1}{a^2\sqrt{(1-e^2)}},$$

$$< P(R)\sin\nu >_o = < P(R)\cos\nu >_o = < P(R)\sin\nu\cos\nu >_o = 0,$$

$$< P(R)\sin^2\nu >_o = < P(R)\cos^2\nu >_o = \frac{G_1}{2a^2\sqrt{(1-e^2)}},$$

and then

$$<< P(R)\oint dS\,\mathbf{d}\,(\mathbf{n}\cdot\mathbf{u}) >_e >_o = 0.$$

We still have to compute:

$$< a_{**} >_e; \quad < a_{**}a_{**} >_e; \quad < a_{**}a_{**}a_{**} >_e\ .$$

To compute these we will assume that there is no resonance between the unperturbed periodic motion of the angles ϕ and ψ, θ (see again [Neishtadt et al. 2003] section 3.6). Noting that the period of the angle ψ is twice the period of θ, it is possible to average over the angle ϕ separately, dropping out the dependence on ϕ and expressing all the averaged

quantities in terms of the $z-$ components $< a_{z*} >_e$, $< a_{z*}a_{z*} >_e$ and $< a_{z*}a_{z*}a_{z*} >_e$ only.

However, the time dependence of the quantities a_{**} through the (unperturbed) angle ϕ is much more complicated than the one through the angles θ, ψ. Let's indicate with P_ϕ the period of the unperturbed angle ϕ, then we will use the following approximation to average over its motion:

$$< a_{**} >_\phi = \frac{1}{P_\phi} \int_0^{P_\phi} a_{**}(\phi(t))\, dt \cong \frac{1}{2\pi} \int_0^{2\pi} a_{**}(\phi)\, d\phi = a_{**}(\theta, \psi).$$

The time dependence through the angles θ, ψ instead is simpler and is based on the elliptic functions sn, cn, dn. Through them we can average over their motion using an integral over time:

$$< a_{**} >_e = \frac{1}{P_{\theta\psi}} \int_0^{P_{\theta\psi}} a_{**}(\theta(t), \psi(t))\, dt$$

where $P_{\theta\psi}$ is the suitable period.

Notice that because the functions $\sin\phi$ and $\cos\phi$ average to zero we can conclude that the quantities $< a_{x*} >_e$ and $< a_{y*} >_e$ average to zero.

We also have to compute the products $< a_{**}a_{**}a_{**} >_e$ that appear in the term with $(\mathbf{n} \cdot \mathbf{u})^2$, where we have to compute the quantities $< d_* n_* n_* >$ with all the possible combinations. The functions $\sin^3\phi$, $\cos^3\phi$, $\sin^2\phi\cos\phi$, $\sin\phi\cos^2\phi$ all average to zero. Then, with the assumption of no resonance, the products $< a_{**}a_{**}a_{**} >_e$ involving only the $x-$ and $y-$ components and the products $< a_{x*}a_{z*}a_{z*} >_e$ and $< a_{y*}a_{z*}a_{z*} >_e$ are zero. The remaining terms that we have to compute are:

$$< a_{x*}a_{x*}a_{z*} >_e, \quad < a_{x*}a_{y*}a_{z*} >_e, \quad < a_{y*}a_{y*}a_{z*} >_e, \quad < a_{z*}a_{z*}a_{z*} >_e .$$

Using the notation $\overline{X}$ instead of $< X >$ when the meaning is clear, we have:

$$\overline{M}_* = << P(R) \frac{4a_2}{3\pi} \oint dS\, d_* \, (\mathbf{n} \cdot \mathbf{u})^2 >_e >_o$$

for $* = x, y, z$. A list with the computed averaged factors $< a_{**}a_{**}a_{**} >_e$ used in the following is given in the Appendix C.

3.3.1 Quantities averaged over the orbital motion

According to the first part of this section, the terms containing the true anomaly ν are averaged over one orbital period to yield:

$$\overline{P(R)} = \frac{G_1}{a^2\sqrt{(1-e^2)}}, \qquad \overline{P(R)u_x^2} = \frac{\overline{P(R)}}{2}(\cos^2\sigma\cos^2\rho + \sin^2\rho),$$

$$\overline{P(R)u_y^2} = \frac{\overline{P(R)}}{2}\sin^2\sigma, \qquad \overline{P(R)u_z^2} = \frac{\overline{P(R)}}{2}(\cos^2\sigma\sin^2\rho + \cos^2\rho), \tag{3.11}$$

$$\overline{P(R)u_x u_z} = -\frac{\overline{P(R)}}{2}\sin^2\sigma\sin\rho\cos\rho, \quad \overline{P(R)u_y u_z} = -\frac{\overline{P(R)}}{2}\sin\sigma\cos\sigma\sin\rho.$$

3.3.2 Factors averaged over the rotational motion

Putting together all the previous results, we obtain the following averaged factors over the unperturbed rotational motion:

In the SAM case:

$$\overline{d_z} = d_\zeta < a_{z\,\zeta} >_e, \tag{3.12}$$

$$\begin{aligned}\overline{d_z n_z^2} &= < a_{z\,\zeta}^3 >_e d_\zeta n_\zeta^2 + < a_{z\,\xi}^2 a_{z\,\zeta} >_e (2d_\xi n_\xi n_\zeta + d_\zeta n_\xi^2) + \\ &+ < a_{z\,\eta}^2 a_{z\,\zeta} >_e (2d_\eta n_\eta n_\zeta + d_\zeta n_\eta^2),\end{aligned}$$

$$\begin{aligned}\overline{d_x n_y n_z} &= \frac{1}{2}(< a_{z\,\zeta}^2 >_e - < a_{z\,\eta}^2 >_e) d_\xi n_\eta n_\zeta + \\ &+ \frac{1}{2}(< a_{z\,\xi}^2 >_e - < a_{z\,\zeta}^2 >_e) d_\eta n_\zeta n_\xi + \\ &+ \frac{1}{2}(< a_{z\,\eta}^2 >_e - < a_{z\,\xi}^2 >_e) d_\zeta n_\xi n_\eta.\end{aligned}$$

In the LAM case:

$$\overline{d_z} = d_\xi < a_{z\,\xi} >_e, \tag{3.13}$$

$$\begin{aligned}\overline{d_z n_z^2} &= < a_{z\,\xi}^3 >_e d_\xi n_\xi^2 + < a_{z\,\xi} a_{z\,\zeta}^2 >_e (2d_\zeta n_\xi n_\zeta + d_\xi n_\zeta^2) + \\ &+ < a_{z\,\xi} a_{z\,\eta}^2 >_e (2d_\eta n_\eta n_\xi + d_\xi n_\eta^2),\end{aligned}$$

$$\begin{aligned}\overline{d_x n_y n_z} &= \frac{1}{2}(< a_{z\,\zeta}^2 >_e - < a_{z\,\eta}^2 >_e) d_\xi n_\eta n_\zeta + \\ &+ \frac{1}{2}(< a_{z\,\xi}^2 >_e - < a_{z\,\zeta}^2 >_e) d_\eta n_\zeta n_\xi + \\ &+ \frac{1}{2}(< a_{z\,\eta}^2 >_e - < a_{z\,\xi}^2 >_e) d_\zeta n_\xi n_\eta.\end{aligned}$$

In both cases:

$$\overline{d_x n_x n_z} = -\frac{1}{2}\overline{d_z n_z^2}, \quad \overline{d_z n_x^2} = \frac{1}{2}(\overline{d_z} - \overline{d_z n_z^2}), \quad \overline{d_z n_y^2} = \overline{d_z n_x^2}, \tag{3.14}$$

$$\overline{d_y n_y n_z} = \overline{d_x n_x n_z}, \quad \overline{d_y n_x n_z} = -\overline{d_x n_y n_z}, \quad \overline{d_z n_x n_y} = 0.$$

3.3.3 Averaged equations

Using the previous formulas and notation, we can write the averaged equations for the angular momentum vector and the dynamic inertia as:

$$\frac{d\bar{\rho}}{dt} = \frac{\overline{M}_x}{\bar{L}}, \qquad \frac{d\bar{\sigma}}{dt} = \frac{\overline{M}_y}{\bar{L}\sin\bar{\rho}}, \qquad \frac{d\bar{L}}{dt} = \overline{M}_z, \tag{3.15}$$

$$\frac{d\,\bar{I}_D}{dt} = -\frac{2\bar{I}_D}{\bar{L}}\left[\frac{(\bar{I}_D - A)}{A}\overline{a_{z\,\xi}M_\xi} + \frac{(\bar{I}_D - B)}{B}\overline{a_{z\,\eta}M_\eta} + \frac{(\bar{I}_D - C)}{C}\overline{a_{z\,\zeta}M_\zeta}\right],$$

where

$$\overline{M}_x = \frac{8a_2}{3\pi}\left[\overline{P(R)u_x u_z}\oint dS\overline{d_x n_x n_z} + \overline{P(R)u_y u_z}\oint dS\overline{d_x n_y n_z}\right] =$$

$$= \frac{4a_2\overline{P(R)}}{3\pi}\left[\frac{1}{2}\sin^2\bar{\sigma}\sin\bar{\rho}\cos\bar{\rho}\oint dS\overline{d_z n_z^2} - \sin\bar{\sigma}\cos\bar{\sigma}\sin\bar{\rho}\oint dS\overline{d_x n_y n_z}\right],$$

$$\overline{M}_y = \frac{8a_2}{3\pi}\left[\overline{P(R)u_x u_z}\oint dS\overline{d_y n_x n_z} + \overline{P(R)u_y u_z}\oint dS\overline{d_y n_y n_z}\right] =$$

$$= \frac{4a_2\overline{P(R)}}{3\pi}\left[\frac{1}{2}\sin\bar{\sigma}\cos\bar{\sigma}\sin\bar{\rho}\oint dS\overline{d_z n_z^2} + \sin^2\bar{\sigma}\sin\bar{\rho}\cos\bar{\rho}\oint dS\overline{d_x n_y n_z}\right],$$

$$\overline{M}_z = \frac{4a_2}{3\pi}\left[\overline{P(R)u_x^2}\oint dS\overline{d_z n_x^2} + \overline{P(R)u_y^2}\oint dS\overline{d_z n_y^2} + \overline{P(R)u_z^2}\oint dS\overline{d_z n_z^2}\right] =$$

$$= \frac{2a_2\overline{P(R)}}{3\pi}\left(\frac{1}{2} - \frac{3}{2}\sin^2\bar{\rho}\sin^2\bar{\sigma}\right)\oint dS\overline{d_z n_z^2},$$

and

$$\overline{a_{z\,*}M_*} = \frac{4a_2}{3\pi}\left[\overline{P(R)u_x^2}\oint dS\overline{a_{z\,*}d_* n_x^2} + \overline{P(R)u_y^2}\oint dS\overline{a_{z\,*}d_* n_y^2} + \overline{P(R)u_z^2}\oint dS\overline{a_{z\,*}d_* n_z^2}\right] =$$

$$= \frac{2a_2\overline{P(R)}}{3\pi}\left(\frac{1}{2} - \frac{3}{2}\sin^2\bar{\rho}\sin^2\bar{\sigma}\right)\oint dS\overline{a_{z\,*}d_* n_z^2},$$

where $* = \xi, \eta, \zeta$, and for example $\overline{a_{z\,\xi}d_\xi n_x^2}$ is obtained from $\overline{d_z n_x^2}$ keeping only the terms containing $a_{z\,\xi}$ and d_ξ.

3.3.4 The obliquity

In order to simplify the discussion we introduce the most important quantity that describes the direction of the angular momentum vector in the inertial space: the obliquity $\delta \in [0, \pi]$, which is the angle between the normal to the orbit $\mathbf{Y}$ and the angular momentum $\mathbf{L}$.

This angle is related to the angles ρ and σ by the equation:

$$\cos\delta = \sin\rho\sin\sigma \tag{3.16}$$

and its dynamics is given by the differential equation:

$$\dot{\delta} = -\frac{1}{\sin\delta}\left(\frac{M_x}{L}\cos\rho\sin\sigma + \frac{M_y}{L}\cos\sigma\right).$$

In order to describe the secular dynamics of the obliquity, as we have done for the angles ρ and σ, we derive the first order averaged equation for δ:

$$\dot{\bar{\delta}} = -\frac{1}{\sin\bar{\delta}}\left(\frac{\overline{M}_x}{\bar{L}}\cos\bar{\rho}\sin\bar{\sigma} + \frac{\overline{M}_y}{\bar{L}}\cos\bar{\sigma}\right)$$

and after some computation:

$$\dot{\bar{\delta}} = -\frac{2a_2\overline{P(R)}}{3\pi\bar{L}}\sin\bar{\delta}\cos\bar{\delta}\oint dS\overline{d_z n_z^2}. \tag{3.17}$$

We have reduced the dynamical system to the three fundamental quantities $\bar{\delta}$, $\bar{L}$ and $\bar{I}_D$. It is easy to see that, if we define the following quantities

$$\mathcal{D}_1 = \mathcal{D}_1^{\pm}(\bar{I}_D) = \oint dS\overline{d_z n_z^2}, \tag{3.18}$$

$$\mathcal{D}_3 = \mathcal{D}_3^{\pm}(\bar{I}_D) = \tag{3.19}$$

$$= \frac{\bar{I}_D - A}{A}\oint dS\overline{a_{z\,\xi}d_\xi n_z^2} + \frac{\bar{I}_D - B}{B}\oint dS\overline{a_{z\,\eta}d_\eta n_z^2} + \frac{\bar{I}_D - C}{C}\oint dS\overline{a_{z\,\zeta}d_\zeta n_z^2},$$

where the sign $\pm$ depends on the mode $SAM/LAM_{\pm}$, we can write the dynamical system in the simple form:

$$\begin{cases} \dot{\bar{I}}_D &= -\frac{a_2\overline{P(R)}}{3\pi}\frac{2\bar{I}_D}{\bar{L}}(1-3\cos^2\bar{\delta})\mathcal{D}_3 \\ \dot{\bar{\delta}} &= -\frac{2a_2}{3\pi}\frac{\overline{P(R)}}{\bar{L}}\sin\bar{\delta}\cos\bar{\delta}\,\mathcal{D}_1 \\ \dot{\bar{L}} &= \frac{a_2\overline{P(R)}}{3\pi}(1-3\cos^2\bar{\delta})\mathcal{D}_1. \end{cases} \tag{3.20}$$

The secular evolution of these quantities is governed by the qualitative behavior of the functions $\mathcal{D}_1$ and $\mathcal{D}_3$. These functions depend on the parameter $\bar{I}_D$ through formulas (3.12)-(3.13) and the averaged factors in Appendix C, and are regular functions in the open intervals (A, B) and (B, C). They have the dimension of a volume. We note that it can be shown that $\mathcal{D}_1 = 0$ for a triaxial ellipsoid shape (see for example [Mysen 2007]). More details about the zeros of these functions will be given in the following.

3.3.5 Separation of variables and limitations

Both the differential equations for $\bar{I}_D$ and $\bar{\delta}$ in the system (3.20) have the same dependence on $\bar{L}$ as a factor $1/\bar{L}$. In particular the bigger $\bar{L}$ is the slower the variation of $\bar{I}_D$ and $\bar{\delta}$ is. Moreover, in all three equations we can separate the variables, yielding an integrable system for the averaged equations. Specifically, if we consider motion in the plane $(\bar{I}_D, \bar{\delta})$, we can always find a (local) first integral.

More precisely, if $\bar{I}_D = x$ and $\bar{\delta} = y$, the first integral is:

$$F(x,y) = e^{\frac{1}{6}\int_{x_0}^{x} \frac{\mathcal{D}_1(x')}{x'\mathcal{D}_3(x')}dx' - \int_{y_0}^{y} \frac{1-3\cos^2 y'}{3\sin 2y'}dy'} \tag{3.21}$$

such that

$$\frac{d}{dt}F(x,y) = F_x(x,y)\dot{x} + F_y(x,y)\dot{y} = 0.$$

Using this result it is easy to describe the solution of the averaged system (see section 4).

It also follows easily from equations (3.20) that there is a direct relation between $\bar{L}$ and $\bar{\delta}$:

$$\frac{\dot{\bar{\delta}}}{\dot{\bar{L}}} = -\frac{2}{\bar{L}}\frac{\sin\bar{\delta}\cos\bar{\delta}}{1-3\cos^2\bar{\delta}} \quad \Rightarrow \quad \bar{L}^2 = K\,\sin^2\bar{\delta}\cos\bar{\delta}$$

where K is a constant which depends on the initial conditions [1].

However, we must notice here that the fact that this system has a first integral is a direct consequence of the separation of variables, which would not be true if we considered a better approximation for the illumination function f (formula (3.4)), such as the approximation in formula (3.5), or incorporated self-shadowing of the body. This is clearly a limitation of the current analytical approach. However, modelling the self-shadowing of the body analytically is difficult, and considering a better approximation of f involves the computation of many terms, perhaps too many for a compact description of the averaged equations. We are not considering these improvements to the model here, leaving this problem to be discussed in future works.

The possible qualitative evolution of this system is described in the next section, in which we only briefly discuss the generalizations mentioned above.

3.3.6 Averaged equations with dissipation of energy

For completeness, assuming that the dissipation torque is a small perturbation of the free rotational motion, we also obtain the first order averaged equations with dissipation of energy for the quantities $\bar{\rho}$, $\bar{\sigma}$, $\bar{L}$, $\bar{I}_D$ as in the case of the YORP torque.

[1] This formula has been derived by D. Vokrouhlicky (private discussion).

It turns out that $\bar{\rho}$, $\bar{\sigma}$ and $\bar{L}$ are not affected by the dissipation, instead for $\bar{I}_D$ we have:

$$\dot{\bar{I}}_D = -\frac{a_2\overline{P(R)}}{3\pi}\frac{2\bar{I}_D}{\bar{L}}(1-3\cos^2\bar{\delta})\mathcal{D}_3 + h_d(\bar{I}_D,\bar{L})$$

where, putting

$$\mathcal{D}_5 = \frac{\bar{I}_D - A}{A}c_1 + \frac{\bar{I}_D - B}{B}c_2 + \frac{\bar{I}_D - C}{C}c_3, \tag{3.22}$$

in the $SAM_\pm$ case we have:

$$h_d(\bar{I}_D,\bar{L}) = \pm 2\frac{\varrho a_{eq}^2}{\mu Q C^3}\bar{L}^3\bar{I}_D\mathcal{D}_5(\bar{I}_D), \tag{3.23}$$

$$c_1 = b_0 < a_{z\,\xi}^2 a_{z\,\zeta} > + b_2 < a_{z\,\xi}^2 a_{z\,\zeta}^3 >, \quad c_2 = b_0 < a_{z\,\eta}^2 a_{z\,\zeta} > + b_2 < a_{z\,\eta}^2 a_{z\,\zeta}^3 >,$$
$$c_3 = b_0(< a_{z\,\zeta}^3 > - < a_{z\,\zeta} >) + b_2(< a_{z\,\zeta}^5 > - < a_{z\,\zeta}^3 >),$$

and in the $LAM_\pm$ case:

$$h_d(\bar{I}_D,\bar{L}) = \mp 2\frac{\varrho a_{eq}^2}{\mu Q A^3}\bar{L}^3\bar{I}_D\mathcal{D}_5(\bar{I}_D), \tag{3.24}$$

$$c_1 = b_0(< a_{z\,\xi}^3 > - < a_{z\,\xi} >) + b_2(< a_{z\,\xi}^5 > - < a_{z\,\xi}^3 >),$$
$$c_2 = b_0 < a_{z\,\xi} a_{z\,\eta}^2 > + b_2 < a_{z\,\xi}^3 a_{z\,\eta}^2 >, \quad c_3 = b_0 < a_{z\,\xi} a_{z\,\zeta}^2 > + b_2 < a_{z\,\xi}^3 a_{z\,\zeta}^2 > .$$

It is straightforward to find that the sign of the quantity h_d does not depend on the sign of the mode. Indeed, looking at the formulas for the averaged factors in Appendix C, we see that the sign of the quantities c_i changes if the sign of the mode changes, and so does the sign in front of the formula for h_d.

Intuitively, the averaged effect of the energy dissipation on the rotation would be to drive the body to principal axis SAM, so to drive $\bar{I}_D$ to the value C. Thus we expect h_d to be always positive, which means $\mathcal{D}_5 > 0$ in the SAM_+ mode and $\mathcal{D}_5 < 0$ in the LAM_+ mode. Proving that analytically is not straightforward, but this is the case for all the shape models that we have tested (see section 6).

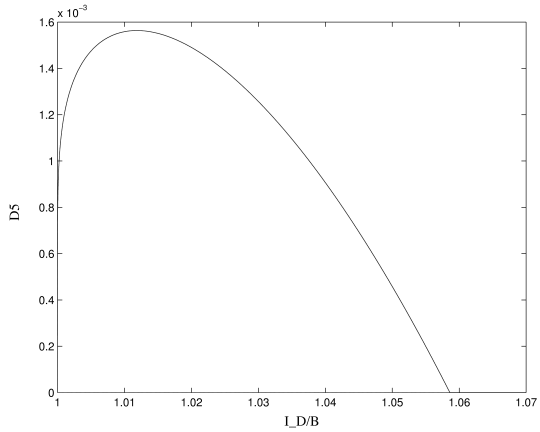

Figure 3.3: The $\mathcal{D}_5$ function in the SAM_+ mode. We used the asteroid *Toutatis* shape model (see section 6.2 for more details about the model).

3.3.7 Comparison between full and averaged solution

For example purposes we present some direct comparisons between numerical integrations and secular integration of the averaged equations. The full numerical integration consists of the implementation of the full dynamical system (3.1), while the secular integration consists of the separate implementation of the dynamical system (3.20) obtained by analytical averaging of (3.1).

To test the agreement between the full solution and the averaged solution we integrated both the equations using the asteroid *Toutatis* shape model, see section 6.2 for more details about the model, on a time span of $\Delta t \cong 20\, T_{orb}$ with the following initial conditions (randomly chosen):

$$\theta_0 = 30^\circ, \quad \phi_0 = 1^\circ, \quad \psi_0 = 50^\circ, \quad (\Rightarrow I_{D0} \cong 1.36 \times 10^{13}\text{kg km}^2), \tag{3.25}$$

$$\rho_0 = 40^\circ, \quad \sigma_0 = 90^\circ \quad (\Rightarrow \delta_0 \cong 101.6^\circ), \quad L_0 = 1.08 \times 10^{13}\text{kg km}^2/\text{d}.$$

We recall that the obliquity is related to ρ and σ by $\cos\delta = \sin\rho \sin\sigma$.

The numerical integrator we use is the Matlab *Ode*45. The error control used is a *RelTol* of 10^{-12} and an *AbsTol* of 10^{-12}.

Note the good agreement between the two over short time spans (Figs. 3.4, 3.5), which already are very computationally challenging for the full simulations. Based on a number of such comparisons we conclude that the secular equations properly represent the averaged motion.

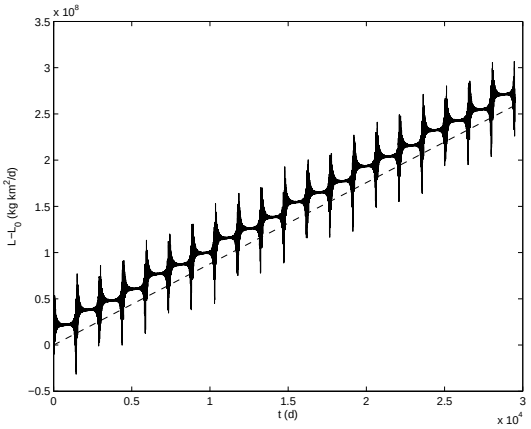

Figure 3.4: Comparison between the full solution (solid curve) and the averaged solution (dashed line) for the angular momentum magnitude $L - L_0$ (initial conditions (3.25)), plotted over a $\Delta t \cong 20 T_{orb}$ time span.

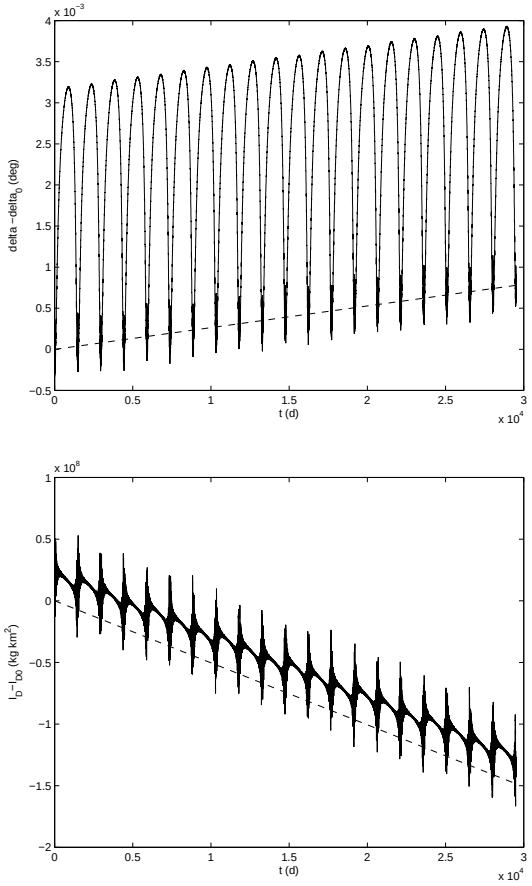

Figure 3.5: Comparison between the full solution (solid curve) and the averaged solution (dashed line), on the top the obliquity $\delta - \delta_0$, on the bottom the dynamic inertia $I_D - I_{D0}$ (initial conditions (3.25)), both plotted over a $\Delta t \cong 20 T_{orb}$ time span.

3.4 Dynamics without dissipation

We have seen that the principal quantities that describe the averaged behavior of the rotational dynamics are the obliquity of the angular momentum, its magnitude, and the dynamic inertia parameter $\bar{I}_D$.

In the previous section we found that

$$\dot{\bar{I}}_D = h(\bar{I}_D, \bar{\delta}, \bar{L}), \qquad \dot{\bar{\delta}} = f(\bar{I}_D, \bar{\delta}, \bar{L}), \qquad \dot{\bar{L}} = g(\bar{I}_D, \bar{\delta}),$$

and that we can easily separate the variables. Thus it is possible to draw, at least qualitatively, the level curves $\dot{\bar{I}}_D = 0$, $\dot{\bar{\delta}} = 0$ and $\dot{\bar{L}} = 0$ in the plane $(\bar{I}_D, \bar{\delta})$. These curves, because of the separation of the variables, are straight lines, independent of the sign of the mode $SAM/LAM\pm$. Instead the parts of the plane in which $\dot{\bar{\delta}}$, $\dot{\bar{I}}_D$ and $\dot{\bar{L}}$ are positive or negative depend on the sign $\pm$ of the mode $SAM/LAM\pm$, through the functions $\mathcal{D}_k^{\pm}(\bar{I}_D)$.

If we know the rotation mode of the body, we can choose the sign $\pm$ of the functions $\mathcal{D}_k = \mathcal{D}_k^{\pm}(\bar{I}_D)$ (note that $\mathcal{D}_k^- = -\mathcal{D}_k^+$). Once the sign and the mode are set we can study the properties of these functions. In particular in the SAM case we have to study $\mathcal{D}_k$ for $\bar{I}_D \in (B, C)$, in the LAM case we have to study $\mathcal{D}_k$ for $\bar{I}_D \in (A, B)$.

This information, together with the level curves of the first integral of the system, gives us the *Phase diagram* structure, i.e. the parts of the plane $(\bar{I}_D, \bar{\delta})$ in which the quantities $\dot{\bar{\delta}}$, $\dot{\bar{I}}_D$, $\dot{\bar{L}}$ are positive or negative and the qualitative behavior of the solutions.

In order to qualitatively describe the dynamics, we will look for the stationary points of $\bar{\delta}$, $\bar{L}$ and $\bar{I}_D$.

Def. Let $\bar{x}$ be one of the quantities $\bar{I}_D$, $\bar{\delta}$, $\bar{L}$.

We define an *equilibrium point* for $\bar{x}$ a configuration of the body at a time t_0 such that

- $\dot{\bar{x}}(t) = 0 \quad \forall t \geq t_0$.

We define a *stationary point* for $\bar{x}$ a configuration of the body at a time t_s such that

- $\dot{\bar{x}}(t_s) = 0$.

3.4.1 Equilibrium points for the obliquity

The behavior of the obliquity $\bar{\delta}$ is described by the differential equation:

$$\dot{\bar{\delta}} = -\alpha \sin\bar{\delta} \cos\bar{\delta}\ \mathcal{D}_1,$$

where $\alpha = 2a_2\overline{P(R)}/3\pi\bar{L} > 0$. Then we deduce that $\dot{\bar{\delta}} = 0$ if and only if:

- $\bar{\delta} = \pi/2$, i.e. $\mathbf{L}$ lies in the orbital plane

- $\bar{\delta} = 0$, $\bar{\delta} = \pi$, i.e. $\mathbf{L}$ is normal to the orbital plane
- there is an $\bar{I}_D^e$ such that $\mathcal{D}_1(\bar{I}_D^e) = 0$

In the first two cases $\dot{\bar{\delta}}$ is 0 whatever the value of $\bar{I}_D$, so the direction of the angular momentum remains fixed over time and we have three equilibrium points for $\bar{\delta}$.

In the third case note that $\lim_{I_D \to B} \mathcal{D}_1 = 0$ whatever the shape, but we will see that the case $\bar{I}_D = B$ is a critical case which has to be discussed separately. In principle $\mathcal{D}_1$ can have other zeros. But since in general $\bar{I}_D$ is changing over time, the direction cannot remain fixed and we can have only a stationary point for $\bar{\delta}$. In this case, if we want a fixed direction over time, i.e. an equilibrium point, we need also a condition on the variation of $\bar{I}_D$: for example a direction $\bar{\delta}_D^*$ such that $\dot{\bar{I}}_D(\bar{I}_D^e, \bar{\delta}_D^*) = 0$. We will come back to this point later.

Given the roots and the sign of the function $\mathcal{D}_1$, it is straightforward to find the parts of the plane $(\bar{I}_D, \bar{\delta})$ in which $\dot{\bar{\delta}}$ is positive or negative. The stability of the equilibrium points for $\bar{\delta}$ is given by the sign of the derivative of the function $\dot{\bar{\delta}} = f(\bar{I}_D, \bar{\delta}, \bar{L})$.

In the first case the equilibrium points are independent of the value of $\bar{I}_D$ (and $\bar{L}$), so what is important is the sign of the derivative respect to $\bar{\delta}$:

$$\frac{\partial f}{\partial \bar{\delta}} = -\frac{2a_2}{3\pi} \frac{\overline{P(R)}}{\bar{L}} \cos 2\bar{\delta}\ \mathcal{D}_1.$$

In the case $\bar{\delta} = \pi/2$ we have:

$$\frac{\partial f}{\partial \bar{\delta}} = \frac{2a_2}{3\pi} \frac{\overline{P(R)}}{\bar{L}}\ \mathcal{D}_1,$$

instead in the cases $\bar{\delta} = 0$ and $\bar{\delta} = \pi$ we have:

$$\frac{\partial f}{\partial \bar{\delta}} = -\frac{2a_2}{3\pi} \frac{\overline{P(R)}}{\bar{L}}\ \mathcal{D}_1.$$

The stability of these points at a given time depends on the sign of $\mathcal{D}_1$, through the shape, the value of $\bar{I}_D$ and the sign of the mode $SAM/LAM\pm$. In general, if $\bar{\delta} = \pi/2$ is stable then $\bar{\delta} = 0$ and $\bar{\delta} = \pi$ are unstable and viceversa.

The stability of the equilibrium points in the third case will be discussed in the following.

3.4.2 Equilibrium points for the dynamic inertia $\bar{I}_D$

We are looking for the solutions of the equation

$$\dot{\bar{I}}_D = -\alpha \bar{I}_D (1 - 3\cos^2 \bar{\delta}) \mathcal{D}_3 = 0.$$

We deduce that $\dot{\bar{I}}_D = 0$ if and only if:

- there is an $\bar{I}_D^d$ such that $\mathcal{D}_3(\bar{I}_D^d) = 0$, so $\dot{\bar{I}}_D = 0 \; \forall \bar{\delta}$
- $\cos^2 \bar{\delta} = \frac{1}{3}$

The first case is possible whatever the shape, for $\bar{I}_D^d = A$, $\bar{I}_D^d = C$ and also $\bar{I}_D^d = B$ because $\lim_{I_D \to B} \mathcal{D}_3 = 0$. So, if we are in principal axis rotation, $\dot{\bar{I}}_D = 0$ whatever the angular momentum obliquity and we have three equilibrium points for $\bar{I}_D$.

In principle, depending on the shape, it is possible to have other zeros of $\mathcal{D}_3$, where these are also equilibrium points for $\bar{I}_D$.

The second case is when $\bar{\delta}^* \cong 54.7°$ or $\bar{\delta}^* \cong 125.3°$. These can be equilibrium points for $\bar{I}_D$ only if they are also equilibrium points for $\bar{\delta}$. As we noticed in the previous section, this is possible if $\bar{I}_D \equiv \bar{I}_D^e$, with $\mathcal{D}_1(\bar{I}_D^e) = 0$. In this case we have an equilibrium point $(\bar{I}_D^e, \bar{\delta}^*)$ for both the direction and the dynamic inertia. Notice that these equilibrium points correspond to the asymptotic states for the obliquity and for the parameter $p = B/I_D$ found in [Vokrouhlicky et al. 2007]. The value of the obliquity asymptotic state does not depend on the shape and it is directly comparable with our result, while the exact value of the dynamic inertia asymptotic state depends sensitively on the shape through $\mathcal{D}_1$ and it can be qualitatively compared with the numerical examples in section 6 for the given shape models. For example, using the asteroid *Toutatis* shape model in the *LAM* case we find a value of $\bar{I}_D^e/B \cong 0.45$. In the next Figure 3.6 we show a numerical comparison between the full solution and the secular one at the equilibrium point $(\bar{I}_D^e, \bar{\delta}^*)$, as described in section 3.7.

Also in this case, once given the roots and the sign of the function $\mathcal{D}_3$, it is easy to find the parts of the plane $(\bar{I}_D, \bar{\delta})$ in which $\dot{\bar{I}}_D$ is positive or negative.

Stability of the equilibrium points for $\bar{I}_D$ and $\bar{\delta}$

The points $(\bar{I}_D^d, 0)$,$(\bar{I}_D^d, \pi)$ and $(\bar{I}_D^d, \pi/2)$ are equilibrium points for both $\bar{I}_D$ and $\bar{\delta}$. Their stability is given by the eigenvalues of the Jacobian matrix $J = \partial(h, f)/\partial(\bar{I}_D, \bar{\delta})$ computed in the equilibrium points:

$$J(\bar{I}_D^d, \pi/2) = \begin{pmatrix} -\alpha \bar{I}_D^d \mathcal{D}_3'(\bar{I}_D^d) & 0 \\ 0 & \alpha \bar{I}_D^d \mathcal{D}_1(\bar{I}_D^d) \end{pmatrix},$$

then $(\bar{I}_D^d, \pi/2)$ can be a saddle or a node, depending on the sign of $\mathcal{D}_3'(\bar{I}_D^d)$ and $\mathcal{D}_1(\bar{I}_D^d)$.

And:

$$J(\bar{I}_D^d, 0) = J(\bar{I}_D^d, \pi) = \begin{pmatrix} 2\alpha \bar{I}_D^d \mathcal{D}_3'(\bar{I}_D^d) & 0 \\ 0 & -\alpha \bar{I}_D^d \mathcal{D}_1(\bar{I}_D^d) \end{pmatrix},$$

then $(\bar{I}_D^d, 0)$ and $(\bar{I}_D^d, \pi)$ are both saddles or both nodes. In particular they are saddles if $(\bar{I}_D^d, \pi/2)$ is a saddle, and nodes if $(\bar{I}_D^d, \pi/2)$ is a node (with opposite stability). We found the same result in the case of principal axis rotation $\bar{I}_D \equiv C$ (example in [Scheeres & Mirrahimi 2008]), where the equilibrium points for the obliquity are $0, \pi$ and $\pi/2$ with opposite stability.

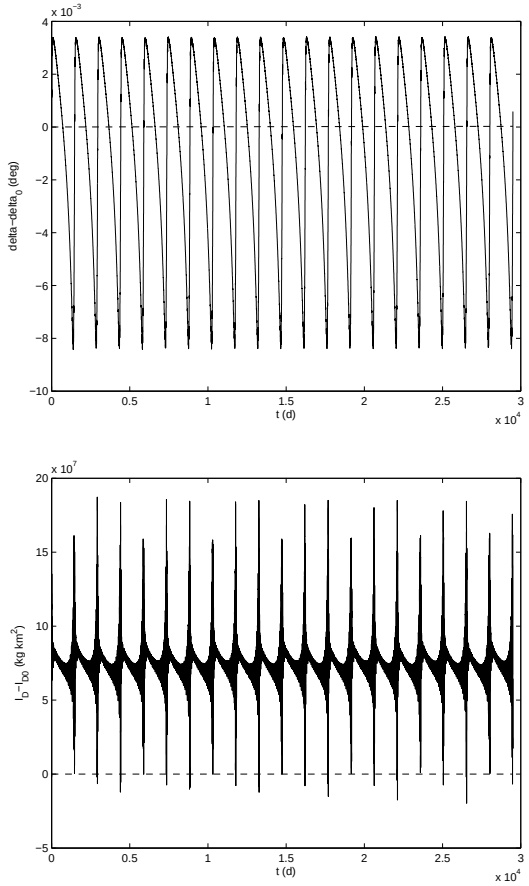

Figure 3.6: Comparison between the full solution (solid curve) and the averaged solution (dashed line), on the top the obliquity $\delta - \delta_0$, on the bottom the dynamic inertia $I_D - I_{D0}$ (initial conditions at the equilibrium $\delta_0 = \delta^* \cong 55°$, $I_{D0} = \bar{I}_D^e$), both plotted over a $\Delta t \cong 20 T_{orb}$ time span.

The point $(\bar{I}_D^e, \bar{\delta}_D^*)$ that we found above is also an equilibrium point for both $\bar{I}_D$ and $\bar{\delta}$. In this case:

$$J(\bar{I}_D^e, \bar{\delta}_D^*) = \begin{pmatrix} 0 & -3\alpha \bar{I}_D^e \sin 2\bar{\delta}^* \mathcal{D}_3(\bar{I}_D^e) \\ -\frac{\alpha}{2} \sin 2\bar{\delta}^* \mathcal{D}_1'(\bar{I}_D^e) & 0 \end{pmatrix}.$$

The eigenvalues of this matrix are:

$$\lambda_{1,2} = \pm \sqrt{\frac{16}{3} \alpha^2 \bar{I}_D^e \mathcal{D}_1'(\bar{I}_D^e) \mathcal{D}_3(\bar{I}_D^e)}.$$

Thus

- if $\mathcal{D}_1'(\bar{I}_D^e)\mathcal{D}_3(\bar{I}_D^e) > 0$ we have a hyperbolic point, in particular a saddle;
- if $\mathcal{D}_1'(\bar{I}_D^e)\mathcal{D}_3(\bar{I}_D^e) < 0$ we have a nonhyperbolic point, in particular a center;
- if $\mathcal{D}_1'(\bar{I}_D^e)\mathcal{D}_3(\bar{I}_D^e) = 0$ we have a nonhyperbolic point with two zero eigenvalues.

Notice that if $\mathcal{D}_1$ and $\mathcal{D}_3$ have only one root in the open interval (A, B) (or (B, C)), respectively $\bar{I}_D^e$ and $\bar{I}_D^d$, then the function $\mathcal{D}_1\mathcal{D}_3$ has exactly two roots, and the signs of $\mathcal{D}_1'(\bar{I}_D^e)\mathcal{D}_3(\bar{I}_D^e)$ and $\mathcal{D}_1(\bar{I}_D^d)\mathcal{D}_3'(\bar{I}_D^d)$ must be opposite. Thus if the equilibrium points $(\bar{I}_D^e, \bar{\delta}^*)$ are centers the equilibrium points $(\bar{I}_D^d, \bar{\delta})$ for $\bar{\delta} = 0, \pi/2, \pi$ are saddles.

A detailed analysis of the critical case $\mathcal{D}_1'(\bar{I}_D^e)\mathcal{D}_3(\bar{I}_D^e) = 0$ is beyond the scope of this work. We notice that if $\mathcal{D}_3(\bar{I}_D^e) = 0$, then the points $(\bar{I}_D^e, \bar{\delta})$ are all equilibrium points for both $\bar{I}_D$ and $\bar{\delta}$.

3.4.3 Equilibrium points for the angular momentum magnitude

The equilibrium and stationary points for $\bar{L}$ are given by the equation

$$\dot{\bar{L}} = \frac{a_2 \overline{P(R)}}{3\pi} (1 - 3\cos^2 \bar{\delta}) \mathcal{D}_1 = 0.$$

We deduce that $\dot{\bar{L}} = 0$ if and only if:

- there is an $\bar{I}_D^l$ such that $\mathcal{D}_1(\bar{I}_D^l) = 0$, so $\dot{\bar{L}} = 0 \; \forall \bar{\delta}$
- $\cos^2 \bar{\delta} = \frac{1}{3}$

In both cases, if $\bar{I}_D^l \neq B$, to be equilibrium points for $\bar{L}$ we need them to also be equilibrium points for $\bar{I}_D$ and $\bar{\delta}$. From the previous sections we know that these are the cases for $\bar{I}_D = \bar{I}_D^e$ with $\mathcal{D}_1(\bar{I}_D^e) = 0$, $\bar{\delta}^* = \arccos(1/\sqrt{3}) \cong 54.7°$ and $\bar{\delta}^* \cong 125.3°$. Figure 3.7 shows a numerical comparison between the full and the secular solutions for L, when the initial conditions are chosen at the equilibrium $(\bar{I}_D^e, \bar{\delta}^*)$ (see section 4.2). Notice that these correspond to the zero-torque obliquities found in [Nesvorny & Vokrouhlicky 2007]. The stability of these points has already been discussed, because it does not depend on the

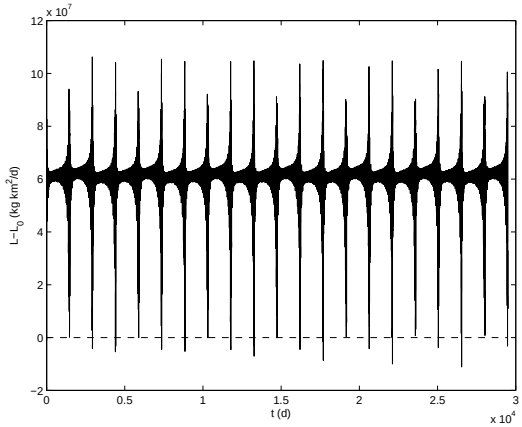

Figure 3.7: Comparison between the full solution (solid curve) and the averaged solution (dashed line) for the angular momentum $L - L_0$ (initial conditions at the equilibrium $\delta_0 = \delta^* \cong 55°$, $I_{D0} = \bar{I}_D^e$), plotted over a $\Delta t \cong 20 T_{orb}$ time span.

value of $\bar{L}$. The parts of the plane $(\bar{I}_D, \bar{\delta})$ in which $\dot{\bar{L}}$ is positive or negative are easily obtainable.

Note. We have seen that in the case of $\bar{I}_D = B$ we have always $\dot{\bar{\delta}} = \dot{\bar{L}} = \dot{\bar{I}}_D = 0$, then this is an equilibrium point for all the three fundamental quantities. However this is only true for the averaged equations, not for the full dynamical system. We will see that this is a critical situation which has to be treated separately (see the section 5 "Transition and chaotic behavior").

3.4.4 Generic examples of dynamics in the plane $(\bar{I}_D, \bar{\delta})$

Here we present two generic examples of the dynamics flow in the plane $(\bar{I}_D, \bar{\delta})$. In the first example we suppose that the functions $\mathcal{D}_1$ and $\mathcal{D}_3$ have exactly one root in the open interval (A, B) and one root in the open interval (B, C). We indicate with $\bar{I}_D^e$ the roots of $\mathcal{D}_1$ and with $\bar{I}_D^d$ the roots of $\mathcal{D}_3$ in the open intervals (A, B) and (B, C).

In the second example we suppose that $\mathcal{D}_1$ and $\mathcal{D}_3$ do not have roots in these intervals.

The structure of the orbits is obtained from the level curves of the first integral function F in formula (3.21). The direction of the orbits is given by the sign $\pm$ of the mode $SAM_\pm$ or $LAM_\pm$: changing it has the only effect of changing the direction of the motion. Since it is possible for the $\mathcal{D}_k$ functions to have roots in the LAM case and to have no roots in the SAM case, or viceversa, mixed phase diagrams are possible (see also section 6).

In the first example (Figure 3.8) we suppose that $\mathcal{D}_1'(\bar{I}_D^e)\mathcal{D}_3(\bar{I}_D^e) < 0$ for both the

zeros of $\mathcal{D}_1$ in (A, B) and in (B, C), i.e., non-hyperbolic equilibrium points. And we also suppose that the roots of $\mathcal{D}_3$ are closer to the value B with respect to the roots of $\mathcal{D}_1$.

In the second example (Figure 3.9) we suppose that $\mathcal{D}_1$ and $\mathcal{D}_3$ do not have roots in the open intervals (A, B) and (B, C). We suppose also that $\mathcal{D}_1(\bar{I}_D)\mathcal{D}_3'(\bar{I}_D) > 0$ for $\bar{I}_D = A, C$. The behavior of the orbits approaching the value $\bar{I}_D = B$ needs to be treated separately (see section 5).

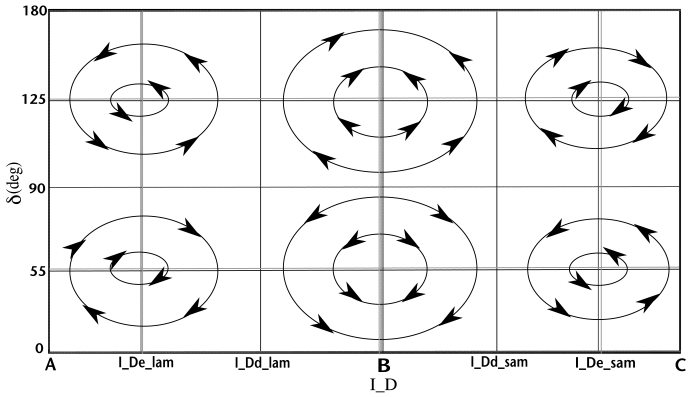

Figure 3.8: In the plane $(\bar{I}_D, \bar{\delta})$, the vertical lines at A, C and $\bar{I}_D^d$ are stationary points for $\bar{I}_D$, the ones at $\bar{I}_D^e$ are stationary points for $\bar{\delta}$ and $\bar{L}$. The horizontal lines at $\sim 55°$ and $\sim 125°$ are stationary points for $\bar{I}_D$ and $\bar{L}$, the ones at $0°$, $90°$ and $180°$ are stationary points for $\bar{\delta}$. The value B is a critical value (section 5). In this case the orbits are closed around the center equilibrium points $(\bar{I}_D^e, \bar{\delta}^* \sim 55°)$ and $(\bar{I}_D^e, \bar{\delta}^* \sim 125°)$. The points $(\bar{I}_D^d, 0)$,$(\bar{I}_D^d, \pi)$ and $(\bar{I}_D^d, \pi/2)$ are saddles.

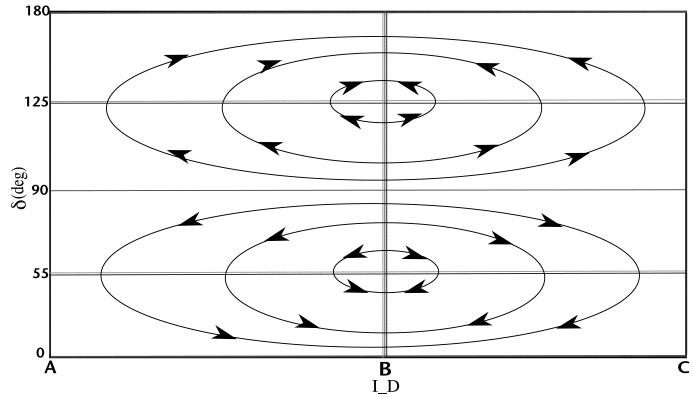

Figure 3.9: In the plane $(\bar{I}_D, \bar{\delta})$, the vertical lines at A and C are stationary points for $\bar{I}_D$. The horizontal lines at $\sim 55°$ and $\sim 125°$ are stationary points for $\bar{I}_D$ and $\bar{L}$, the ones at $0°$, $90°$ and $180°$ are stationary points for $\bar{\delta}$. The value B is a critical value (section 5). The equilibrium points $(\bar{I}_D, 0)$, $(\bar{I}_D, \pi)$ and $(\bar{I}_D, \pi/2)$ for $\bar{I}_D = A, C$ are saddles.

In principle other behaviors are possible, for example we can consider the case $\mathcal{D}_1'(\bar{I}_D^e)\mathcal{D}_3(\bar{I}_D^e) > 0$ for both the zeros of $\mathcal{D}_1$ in (A, B) and in (B, C), i.e., hyperbolic equilibrium points. Or cases in which the roots of $\mathcal{D}_1$ are closer to the value B with respect to the roots of $\mathcal{D}_3$. We could also consider hypothetical cases in which the function $\mathcal{D}_1$ has roots and the function $\mathcal{D}_3$ does not. However, the qualitative behaviors described in this section are the only ones that we found from all the asteroid shape models that we tested (see section 6).

Confronting the plot in Figure 3.8 with the corresponding ones in [Vokrouhlicky et al. 2007] we can notice that the former contains closed cycles with no way to tend towards the equilibrium point, while in the latters there are cases in which the solution tends asymptotically to the equilibrium. This is probably the principal difference between the present results and the numerical simulations of [Vokrouhlicky et al. 2007]. Possible reasons for these differences are discussed in the next subsection 4.5.

3.4.5 Generalizations

In section 2.4, while modelling the YORP torque, we pointed out two important generalizations that we made to the approximations:

- considering a better approximation of the illumination function f, up to higher order terms (e.g. to $(\mathbf{n} \cdot \mathbf{u})^4$), and considering the self-shadowing phenomena of the body;
- considering the dissipation of energy.

In section 3.5 we noticed that a better approximation of f involves the computation of a large number of terms, and we are not considering the possibility of doing this computation here. In the following we discuss qualitatively, and not rigorously, some possible consequences of these approximations.

The illumination function

Considering additional terms in the series development of the illumination function acts as a perturbation on the dynamics previously described:

$$\begin{cases} \dot{\bar{I}}_D &= h(\bar{I}_D, \bar{\delta}, \bar{L}) + \frac{1}{L}\epsilon_1(\bar{I}_D, \bar{\delta}) \\ \dot{\bar{\delta}} &= f(\bar{I}_D, \bar{\delta}, \bar{L}) + \frac{1}{L}\epsilon_2(\bar{I}_D, \bar{\delta}) \\ \dot{\bar{L}} &= g(\bar{I}_D, \bar{\delta}) + \epsilon_3(\bar{I}_D, \bar{\delta}). \end{cases}$$

However, it is not obvious how much the effect of such a perturbation would be for different shapes, it could be stronger for shapes with possible self-shadowing.

We can only conjecture that the dynamics does not change much in the case of the hyperbolic equilibrium points, because the linear part of the system should not be perturbed enough to change its kind.

Instead, in the case of the non-hyperbolic equilibrium points, we could expect them to become hyperbolic, and to have a deviation from the closed orbits (the ones along the first integral level curves), moving on a spiral toward the equilibrium points, or escaping from them (the center becomes a focus). A qualitative example of this effect is given in Figure 3.10.

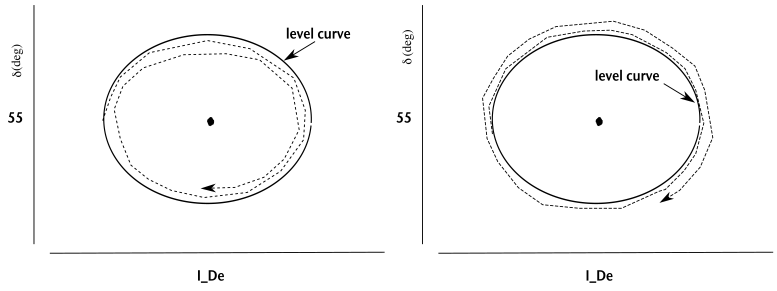

Figure 3.10: A qualitative example (conjectured) of the solution deviating from the level curve of the first integral. Going toward the equilibrium point (left), or escaping from it (right).

As we anticipated, the numerical simulations in [Vokrouhlicky et al. 2007] actually show asymptotic states and a more complex dynamics. Although the asymptotic states clearly correspond to the equilibrium points $(\bar{I}_D^e, \bar{\delta}^*)$ that we also found, in those simulations there seems to be no trace of the roots of the function $\mathcal{D}_3$. Moreover they found that when the solution is close to the asymptotic state the angular momentum magnitude rate $\dot{L}$ is constant. It is possible that these differences are due to the fact that they

also included gravitational torques due to the Sun and to the different model they used for the illumination function, which is more realistic in the numerical simulations and it can easily destroy the integrability of our simplified model. It is worth to notice that in [Statler 2009] it is shown, using full numerical simulations, the sensitivity of the YORP effect to small changes in the shape of the body.

A better model for f should be necessary to describe the averaged behavior of the rotational dynamics under the YORP torque in a more accurate way.

The dissipation of energy

The dissipation of energy, discussed in sections 2.5 and 3.6, involves the angular momentum magnitude as an important parameter. Indeed, if L is small the effect of the dissipation is small, and in this case we have a small perturbation of the dynamics with no dissipation. Again, the effect would not be important in the case of hyperbolic equilibrium points, while it could drive the motion toward the equilibrium points (on a spiral) in the case of the non-hyperbolic equilibrium points. An interesting result here is that, for moderate values of L, we may have non principal axis states as an asymptotic state even with energy dissipation. Instead, when L is large, dissipation tends to dominate the $YORP$ effect. In this case we would not have equilibrium points for $\bar{I}_D$ anymore, and the result will be that the motion tends to the principal SAM axis rotation ($\bar{I}_D \to C$).

3.5 Transition and chaotic behavior

In this section we describe qualitatively the behavior of the solution when it approaches the critical value $\bar{I}_D = B$.

Since the functions $\mathcal{D}_k^{\pm}(\bar{I}_D)$ change sign when we change the sign mode $\pm$, the phase diagram changes behavior after every transition $SAM \leftrightarrow LAM$, depending on which of the four following transitions happen:

$$SAM_+ \leftrightarrow LAM_+,\ SAM_+ \leftrightarrow LAM_-,\ SAM_- \leftrightarrow LAM_+,\ SAM_- \leftrightarrow LAM_-.$$

Note that these are the only possible transitions, since it is not possible to have a transition $SAM_+ \leftrightarrow SAM_-$ or $LAM_+ \leftrightarrow LAM_-$.

So, as long as the rotation state stays in the same mode, for a long enough time span to perform an averaged solution, then, starting from some initial conditions $(\bar{I}_{D0}, \bar{\delta}_0)$ it is possible to perform a qualitative study of the averaged solution $(\bar{I}_D(t), \bar{\delta}(t))$. This gives us information on the non-principal axis rotation, on the direction of the angular momentum, and also on the sign of $\dot{\bar{L}}(t)$, which gives us information on the acceleration or deceleration of the rotation state of the body.

However, what happens when we approach the transition point $\bar{I}_D = B$ is a delicate matter, because we cannot know a priori if the system is going to make a transition to a + or a − mode, which depends on the rotation state in the body fixed frame. In particular, the sign of the mode is given by the angles θ and ψ, so we should go back to the full perturbed solution to know what these angles are doing near the transition.

When the full solution is close to the transition point we find it has a *chaotic behavior*: the system can transit from a $SAM_\pm$ to a $LAM_\pm$ several times before reaching a stable condition, at which point it makes sense to continue the averaged study. We will explain this with the following example.

Example. To better understand why this happens and in what sense the transition has a chaotic behavior, we recall that the direct formula (3.2) for I_D depends on the angles θ and ψ, the unperturbed behavior of these angles is:

- SAM_+: $\theta \in]0, \frac{\pi}{2}[$ oscill., $\psi \in [0, 2\pi]$ circul.
- SAM_-: $\theta \in]\frac{\pi}{2}, \pi[$ oscill., $\psi \in [0, 2\pi]$ circul.
- LAM_+: $\theta \in]0, \pi[$ libr. around $\frac{\pi}{2}$, $\psi \in]0, \pi[$ libr. around $\frac{\pi}{2}$
- LAM_-: $\theta \in]0, \pi[$ libr. around $\frac{\pi}{2}$, $\psi \in]\pi, 2\pi[$ libr. around $\frac{\pi}{2}$

and the period of ψ is exactly twice the period of θ.

We can examine as an example a transition $SAM_+ \to LAM$. Let us suppose the body is in a SAM_+ state and we are approaching a transition, i.e. $I_D \sim B$. This means that the angle θ is approaching the value $\pi/2$, while the angle ψ is still circulating in $[0, 2\pi]$. Because ψ is circulating with twice the period of θ, immediately after I_D transitions to $< B$, the angle ψ has "the same probability" to be in the interval $]0, \pi[$ or $]\pi, 2\pi[$. In the first case the body is captured in a LAM_+ state, in the second case in a LAM_- state. A qualitative example of the level curves of the function $I_D = I_D(\theta, \psi)$ on the rectangle (θ, ψ) and examples of unperturbed orbits and possible perturbed transitions are given in the next Figure 3.11.

After the transition, the solution can either stay close to the value $I_D \sim B$, and we can have a transition again, or instead, depending on the sign of $\dot{\bar{I}}_D$ (see subsection 5.2), it can go far enough from the transition zone to be captured in a definite mode for a longer time span.

Def. We say the the system is in a *steady state condition* if $\bar{I}_D$ remains far from the critical point $\bar{I}_D = B$ for a long time span, where long is measured with respect to the orbital period T_{orb}.

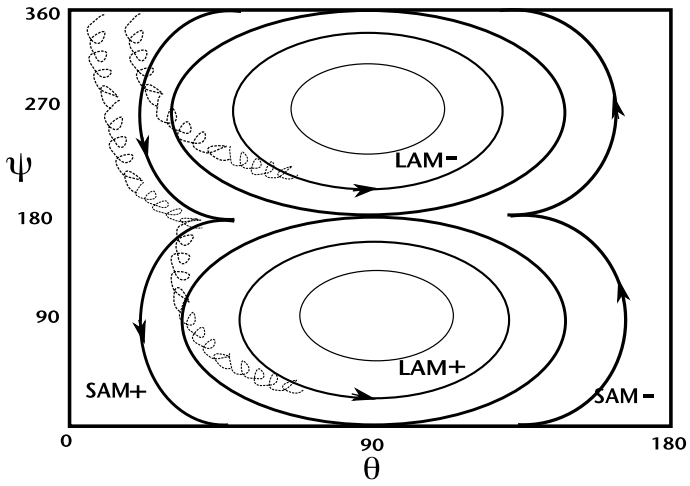

Figure 3.11: Qualitative cartoon of the level curves of the function $I_D = I_D(\theta, \psi)$ on the rectangle (θ, ψ) (solid lines), the different modes SAM and LAM are highlighted. The dashed curves are examples of perturbed orbits which can transition from the SAM_+ mode to the LAM_- or to the LAM_+ mode.

3.5.1 The transition probability

In order to predict what kind of transition the system is going to have, using only the averaged equations, we define a transition probability:

Def1. Assume that $\bar{I}_D$ is monotonically approaching the critical value $\bar{I}_D = B$. We define the *transition probability* $P_t^{\pm}$ to the other mode (SAM or LAM) + or −, as the percentage of the initial conditions θ_0, ϕ_0, ψ_0 such that the body makes a transition to the mode + or the mode −.

According to the previous discussion, we assume, as a rule, that the transition probability to the other mode + or − is $P_t^+ = P_t^- = 0.5$.

Def2. Once a transition occurs, we define in the same way the *probability to have another transition*, P_{nt}, before reaching a steady state condition.

In general we can have two kinds of situations near the critical value $\bar{I}_D = B$:

- The *potential transition* modes:

$$SAM \quad \text{with} \quad \dot{\bar{I}}_D < 0 \qquad \text{or} \qquad LAM \quad \text{with} \quad \dot{\bar{I}}_D > 0$$

- The *potential steady state* modes:

$$SAM \quad \text{with} \quad \dot{\bar{I}}_D > 0 \qquad \text{or} \qquad LAM \quad \text{with} \quad \dot{\bar{I}}_D < 0$$

We assume that the probability to have another transition whenever we are in a "potential transition" mode is $P^a_{nt} = 1$. We note that, for a non-averaged dynamical system, that this probability could be less than 1.

We assume that the probability to have another transition when we are in a potential steady state mode is $P^s_{nt} = 0.5$, but this is not an intuitive rule as the ones above, and it is only a first guess. While intuitively one would think this probability should be "0", our numerical results show that the short period fluctuations about the secular motion allow for a non-zero probability here.

As a consequence, assuming that following a transition we enter to a potential transition mode with probability P^a_t and enter a potential steady state mode with probability P^s_t, the total probability to have another transition is

$$P_{nt} = P^a_t P^a_{nt} + P^s_t P^s_{nt}.$$

For example, assuming that one mode (e.g. the $+$) is a transition approaching and the other (the $-$) is a potentially steady state, with our previous assumptions we have $P_{nt} = 0.75$.

3.5.2 Chaotic phase and steady state evolution

As anticipated before, when we are approaching a transition we can have only the two following behaviors:

- The system stays for a while in a chaotic state, undergoing several transitions: the average behavior is basically $\bar{I}_D \cong B$, $\dot{\bar{\delta}} \cong 0$ and $\dot{\bar{L}} \cong 0$.
- The system falls into a steady state mode and it goes far from the transition point $\bar{I}_D = B$.

Once we know what is the probability for the system to have a new transition before reaching a steady state condition, we can compute the probability to reach a steady state condition after N transitions. This provides us with an idea of the time span in which the system persist in chaotic behavior.

For example, with our previous hypothesis, the probability to have at least $N = 10$ subsequent transitions is $P = (P_{nt})^N \cong 0.05$, which is low. Then the probability to reach a steady state condition after more than $N = 10$ subsequent transitions is $P^s \cong 0.95$.

If we assume that there is, on average, one or two transitions per year, this means that the chaotic behavior will last from 5 to 10 years.

Finally, if we come back to the situation in which the system is approaching the transition for the first time, we have two possible steady state conditions that can happen after a chaotic phase, the probability to get to each one of them is 0.5.

3.5.3 Tests on the chaotic transition

In order to verify numerically the previous discussion about the chaotic transition of a body under torque, we used the asteroid *Toutatis* shape model to perform some tests.

In this case the transition modes are SAM_+ and LAM_+, while the steady state modes are SAM_- and LAM_- (see section 6.1). Using suitable initial conditions, we obtain an averaged solution which is approaching the critical value $\bar{I}_D = B$. In these tests we are approaching the transition from the SAM_+ mode.

To see what happens during the transition, we start a full numerical integration close to the critical value, choosing the initial conditions for the angles θ, ϕ and ψ in a suitable way to have the right initial value for I_D. This choice is not unique, and we find that choosing slightly different values for these initial conditions yields very different evolutions.

In the first example the body ultimately transitions from SAM_+ to LAM_-, and during the chaotic phase it undergoes the following transitions before reaching a steady state condition:

$$SAM_+ \to LAM_+ \to SAM_- \to LAM_- \to SAM_+ \to$$

$$\to LAM_- \to SAM_- \to LAM_- \to SAM_+ \to LAM_-.$$

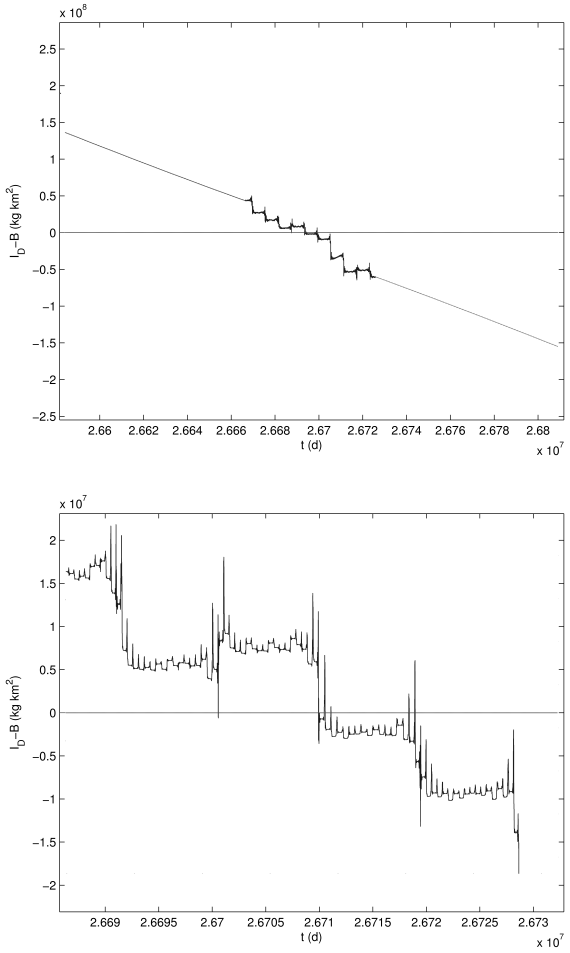

Figure 3.12: Time versus the dynamic inertia I_D. On the top, the full numerical simulation going through the transition point $I_D = B$ (horizontal line), connected with two branches of the secular solution. On the bottom a detail of the transitions. In this case the system goes from the SAM_+ mode to the LAM_- mode.

In the second example, we change the initial conditions a small amount with respect to the first example, and the body has instead a transition from SAM_+ to SAM_-, and during the chaotic phase it undergoes the following transitions before reaching a steady state condition:

$$SAM_+ \rightarrow LAM_+ \rightarrow SAM_-.$$

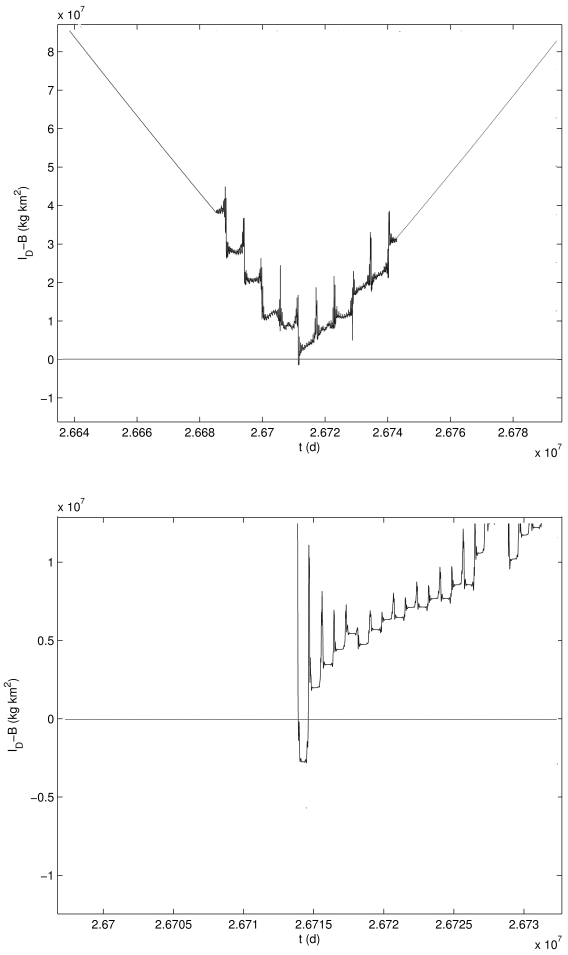

Figure 3.13: Time versus the dynamic inertia I_D. On the top, the full numerical simulation going through the transition point $I_D = B$ (horizontal line), connected with two branches of the secular solution. On the bottom a detail of the transitions. In this case the system goes from the SAM_+ mode to the SAM_- mode.

3.5.4 Other possible transitions

Another effect similar to the transition phenomenon described in this section, is the behavior of the solution close to the stationary points $\dot{\bar{I}}_D = 0$ and $\dot{\bar{\delta}} = 0$. Since they are stationary points for the averaged dynamical system (3.20), the secular solution cannot cross them in the plane $(\bar{I}_D, \bar{\delta})$. However, if the secular solution is close enough to these lines, then, because the true solution has non zero finite amplitude around the secular one, it can eventually cross the stationary point, and there is a non zero probability for the solution to fall into the other side with respect to the lines $\dot{\bar{I}}_D = 0$ or $\dot{\bar{\delta}} = 0$. According to this mechanism, it is possible for the true solution to go through the whole plane $(\bar{I}_D, \bar{\delta})$ regardless of the presence of stationary points for the averaged solution. Indeed, the true solution can remain close to the stationary value for a long time span, following, on average, orbits on both sides of that value. But since the secular orbits have to go through the level curves of the first integral (3.21), at some point the solution has to go far away from the stationary value. On which side of the stationary value the true solution goes at the end is a matter of probability. An idea of this behavior is given in the next Figure 3.14, obtained using the asteroid *Toutatis* shape model (see section 6).

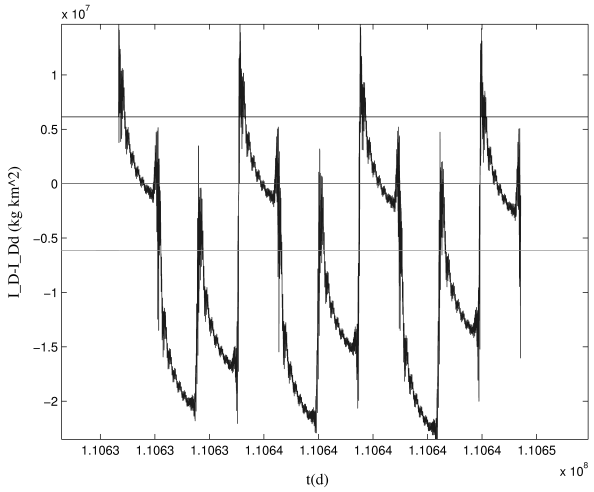

Figure 3.14: On the vertical axis the dynamic inertia I_D, translated by the stationary value $\bar{I}_D^d$. On the horizontal axis the time ($\Delta t \cong 10 T_{orb}$). The solid and the dashed horizontal lines are the secular solutions close to the stationary value (zero horizontal line). The true solution oscillates going through both sides with respect to the stationary point.

3.6 Tests on asteroids

In the sections 3.6, 3.7, 5.3 and 5.4 we showed the results from numerical integrations in which we used the asteroid *Toutatis* shape model. The model we used consists in $N \cong 3000$ triangular facets. In this section we test seven different asteroid shape models, all of them consisting in thousands of triangular facets. The asteroids we test are *Toutatis*, *1998 KY26*, *Castalia*, *Golevka* (shape models from [Neese 2004]), the asteroid *1992 SK*, from [Busch et al 2006], the asteroid *Nereus*, from [Brozovic et al. 2009] and the asteroid *1999 KW4*, from [Ostro et al 2006] (Figs. 3.15, 3.16).

3.6.1 Computation of the $\mathcal{D}_k$ functions

We compute here the $\mathcal{D}_k$ functions for all of them, using a discretization of the interval (A, C) with ~ 100000 points. The functions are normalized using the mean radius cube R_m^3 of each asteroid, and they are plotted together in the next Figures 3.17 - 3.20, assuming the positive sign for the modes SAM and LAM. We recall that $\mathcal{D}_k^- = -\mathcal{D}_k^+$. Finally, we summarize the main features of these functions in Tables 3.1 and 3.2, in light of the discussion of section 4.

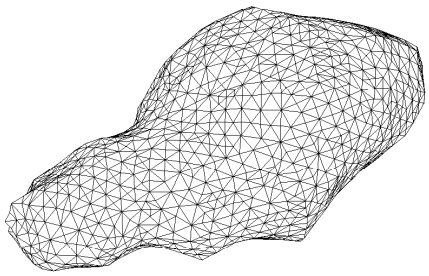

Figure 3.15: The asteroid *Toutatis* shape model with $N \cong 3000$ facets.

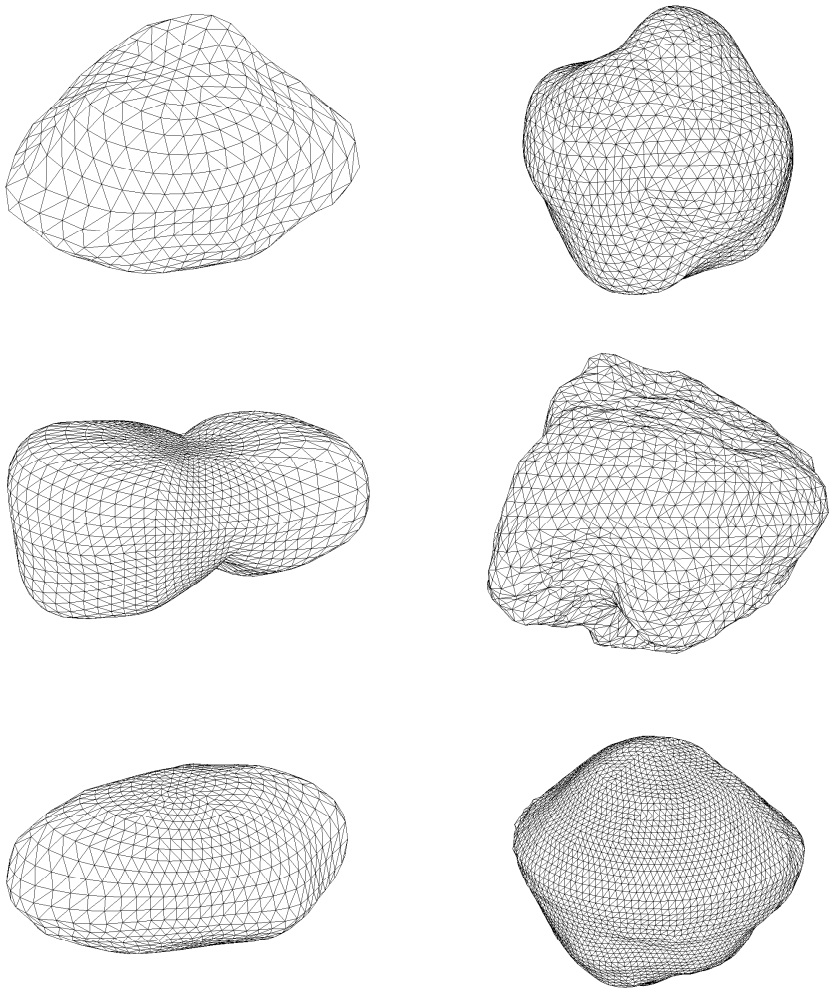

Figure 3.16: From the top on the left to the bottom on the right, the asteroids *1992 SK*, *1998 KY26*, *Castalia*, *Golevka*, *Nereus* and *1999 KW4* shape models. All of them consist of thousands of triangular facets.

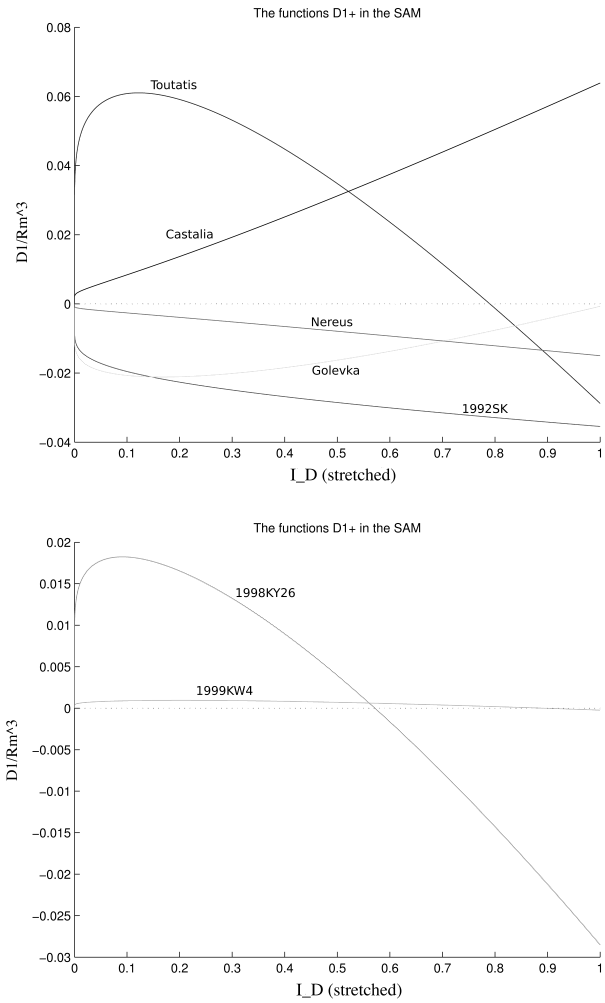

Figure 3.17: In this plot we show the $\mathcal{D}_1$ functions for the seven asteroid shape models we tested, normalized by the mean radius cube R_m^3 of the asteroid, for the SAM_+ case. The horizontal axis is stretched for each asteroid in order to show the plots together $((B, C) \to (0, 1))$. The zero value is highlighted with an horizontal line.

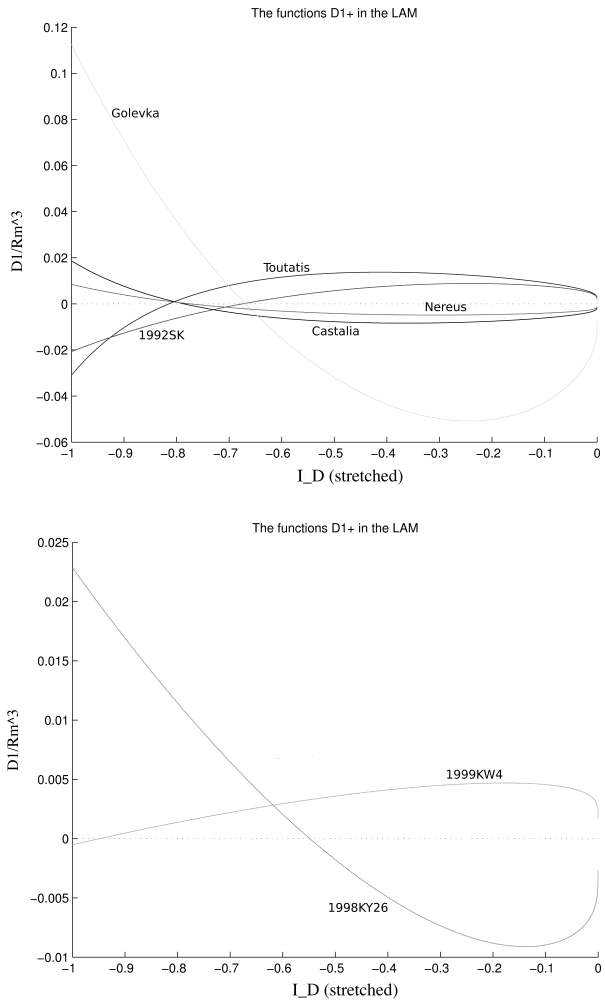

Figure 3.18: In this plot we show the $\mathcal{D}_1$ functions for the seven asteroid shape models we tested, normalized by the mean radius cube R_m^3 of the asteroid, for the LAM_+ case. The horizontal axis is stretched for each asteroid in order to show the plots together $((A, B) \to (-1, 0))$. The zero value is highlighted with an horizontal line.

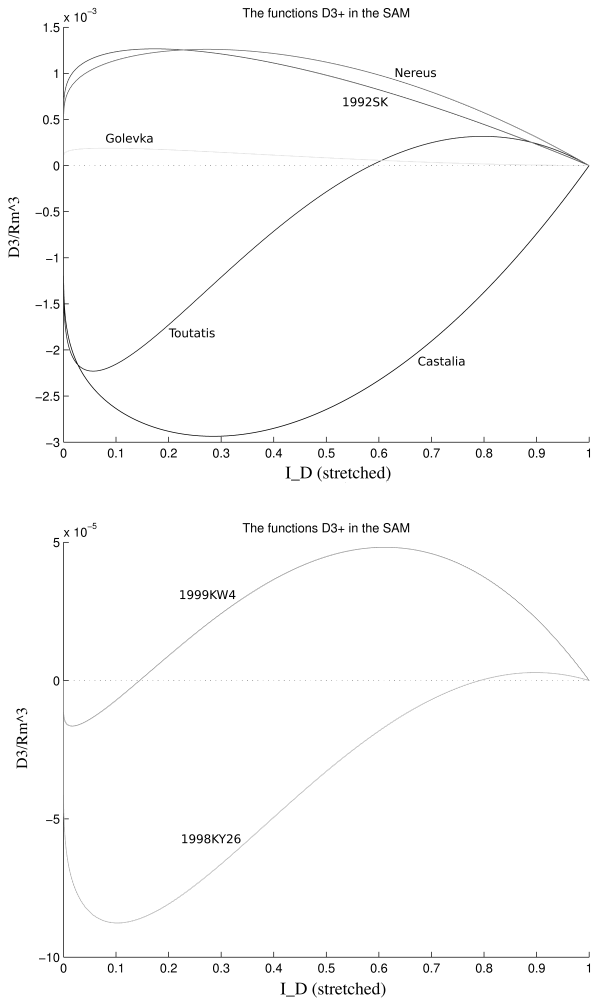

Figure 3.19: In this plot we show the $\mathcal{D}_3$ functions for the seven asteroid shape models we tested, normalized by the mean radius cube R_m^3 of the asteroid, for the SAM_+ case. The horizontal axis is stretched for each asteroid in order to show the plots together ($(B, C) \to (0, 1)$). The zero value is highlighted with an horizontal line.

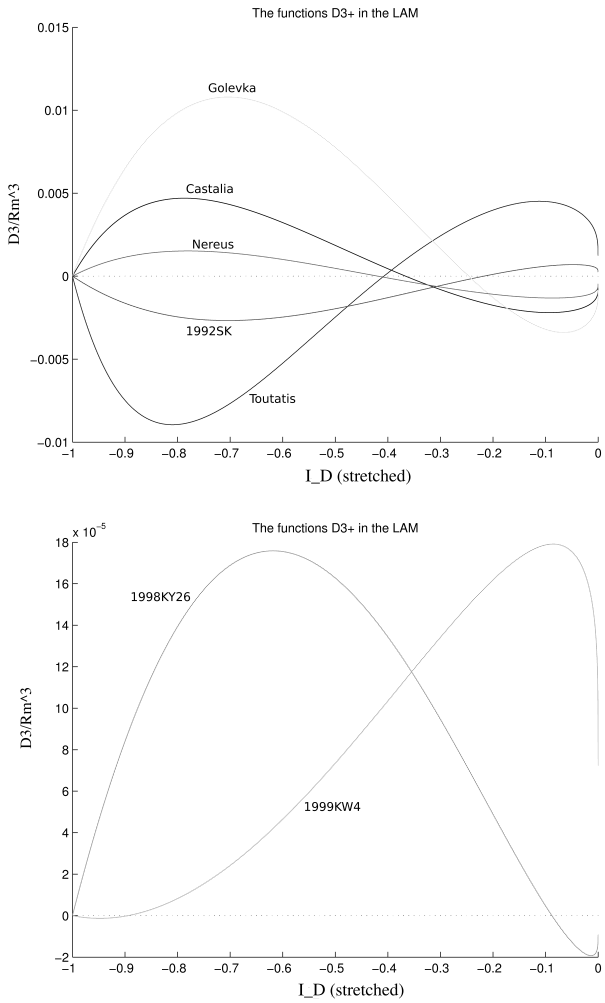

Figure 3.20: In this plot we show the $\mathcal{D}_3$ functions for the seven asteroid shape models we tested, normalized by the mean radius cube R_m^3 of the asteroid, for the LAM_+ case. The horizontal axis is stretched for each asteroid in order to show the plots together $((A, B) \to (-1, 0))$. The zero value is highlighted with an horizontal line.

	LAM		
Asteroid	# roots of $\mathcal{D}_1$	# roots of $\mathcal{D}_3$	Eq. point $(\bar{I}_D^e, \bar{\delta}^*)$
Toutatis	1	1	center
1992 SK	1	1	center
1998 KY26	1	1	center
Castalia	1	1	center
Golevka	1	1	center
Nereus	1	1	center
1999 KW4	1	1	center

Table 3.1: The main features of the $\mathcal{D}_k$ functions for the asteroid shape models that we tested, for $\bar{I}_D \in (A, B)$. The behavior of the solutions are the ones described in Figure 3.8.

	SAM		
Asteroid	# roots of $\mathcal{D}_1$	# roots of $\mathcal{D}_3$	Eq. point $(\bar{I}_D^e, \bar{\delta}^*)$
Toutatis	1	1	center
1992 SK	0	0	-
1998 KY26	1	1	center
Castalia	0	0	-
Golevka	0	0	-
Nereus	0	0	-
1999 KW4	1	1	center

Table 3.2: The main features of the $\mathcal{D}_k$ functions for the asteroid shape models that we tested, for $\bar{I}_D \in (B, C)$. The behavior of the solutions are the ones described in Figures 3.8 and 3.9.

We note that in all of the shape models we tested, we only found the behaviors of Figures 3.8 and 3.9, and we did not find any of the "hyperbolic" points described in section 4. We also note that there is no strong preference for the sign of $\mathcal{D}_k^+$ over the different intervals. We note explicitly that the asteroids *1992 SK*, *Castalia*, *Golevka* and *Nereus* have a phase plane of the sort found in Figure 3.8 for the LAM state and of the sort found in Figure 3.9 for the SAM state.

3.6.2 Tests of the dynamics in detail: Asteroid Toutatis

In this subsection we perform some numerical simulation using the *Toutatis* shape model and the rotation state initial conditions given in
[Hudson & Ostro 1995]. As stated in Hudson and Ostro the asteroid Toutatis had the following initial conditions at the epoch 11 *Dec* 1992:

$$\theta_0 \cong 65^\circ, \quad \phi_0 \cong 40^\circ, \quad \psi_0 \cong 134^\circ, \quad \rho_0 \cong 142^\circ, \quad \sigma_0 \cong 136^\circ,$$

which means a LAM_+ mode with $I_{D0}/B \cong 0.54$ and an obliquity of $\delta_0 \cong 65^\circ$. The asteroid's mass is $m \cong 1.5 \times 10^{13}$ kg, the moments of inertia over mass ratios are $A/m \cong 0.37$ km^2, $B/m \cong 1.11$ km^2, $C/m \cong 1.18$ km^2.

The numerical integration of the averaged equations, for a time span of $\Delta t \cong 10^6\, T_{orb}$, $T_{orb} \cong 4$ years, is described in the next Figures 3.21 and 3.22. Note that the solution has to stay in a level curve of the first integral (3.21), the orbit is closed and it undergoes one full cycle in the plane $(\bar{I}_D, \bar{\delta})$.

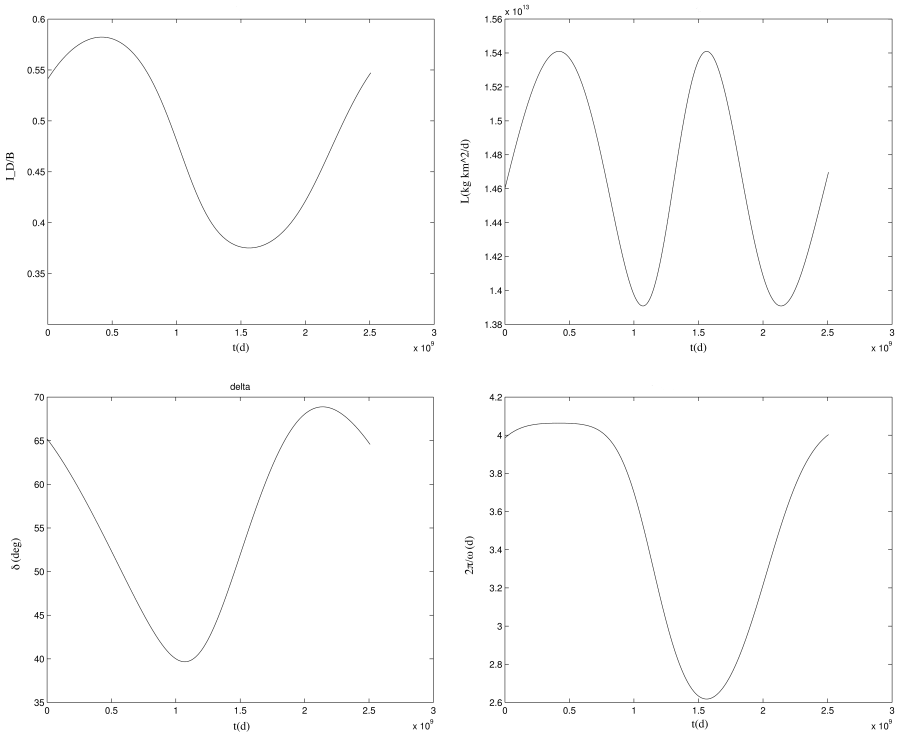

Figure 3.21: From the top on the left to the bottom on the right: the dynamic inertia $\bar{I}_D/B$, the angular momentum magnitude $\bar{L}$, the averaged obliquity $\bar{\delta}$ and the effective rotational period $2\pi/\bar{\omega}_l$ over time, $\bar{\omega}_l = \bar{L}/\bar{I}_D$.

As we noticed in section 4.5, if we also add the effect of a small energy dissipation through the formulas (3.23) and (3.24), the solution does not remain on the level curve of the first integral of formula (3.21), and it tends to the equilibrium point (asymptotic value) in the case that stability is introduced, and otherwise it goes away from it, , which is the case that occurs in Figure 3.22.

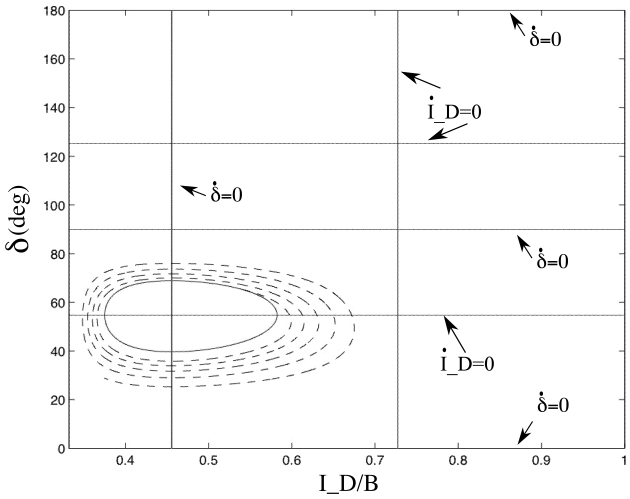

Figure 3.22: The secular solution (solid line) stays in a closed cycle around the equilibrium point ($\bar{I}_D^e, \sim 55^\circ$) on the plane ($\bar{I}_D, \bar{\delta}$), where $\mathcal{D}_1(\bar{I}_D^e) = 0$, $\bar{I}_D^e \in (A, B)$ (LAM_+). The dashed curve is the solution with a small energy dissipation, enhanced enough to be clearly seen ($\varrho \cong 2\, g/cm^3$, $\mu Q \cong 10^{10}\, g/cm\, s^2$) and integrated over a long enough time span ($\Delta t \cong 10^7 T_{orb}$). Its effect is to drive the solution far from the equilibrium point on a spiral. $\bar{I}_D$ is scaled by the value B, the stationary values for $\bar{I}_D$ (vertical lines) and $\bar{\delta}$ (horizontal lines) are highlighted.

3.7 Conclusions

In this paper we developed the first analytical approach to the problem of a rigid body in non-principal axis rotation under the YORP torque.

The method we used is based on a first order approximation of the general rotational equations of motion with a small torque, averaged over the fast rotational angles in order to capture the secular terms. To make the analytical computation easier, we assumed zero thermal inertia and a second order approximation for the illumination function, considering only "convex-like" bodies, hence no possible self-shadowing. Energy dissipation equations are also derived for eventual incorporation into the model.

We obtained simple integrable secular equations for the angular momentum, the dynamic inertia and the obliquity. We tested them on several real asteroid shape models, in particular on the asteroid Toutatis, which is known to be in a non-principal axis state.

These equations show the same basic properties of previous research on principal axis rotators under YORP, like [Scheeres & Mirrahimi 2008] and
[Nesvorny & Vokrouhlicky 2007], and have main features in agreement with the numerical simulations of [Vokrouhlicky et al. 2007], although also some non negligible differences as the closed cycles around the equilibrium points which correspond instead to asymptotic states in their numerical simulations.

We believe that the main limit of the current approach is in the model of the illumination function, besides the zero termal lag approximation. As pointed out in [Statler 2009], small changes in the surface of the body, and so in the illumination model, yield significant effects on the rotation.

A better analytical model for the illumination of the body, including self-shadowing and finite thermal inertia, is necessary to describe the rotational dynamics under the YORP torque in a more accurate way. Whether a more detailed analytical approach can be afforded or not, is a challenge for future improvements of this work.

Appendix C

The averaged factors

Once we have chosen the initial conditions of the dynamical system, we have a nominal initial value for $I_D = I_{D0}$, which is constant in the unperturbed solution. We distinguish between SAM mode, if $B < I_{D0} < C$, or LAM mode, if $A < I_{D0} < B$.

The complete classification of the unperturbed motion is given by the following rule:

$$SAM_+ \Leftrightarrow \{B < I_D < C \ \wedge \ \cos\theta > 0\},\ SAM_- \Leftrightarrow \{B < I_D < C \ \wedge \ \cos\theta < 0\},$$

$$LAM_+ \Leftrightarrow \{A < I_D < B \ \wedge \ \sin\psi > 0\},\ LAM_- \Leftrightarrow \{A < I_D < B \ \wedge \ \cos\psi < 0\}.$$

In the following, let be

$$k^2 = \frac{(B-A)(C-I_D)}{(I_D-A)(C-B)} \quad SAM, \qquad k^2 = \frac{(I_D-A)(C-B)}{(B-A)(C-I_D)} \quad LAM$$

and K and E are, respectively, the complete elliptic integrals of the first and of the second kind, with parameter k. We indicate with $\pm$ the rotation mode $SAM_\pm$ or $LAM_\pm$.

The time dependence of the quantities a_{**} through the unperturbed angles θ, ψ has always a period $P_{\theta\psi} = 4K$. All the following formulas follow from the properties of the elliptic functions sn, cn, dn with parameter k.

$$\begin{aligned} < a_{z\,\xi} >_e &= \frac{1}{4K}\sqrt{\frac{A(C-I_D)}{I_D(C-A)}}\int_0^{4K} cn(\tau)\,d\tau = 0 \quad SAM \\ &= \pm\frac{1}{4K}\sqrt{\frac{A(C-I_D)}{I_D(C-A)}}\int_0^{4K} dn(\tau)\,d\tau = \pm\frac{\pi}{2K}\sqrt{\frac{A(C-I_D)}{I_D(C-A)}} \quad LAM \end{aligned}$$

$$\begin{aligned} < a_{z\,\eta} >_e &= \frac{1}{4K}\sqrt{\frac{B(C-I_D)}{I_D(C-B)}}\int_0^{4K} sn(\tau)\,d\tau = 0 \quad SAM \\ &= \frac{1}{4K}k\sqrt{\frac{B(C-I_D)}{I_D(C-B)}}\int_0^{4K} sn(\tau)\,d\tau = 0 \quad LAM \end{aligned}$$

$$
\begin{aligned}
< a_{z\,\zeta} >_e &= \pm\frac{1}{4K}\sqrt{\frac{C(I_D-A)}{I_D(C-A)}}\int_0^{4K} dn(\tau)\,d\tau = \pm\frac{\pi}{2K}\sqrt{\frac{C(I_D-A)}{I_D(C-A)}} \quad SAM \\
&= \frac{1}{4K}\sqrt{\frac{C(I_D-A)}{I_D(C-A)}}\int_0^{4K} cn(\tau)\,d\tau = 0 \quad LAM.
\end{aligned}
$$

The $z-$ components products:

$$
< a_{z\,\xi} a_{z\,\eta} >_e = < a_{z\,\xi} a_{z\,\zeta} >_e = < a_{z\,\eta} a_{z\,\zeta} >_e = 0
$$

$$
\begin{aligned}
< a_{z\,\xi}^2 >_e &= \frac{A(C-I_D)}{I_D(C-A)}(1-\frac{1}{k^2}(1-\frac{E}{K})) \quad SAM \\
&= \frac{A(C-I_D)}{I_D(C-A)}\frac{E}{K} \quad LAM
\end{aligned}
$$

$$
\begin{aligned}
< a_{z\,\eta}^2 >_e &= \frac{B(I_D-A)}{I_D(B-A)}(1-\frac{E}{K}) \quad SAM \\
&= \frac{B(C-I_D)}{I_D(C-B)}(1-\frac{E}{K}) \quad LAM
\end{aligned}
$$

$$
\begin{aligned}
< a_{z\,\zeta}^2 >_e &= \frac{C(I_D-A)}{I_D(C-A)}\frac{E}{K} \quad SAM \\
&= \frac{C(I_D-A)}{I_D(C-A)}(1-\frac{1}{k^2}(1-\frac{E}{K})) \quad LAM.
\end{aligned}
$$

The $z-$components triple products with non zero average in the SAM case are:

$$
< a_{z\,\zeta}^3 >_e = \pm\left(\frac{C(I_D-A)}{I_D(C-A)}\right)^{3/2}\frac{\pi}{4K}(2-k^2),
$$

$$
< a_{z\,\xi}^2 a_{z\,\zeta} >_e = \pm\frac{A(C-I_D)}{I_D(C-A)}\sqrt{\frac{C(I_D-A)}{I_D(C-A)}}\frac{\pi}{4K},
$$

$$
< a_{z\,\eta}^2 a_{z\,\zeta} >_e = \pm\frac{B(C-I_D)}{I_D(C-B)}\sqrt{\frac{C(I_D-A)}{I_D(C-A)}}\frac{\pi}{4K}.
$$

The $z-$components triple products with non zero average in the LAM case are:

$$
< a_{z\,\xi}^3 >_e = \pm\left(\frac{A(C-I_D)}{I_D(C-A)}\right)^{3/2}\frac{\pi}{4K}(2-k^2),
$$

$$< a_{z\,\xi} a_{z\,\zeta}^2 >_e = \pm \frac{C(I_D - A)}{I_D(C - A)} \sqrt{\frac{A(C - I_D)}{I_D(C - A)}} \frac{\pi}{4K},$$

$$< a_{z\,\xi} a_{z\,\eta}^2 >_e = \pm \frac{B(C - I_D)}{I_D(C - B)} \sqrt{\frac{A(C - I_D)}{I_D(C - A)}} k^2 \frac{\pi}{4K}.$$

The other averaged factors that we used in the dissipation torque are the following, in the $SAM_{\pm}$ case:

$$< a_{z\,\zeta}^5 >_e = \pm \left(\frac{C(I_D - A)}{I_D(C - A)} \right)^{5/2} \frac{\pi}{4K} \left(2 - 2k^2 + \frac{3}{4} k^4 \right),$$

$$< a_{z\,\xi}^2 a_{z\,\zeta}^3 >_e = \pm \frac{A(C - I_D)}{I_D(C - A)} \left(\frac{C(I_D - A)}{I_D(C - A)} \right)^{3/2} \frac{\pi}{4K} \left(1 - \frac{k^2}{4} \right),$$

$$< a_{z\,\eta}^2 a_{z\,\zeta}^3 >_e = \pm \frac{B(C - I_D)}{I_D(C - B)} \left(\frac{C(I_D - A)}{I_D(C - A)} \right)^{3/2} \frac{\pi}{4K} \left(1 - \frac{3k^2}{4} \right),$$

and in the $LAM_{\pm}$ case:

$$< a_{z\,\xi}^5 >_e = \pm \left(\frac{A(C - I_D)}{I_D(C - A)} \right)^{5/2} \frac{\pi}{4K} \left(2 - 2k^2 + \frac{3}{4} k^4 \right),$$

$$< a_{z\,\xi}^3 a_{z\,\zeta}^2 >_e = \pm \frac{C(I_D - A)}{I_D(C - A)} \left(\frac{A(C - I_D)}{I_D(C - A)} \right)^{3/2} \frac{\pi}{4K} \left(1 - \frac{k^2}{4} \right),$$

$$< a_{z\,\xi}^3 a_{z\,\eta}^2 >_e = \pm \frac{B(C - I_D)}{I_D(C - B)} \left(\frac{A(C - I_D)}{I_D(C - A)} \right)^{3/2} k^2 \frac{\pi}{4K} \left(1 - \frac{3k^2}{4} \right).$$

Acknowledgements

The funding for this work was provided by the University of Pisa, "Scuola di Dottorato Galileo Galilei", Department of Mathematics. D.J. Scheeres acknowledges support from a NASA Planetary Geology and Geophysics grant. The authors want to thank D. Vokrouhlicky for his insightful suggestions and S. Breiter who, as a referee, helped to improve a lot the preliminar version of this work.

Bibliography

[Arnold et al. 1998] Arnold, V.I., Kozlov V.V., Neishtadt, A.I.: *Mathematical aspects of classical and celestial mechanics* Encyclopaedia of Mathematical Science, 3. Springer, Berlin, (1998)

[Brozovic et al. 2009] M. Brozovic, et al. *Radar observations and a physical model of Asteroid 4660 Nereus, a prime space mission target.* Icarus **201** 153-166 (2009).

[Busch et al 2006] Busch, M.W., et al.: *Radar and optical observations and physical modeling of near-Earth Asteroid 10115 (1992 SK).* Icarus **181**, 145-155 (2006).

[Capek & Vokrouhlicky 2004] Capek, D., Vokrouhlicky, D.: *The YORP effect with finite thermal conductivity.* Icarus **172**, 526-536, (2004).

[Hudson & Ostro 1995] Hudson, R.S., Ostro, S.J.: *Shape and Non-Principal axis spin state of asteroid 4179 Toutatis.* Science **270**, 84-86, (1995).

[Mysen 2007] Mysen, E.: *The dynamics of globally active triaxial comets, with applications to asteroid rotation.* Mon.Not.R.Astron.Soc. **381**, 301-307, (2007)

[Mysen 2008] Mysen, E.: *An analytical model for YORP and Yarkovsky effects with a physical thermal lag.* A&A **484**, 563-573 (2008)

[Neese 2004] Neese, C., Ed. Small Body Radar Shape Models V2.0. EAR-A-5-DDR-RADARSHAPE-MODELS-V2.0. NASA Planetary Data System, (2004).

[Neishtadt et al. 2003] Neishtadt, A.I., Scheeres, D.J., Sidorenko, V.V., Stooke, P.J., Vasilev, A.A.: *The influence of reactive torques on comet nucleus rotation.* CMDA **86**, 249-275, (2003)

[Nesvorny & Vokrouhlicky 2007] Nesvorny, D., Vokrouhlicky, D.: *Analytical theory of the YORP effect for near spherical objects.* Astronom J **134**, 1750-1768, (2007)

[Ostro et al 2006] Ostro, S.J., et al. *Radar Imaging of Binary Near-Earth Asteroid (66391) 1999 KW4.* Science 314: 1276, (2006).

[MacMillan 1936] MacMillan, W.D.: *Dynamics of Rigid Bodies.* McGraw-Hill, (1936).

[Rubincam 2000] Rubincam, D.P.: *Radiative spin-up and spin-down of small asteroids.* Icarus **148**, 2-11, (2000).

[Scheeres 2007] Scheeres, D.J.: *The dynamical evolution of uniformly rotating asteroids subject to YORP.* Icarus **188**, 430-450, (2007).

[Scheeres & Mirrahimi 2008] Scheeres, D.J., Mirrahimi, S.: *Rotational dynamics of a solar system body under solar radiation torque.* CMDA **101**, 69-103, (2008)

[Sharma et al. 2005] Sharma, I., Burns, J.A., Hui, C.Y.: *Nutational damping times in solids of revolution.* Mon.Not.R.Astron.Soc. **359**, 79-92, (2005)

[Sidorenko et al. 2008] Sidorenko V.V., Scheeres D.J., Byram S.M.: *On the rotation of comet Borrelly's nucleus.* CMDA **102**, 133-147, (2008).

[Statler 2009] Statler, T.S.: *Extreme Sensitivity of the YORP Effect to Small-Scale Topography.* Icarus **202**, Issue 2, 502-513, (2009).

[Vokrouhlicky et al. 2007] Vokrouhlicky, D., Breiter, S., Nesvorny, D., Bottke, W.F.: *Generalized YORP evolution: onset of tumbling and new asymptotic states.* Icarus **191**, 636-650, (2007)

[Vokrouhlicky & Capek 2002] Vokrouhlicky, D., Capek, D.: *YORP-induced long term evolution of the spin state of small asteroids and meteoroids: Rubincam's approximation.* Icarus **159**, 449-467, (2002)